Benedict Jux

Multi-Physics Design of High-Speed Permanent Magnet Synchronous Machines for Hydrogen Fuel Cell Air Compressors

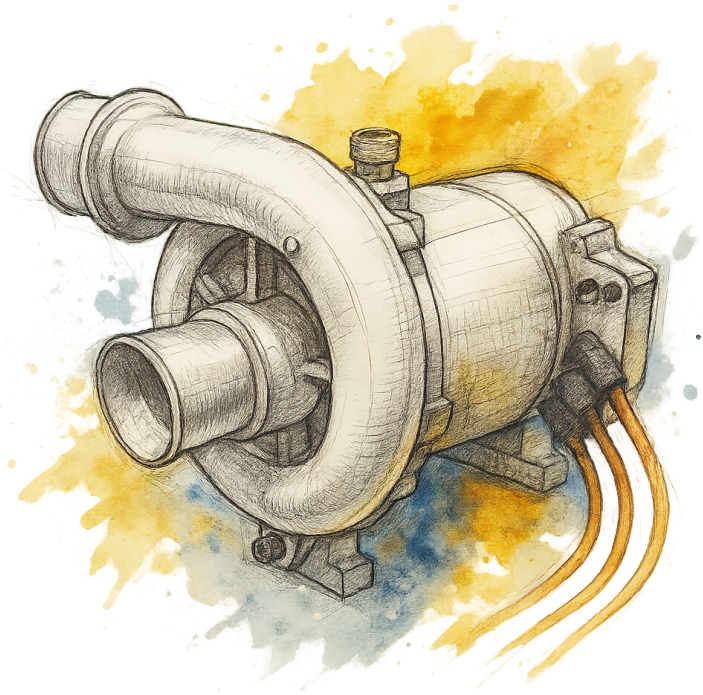

Karlsruhe Institute of Technology

Elektrotechnisches Institut

Multi-Physics Design of High-Speed Permanent Magnet Synchronous Machines for Hydrogen Fuel Cell Air Compressors

Zur Erlangung des akademischen Grades eines

DOKTORS DER INGENIEURWISSENSCHAFTEN
(Dr.-Ing.)

von der KIT-Fakultät für
Elektrotechnik und Informationstechnik
des Karlsruher Instituts für Technologie (KIT)
angenommene

Dissertation

von
M.Sc. Benedict Jux
geb. in: Bergisch Gladbach

Tag der mündlichen Prüfung:	27.06.2025
Hauptreferent:	Prof. Dr.-Ing. Martin Doppelbauer
Korreferent:	Prof. Dr.-Ing. Markus Henke (TU Braunschweig)

Karlsruher Institut für Technologie (KIT)
Elektrotechnisches Institut (ETI)

Zur Erlangung des akademischen Grades eines Doktor-Ingenieurs
von der KIT-Fakultät für Elektrotechnik und Informationstechnik des
Karlsruher Instituts für Technologie (KIT) eingereichte Dissertation
von M.Sc. Benedict Jux, geb. Bergisch Gladbach.

Tag der mündlichen Prüfung:	27.06.2025
Hauptreferent:	Prof. Dr.-Ing. Martin Doppelbauer
Korreferent:	Prof. Dr.-Ing. Markus Henke (TU Braunschweig)

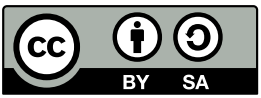

Kurzfassung

In Protonenaustauschmembran-Brennstoffzellen kann Wasserstoff in Verbindung mit Sauerstoff zu Wasser reagieren und elektrische Energie gewonnen werden. Um die Leistungsdichte von diesen Brennstoffzellen zu steigern, wird der Sauerstoff diesen mit erhöhtem Druck zur Verfügung gestellt. Dazu können elektrisch angetriebene Radialverdichter verwendet werden, da sie eine besonders hohe Effizienz aufweisen. Hierzu werden permanentmagneterregte Synchronmaschinen verwendet. Die Auslegung und Dimensionierung eines solchen Systems ist eine gebietsübergreifende Aufgabe und beinhaltet die Auslegung der Strömungsmaschine, die Festigkeitsberechnung des Rotorverbandes, die elektromagnetische Auslegung der elektrischen Maschine und die thermische Berechnung. Dazu wird in dieser Arbeit ein effizienter, multiphysikalischer Ansatz für die Auslegung von permanentmagneterregten Synchronmaschinen vorgestellt. Die aerodynamische Auslegung beruht auf einer Skalierung von bestehenden Systemen und umfasst sowohl die Skalierung des Radialverdichters als auch die Skalierung der Turbine, welche genutzt werden kann um Energie aus dem Abgasmassenstrom der Brennstoffzelle zu gewinnen. Weiter wird ein analytischer Ansatz vorgestellt zur Festigkeitsberechnung der Rotorbandage. In der elektromagnetischen Auslegung wird ein Ansatz entwickelt, der die Besonderheiten einer Hochdrehzahlmaschine abbildet. Der Ansatz nutzt neuronale Netze, welche mit Finite Elemente Berechnung erzeugt wurden, um die großen Luftspalte und die Krümmung der Maschinen effizient zu berücksichtigen, welche in den bekannten Ansätzen aus der Literatur nicht berücksichtigt werden. Die Auslegung wird damit vervollständigt, dass die Maschinenverluste bestimmt werden. Dazu sind analytische Ansätze beschrieben, die unter anderem die Stator Eisenverluste und die Wirbelstromverluste im Rotor berücksichtigen. In einer thermischen 2D Finite Elemente Berechnung werden die Bauteiltemperaturen der elektrischen Maschine bestimmt. Der vorgestellte Modellbildungsansatz wird

mit einer entwickelten und gebauten Maschine validiert. Es kann gezeigt werden, dass der Modellierungsansatz sehr gute Übereinstimmungen mit den Auslegungsergebnissen der Referenzmaschine zeigt. Im Anschluss wird der Modellierungsansatz für verschieden Studien genutzt. Dabei wird unter anderem der Einfluss des Bandagenmaterials untersucht, welchen Einfluss die Rotorumfangsgeschwindigkeiten auf die Auslegung haben und wie sich zusätzliche Optimierungskriterien auf die Auslegung der Maschine auswirken.

Abstract

In proton exchange membrane fuel cells, hydrogen can react with oxygen to form water and generate electrical energy. In order to increase the power density of these fuel cells, the oxygen is supplied at increased pressure. Electrically driven radial compressors can be used for this purpose, as they are particularly efficient as they are driven by permanent magnet synchronous machines. The design and dimensioning of such a system is an interdisciplinary task and includes the design of the turbomachinery, the strength calculation of the rotor assembly, the electromagnetic design of the electric machine and the thermal calculation of the machine. For this purpose, an efficient, semi-analytical, multi-physical approach for the design of permanent magnet synchronous machines is presented in this work. The aerodynamic design is based on a scaling of existing systems and includes both the scaling of the centrifugal compressor and the scaling of the turbine, which can be used to recover energy from the exhaust gas mass flow of the fuel cell. An analytical approach for calculating the stresses in the rotor sleeve is also presented. In the electromagnetic design, an approach is developed that models the properties of a high-speed electric machine. The approach uses neural networks trained with results from finite element analysis to efficiently consider the effect of the large air gaps and the curvature of the machines, which are not considered in the known approaches from literature. The magnetic domain is completed by determining the machine losses. Analytical approaches are described for this purpose, including the stator iron losses and the eddy current losses in the rotor. The component temperatures of the electrical machine are determined in a thermal 2D finite element calculation. The presented modeling approach is validated with a developed and built machine. It can be shown that the modeling approach is in very good agreement with the design results of the reference machine. The modeling approach is then used for various studies. The influence of the sleeve material, the influence of the rotor circumferential speeds

on the design and the influence of additional optimizing criteria on the machine design are investigated and presented.

Contents

Chapter 1

Introduction

In the beginning of this thesis the motivation, to investigate the design of high-speed electric compressors for hydrogen Fuel Cells (FCs), is described. Briefly the function of an electric compressor in a FC is explained. The two most popular FC technologies, Proton exchange membrane (PEM) and Solid Oxide Fuel Cell (SOFC) are briefly introduced and the application dependent need for an air compressor is explained. More in detail the effect of pressurizing the cathode side of the PEM is explained. Based on the results, the current development status of PEM in mobile applications is discussed and the advantages and disadvantages of Fuel Cell Electric Vehicles (FCEVs) are discussed. A literature review of centrifugal fuel cell compressors is presented. This leads to the objectives of the thesis. Finally, the structure of this thesis is presented and each chapter is briefly outlined.

1.1 Motivation

In the quest for a sustainable and resilient future, the need to transition away from conventional fossil fuels has become more urgent than ever. Fossil fuels, the main source of the world's current energy landscape, have powered human progress for centuries. However, their adverse environmental impact, finite availability, and contribution to climate change have prompted a global paradigm shift towards cleaner, more sustainable alternatives. As stated in the results of the COP28 [1], the world wants to step away from fossil fuels for the future to keep the global warming of $1.5\,^{\circ}\mathrm{C}$ within reach. Many countries have released their own goals and actions to reach the goal to become climate-neutral. Europe

therefore, wants to be the first climate-neutral continent by 2050 and reduce the yearly emitted greenhouse gases by 55 % by 2030 compared to 1990 [2]. The fleet of newly registered passenger cars must now reduce their emissions by 55 % by 2030, an increase from the previous target of 37.5 %. By 2035, the objective is to reach a 100 % reduction compared to 2021. For new light commercial vehicles, the fleet reduction target for 2030 is increased from 31 % to 50 %. From 2035, the EU-wide fleet targets for both vehicle classes of newly registered vehicles is 100 % zero emission drives. The EU Regulation lists the targets for the development of hydrogen charging and refuelling infrastructure. The regulation aims to extend the hydrogen refuelling and charging network along the trans-European road network for all vehicle classes. Other countries like India have released their own plans to be climate-neutral by 2070 and set up a dedicated hydrogen mission. The Indian government plans to set up regulations and infrastructure to use hydrogen among other uses in heavy commercial vehicles and long-haul operations [3]. The focus of the work is on the use of hydrogen in a fuel cell in which the hydrogen is converted into electricity. Fuel cells have a large advantage in comparison to hydrogen internal combustion engines and sustainable fuels, in terms of efficiency.
Different types of fuel cells have been developed. The two most common types are the PEM and the SOFC. A PEM is operating at low temperatures with 60 °C to 80 °C compared to the SOFC with an operating temperature of 500 °C to 1000 °C. Operating temperature limits the applications in which each type can be used. High-temperature FC will be used in applications which have a long continuous operating time. SOFCs may be employed in situations where there is a projected long-term deficit in renewable energy sources within the electricity grid. This could be achieved by utilizing green hydrogen as a fuel source. It should be noted that this technology is not well suited to address immediate power shortages due to the extended ramp-up period required for its deployment. In contrast, a PEM can be brought to the required operating temperature in a relatively short period of time. This enables the delivery of variable power. In principle, both systems can be used in conjunction with an air compression system on the cathode side. As explained below, this increases the power density of the fuel cell. This is particularly important for mobile applications. For this reason, low overpressure air compression systems are primarily used for PEM and SOFC systems in stationary applications. In mobile applications, where the power density must be high, higher pressures are required from an air compressor. Therefore, this work focuses on applications in PEM systems for mobile applications, as the power density is particularly high here and the demands on a charging system are high. [4, 5]

Hydrogen fuel cells have a wide range of applications [6–8]. They can be used in the power grid as energy generators if surplus renewable energy is stored in hydrogen with electrolyzers. Fuel cells can also be used in the transportation sector. In road transport, the fuel cell is in direct competition with the battery. Until recently the advantage of fuel cells in comparison are the high energy density of $33.3\,\mathrm{kW\,h\,kg^{-1}}$ of hydrogen and the resulting greater range with a lower overall weight [8]. As the battery technology is further evolving the advantage of the fuel cell system energy density descreases. Main weight driver in the fuel cell system is the vehicles or applications power requirement. The current system power density, including the external parts like hoses, valves and pumps, is $650\,\mathrm{W\,kg^{-1}}$ [9]. Besides that the tank has a specific weight of $17.5\,\mathrm{kg}$ per kg hydrogen stored. In addition to that new solid state battery systems have an energy density of $260\,\mathrm{W\,h\,kg^{-1}}$[10, 11]. Current vehicles like the Toyota Mirai or the BMW iX5 Hydrogen have a stack power output of $114\,\mathrm{kW}$ and $125\,\mathrm{kW}$. The battery in the Mirai and the iX5 Hydrogen have only a capacity of $1.2\,\mathrm{kW\,h}$ and $2\,\mathrm{kW\,h}$. The tank capacity is $5\,\mathrm{kg}$ and $6\,\mathrm{kg}$ respectively. Based on the mentioned specific weights the fuel cell system weight can be estimated for the two example vehicles. For the Toyota Mirai the weight is $268\,\mathrm{kg}$ and $305\,\mathrm{kg}$ for the BMW iX5 Hydrogen. The overall Worldwide Harmonized Light-Duty Vehicles Test Procedure (WLTP) reach is $504\,\mathrm{km}$ for the BMW and $650\,\mathrm{km}$ for the Toyota. That leads to an overall specific energy storage weight of $0.61\,\mathrm{kg\,km^{-1}}$ and $0.41\,\mathrm{kg\,km^{-1}}$.
On the Battery Electric Vehicle (BEV) side, the Nio ET7 has a range of $580\,\mathrm{km}$ (WLTP) with the $100\,\mathrm{kW\,h}$ battery and a battery system weight of $555\,\mathrm{kg}$, which is equal to an energy density of $180\,\mathrm{W\,h\,kg^{-1}}$. With the $150\,\mathrm{kW\,h}$ solid-state battery, the energy density increases further to $260\,\mathrm{W\,h\,kg^{-1}}$, and the WLTP range increases to $860\,\mathrm{km}$ with a battery weight of $575\,\mathrm{kg}$. This results in a specific energy storage weight of $0.67\,\mathrm{kg\,km^{-1}}$. [10, 11]
One other important point in this comparison must be noted. The aerodynamic performance of the Nio's is much better with an advertised drag coefficient of 0.21, compared to BMW's SUV and the Mirai's with a drag coefficient of 0.29. Nevertheless, it shows that the weight advantages of the fuel cell vehicle are not as significant as the energy density of the energy source indicate. With the assumption of a stack efficiency of $56\,\%$ the energy density of a hydrogen storage is about $1\,\mathrm{kg\,kW^{-1}\,h}$. With this separation the fuel cell system has its advantage in systems with a high energy demand and low output powers.
Fuel cells are not only used in road transport. Hydrogen can also be used on the railway as a replacement for diesel locomotives. There are now a number of pilot projects in this area [12]. One area that is currently attracting more and

more attention is its use for the electrification of aviation. For electric aircraft the average power demand is rather low compared to the take-off power demand. Therefore, a combination of hydrogen fuel cells and batteries might be of interest. More details on the load collective for a regional aircraft can be found in [E1]. In this area, the weight and range advantages are decisive factors in favor of using fuel cells. On the other hand, the disadvantages of the technology cannot be denied. The energy efficiency of fuel cell systems from tank to wheel is in the range of $54\,\%$ for road vehicles. In contrast, a battery-electric powertrain has an efficiency of $86\,\%$ [13]. In addition, the production of green hydrogen is less efficient compared to the charging process of a battery. The efficiency for a FCEV then reduces down to $25\,\%$ to $30\,\%$ compared to $70\,\%$ to $80\,\%$ for a BEV [14]. Furthermore, installation costs for hydrogen refueling stations are usually significantly more expensive than charging stations [12].
Details about the production of hydrogen and its origin will not be considered further here, but it should be noted that sustainable use in terms of Carbon Dioxide (CO_2) neutrality is only possible with green hydrogen. Hydrogen use in road transport increases by about $45\,\%$ in 2022 compared to 2021 to an estimated $32\,000\,000\,\mathrm{kg}$ of hydrogen. FCEVs have had the earliest success in terms of vehicle sales, in the car and bus segments, but as sales of heavy-duty fuel cell trucks increase, their share of total consumption is growing. China's focus on heavy-duty vehicles and its prominent role in the deployment of fuel cell trucks means that although only $20\,\%$ of all FCEVs are in operation in China, they consume more than half of the hydrogen used in road transport. Hydrogen use in transport is expected to remain predominantly in the road sector for the near future. Besides the road segment, several fuel cell ferries are set to begin operation in 2023, which will further diversify the use of hydrogen in transport applications. [12]
The total number of registered FCEVs in the world have reach around $80\,000$ vehicles in June 2023. This includes passenger cars, buses, and commercial vehicles. Passenger cars account for the largest share and are sold in China and Korea in particular. In 2022, $15\,000$ FCEVs passenger cars were sold in the world. In contrast, 7.3 million BEVs were sold in the world in the same time period. Within the commercial vehicle segment, $58\,000$ BEVs were sold in 2022. Worldwide, about $15\,000$ buses and commercial vehicles were sold as FCEVs in the same period. While BEVs have a market advantage over FCEVs in the passenger car segment, the trend for commercial vehicles is not yet equally clear. Many national resolutions suggest the use of FCEVs for long-distance commercial vehicles due to their short refueling times and greater range. Based on the available numbers the Asian market is most likely to adopt the FCEV in

the long haul truck segment. Nevertheless, too many uncertainties are not yet clear, and therefore, it can't be concluded which technology will become which market share. [12]
For the fuel cell in mobile applications usually the PEM fuel cell is used. The PEM fuel cell is used due to its high power density and the resulting small construction volume [8, 13]. This is achieved by pressurizing the supplied air on the cathode side. Air compressors are typically used for this purpose. Different compressor technologies have been used in the development of hydrogen fuel cells. On the one hand, research has been done on positive displacement compressors, which include rotary and screw compressors. Dynamic compressors have also been studied [15, 16].
As a dynamic compressor, centrifugal compressors are more suitable for PEM fuel cells than positive displacement compressors. The centrifugal compressor generates air pressure at high speeds, has a low noise level, and is more efficient than positive displacement compressors [15, 16]. This makes the centrifugal compressor currently the most used solution for PEM fuel cells [17]. One of the challenges is that the system must be oil-free to meet the cleanliness requirements of the hydrogen fuel cell. In addition, high rotational speeds are required for the electric machine. An overview of the different technologies used in commercially available vehicles is given in Table 1.1. It can be observed that the trend for centrifugal compressors has been adopted by most of the available FCEV manufacturers. The individual fuel cell systems have a range of

Table 1.1: Compressors used in FCEV to supply air to a PEM fuel cell [17–19].

OEM	Toyota	Honda	Daimler	GM	Hyundai	SAIC
Model	Mirai	FCX Clariry	FCV A-Class, B-Class, F-Class	Chevrolet Equinox	FCV ix35	Roewe 950
Air supply	Roots	2-stage Centrifugal	Centrifugal	Centrifugal	Blower	Centrifugal
H_2 pressure	700 bar	700 bar	700 bar	700 bar	700 bar	700 bar

applications, from a few kilowatts to around 150 kW of output power, which is

also analyzed in this work. For a 150 kW fuel cell, the compressor power falls within the range of 20 kW to 25 kW.

This work presents an approach for the holistic modeling of the centrifugal compressor, with a focus on the electric machine and its modeling. The unique aspects of the fast-rotating machine and the high circumferential speeds are also discussed.

1.2 Hydrogen Fuel Cell Applications

For optimal fuel cell systems in mobile applications, power density and system efficiency are essential. Power output is determined by the product of voltage and current, both of which are affected by internal system pressure. Fig. 1.1 (a) shows that increasing the air supply pressure in PEM fuel cells results in higher cell voltages and current densities [20]. It can also be seen in Fig. 1.1 (b) that the power output per surface area increases and therefore the power density. It is observed that an increase in pressure from 1 bar to 2 bar leads to an increase in power of 29 % at the optimum operating point. A further increase to 3 bar increases the power output by another 10 %. Increasing the supply pressure further to 4 bar results in an increase of 7.3 % compared to a supply pressure of 3 bar. It is clear that increased pressure can increase voltage and current output, and therefore power output. Pressures beyond 3 bar have limited effect in further increasing power density. Pressurized operation can also help reduce the size of the humidifier and heat exchanger, thereby improving the power to volume ratio of the stack system. However, the pressure of fuel cell stack operation must be balanced against the effort required for compression and bonding technology to achieve stack tightness. For this reason, the ideal pressure range for fuel cell stack operation is between 2 bar to 3 bar [21–24]. In addition, the compressor must be capable of achieving the appropriate pressure ratios while taking into account the high altitude and high temperature conditions in which the FC will operate. Actively pressurized fuel cells have an advantage over naturally aspirated systems in that the compressor can compensate for low inlet pressure (altitude) and high inlet temperature conditions. In Fig. 1.2, the FC setup shown includes an electrically driven compressor, a fuel cell FC, and other necessary components. The electric compressor is driven by a permanent magnet synchronous motor (Permanent Magnet Synchronous Machine (PMSM)) with a Compressor (C) mounted on the shaft. The optional energy recovery device shown here is a Turbine (T), which can be replaced by another compressor if a higher pressure ra-

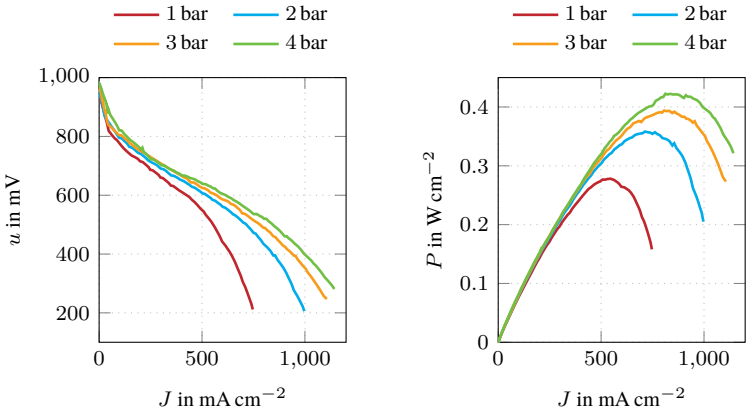

(a) Voltage characteristics

(b) Power characteristics

Figure 1.1: The effects of air pressure on fuel cell performance [20]

tio is required. The blue arrows indicate the airflow, which enters the compressor through a filter to prevent contamination that could damage the fuel cell. When the airflow leaves the compressor, it is typically at a temperature above $80\,^{\circ}\mathrm{C}$ and must be cooled by an Intercooler (IC). The airflow then passes through a Humidifier (HU) to increase the humidity and thereby improve the efficiency of the fuel cell [20]. The air reacts with hydrogen from a tank as it enters the fuel cell. The outgoing mass flow then contains water, which is then removed in a Water seperator (WS) to remove water droplets to prevent damage to the turbine stage. At the high circumferential speeds of more than $300\,\mathrm{m\,s^{-1}}$, a droplet hitting a turbine blade would otherwise cause damage to the turbine. The output voltage of the fuel cell is low compared to a high-voltage battery, so a DC/DC converter is used to charge a battery and store the energy temporarily. From the battery, the electric compressor is driven by an inverter (DC/AC). In total, the electric compressor typically consumes $10\,\%$ to $20\,\%$ of the electric energy generated in the fuel cell. Inverters with high switching frequencies are used for the high-speeds of the PMSM. To keep machine losses low, three-level inverters or output filters are used in some applications. The load is then supplied from the battery. For a FCEV this would be the identical drive train as for a BEV.

As already mentioned, the electric compressor is using a significant amount of the produced energy of the fuel cell. Due to the isentropic efficiency of the compressor, which is usually below 80 %, the efficiency of the compressor is the critical component for the overall fuel cell efficiency. In [25] the authors investigated on how the compressor needs to be designed for an electric fuel cell turbocharger. Overall, the results show that not only the compressor efficiency is relevant but also the whole operating range of the compressor and the fuel cell. The work has shown that a good control method can lead to a better system efficiency in the WLTP compared to a compressor, which has a higher maximum efficiency, but is not optimized to the requirements. The author concludes that it is necessary to design an optimized compressor geometry for a FC application. In this research, it is seen that common exhaust gas turbochargers have a ratio of

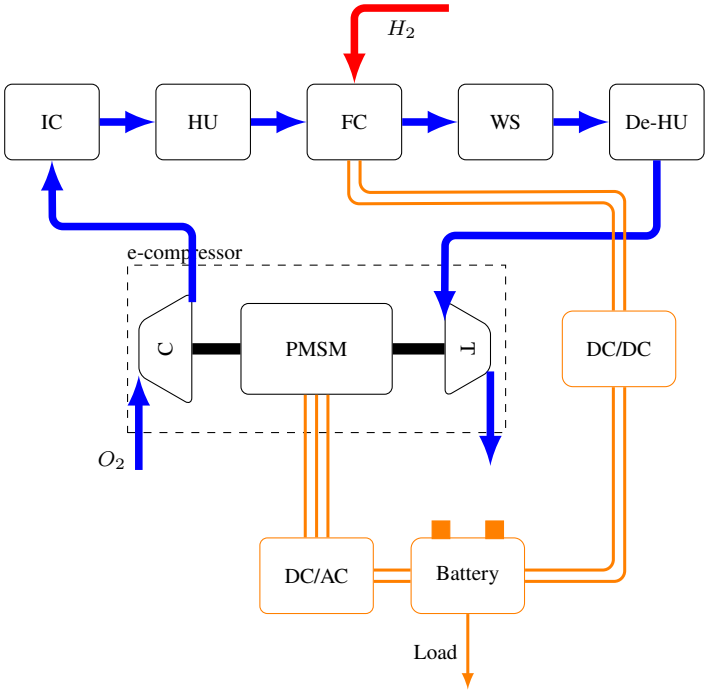

Figure 1.2: Fuel cell setup

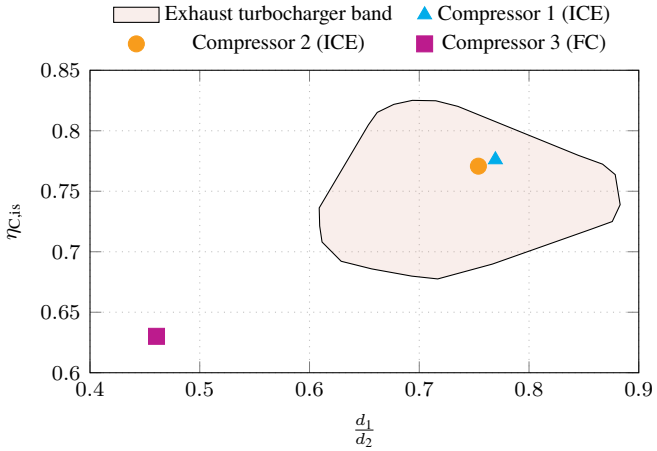

Figure 1.3: Compressor isentropic peak efficiency $\eta_{C,is}$ influenced by the ratio of inlet to outlet diameter $\left(\frac{d_1}{d_2}\right)$ and the comparison of the exhaust gas turbocharger [25].

compressor wheel inlet to outlet diameter of 0.6 , to 0.85 , as shown in Fig. 1.3. This ratio is also known as the trim of a compressor. A large trim results in a high efficiency because the airflow is not diverted as much compared to a wheel with a small trim [25]. In order to obtain the required air mass flow, the inlet cross-section is relevant. The mass flow is scaled with the inlet area and therefore with the free inlet cross-section [26]. Therefore, the cross-section for two compressors with the same mass flow requirement will have a similar large inlet diameter, but the outside diameter will vary depending on the trim and pressure ratio requirement. To achieve the required pressure ratio, the following correlation is known from the non-dimensional representation of the compressor map [26]:

$$\Pi_{\text{C,t-t}} = \left(\frac{\Psi {u_2}^2}{c_\text{p} T_1} + 1 \right)^{\left(\frac{\kappa}{\kappa - 1}\right)} \tag{1.1}$$

It can be seen that the circumferential speed at the tip diameter d_2 of the wheel, u_2 correlates to the square of the pressure ratio $\Pi_{\text{C,t-t}}$. Ψ denotes the pressure head coefficient, which is a dimensionless description of the pressure ratio. The

isentropic exponent is given by κ. Furthermore, c_p describes the heat capacity at constant pressure of the medium and T_1 the inlet temperature. Therefore, the compressor with the large trim will have a higher rotational speed compared to the compressor with the smaller trim to achieve the same pressure ratio. This can lead to different challenges for the electric machine as seen in Section 2.2.2. On the one hand, the increased speed will reduce the efficiency and on the other hand, it increases the thermal challenges in the system. It is therefore concluded that the design of an electric driven compressor is highly dependent on the design of the compressor as it defines the speed of the system and most importantly the efficiency of the system.

1.3 Research on High-Speed Machines for FC-Applications

The use of high-speed machines for FC applications has been the subject of many works, as summarized in Table 1.2. As mentioned in [27], it is an interdisciplinary design topic that includes the design of the aerodynamic components, the structural design, the magnetic design and the thermal design of the system. The published articles were subjected to a comparative analysis with respect to the listed topics, and the areas covered were noted. As observed, only a limited number of topics have been addressed in the published resources. The majority of the work has focused on the aerodynamic design of the compressor. The magnetic design represents the second most studied topic in the research of FC air compressors. In contrast, thermal design has been the least studied area. Commercial air compressors are shown in Table 1.3. Using the available information, it is possible to identify the operating range of a fuel cell compressor by considering the mass flow and pressure ratio given in the compressor specification. It is important to note that not all information may be available for all systems, resulting in incomplete data. Additionally, in cases where stack power was not available, an estimate of mass flow was made using [28]:

$$\dot{m}_\mathrm{FC} = \frac{3.58 \cdot 10^{-4}\, \lambda_\mathrm{FC} P_\mathrm{FC}}{u_\mathrm{cell}} \tag{1.2}$$

In here λ_FC is the air stoichiometry, the value is usually about 1.7; P_FC is the power of the PEM fuel cell system in kW and u_cell is the average cell voltage, and the value of it is $0.65\,\mathrm{V}$. Since it is a summary of the available compressors, the applications for the compressors are not known. Two systems stand out from the

rest due to their significantly lower or higher speeds. The first system, operating at $15\,900\,\mathrm{min}^{-1}$ includes a gearbox that allows the motor to operate at lower speeds [29]. The second system has speeds exceeding $250\,000\,\mathrm{min}^{-1}$, making it suitable for small fuel cells. All other systems operate within the range of $50\,000\,\mathrm{min}^{-1}$ to $135\,000\,\mathrm{min}^{-1}$ [30].

Table 1.2: Summarized research literature on the topic of air compressors for fuel cell applications. Divided into the different research sections aerodynamic, structural, magnetc and thermal design.

Aerodynamic	Structural	Magnetic	Thermal	$\dot{m}_{FC}$ $g\,s^{-1}$	$\Pi_{C,t\text{-}t}$ -	n_{max} 1×10^3 min	Year	Reference
x				253	3	5	2000	[31]
x				76	3.2	110	2003	[32]
		x		-	-	10	2005	[33]
x				300	2.2	50	2006	[34]
	x			-	-	120	2006	[35]
x				150	1.8	24	2008	[36]
	x	x		-	-	120	2012	[37]
x				11.4	1.5	250	2012	[38]
x				150	2.4	201.5	2016	[29]
x				2000	4	30	2016	[39]
x				80	2.2	100	2017	[17]
x				70	2.2	120	2018	[40]
x				110	2	135	2019	[27]
x				100	3	100	2020	[41]
x		x		14.7	1.6	280	2021	[30]
	x	x		102	2.3	110	2021	[42]
x	x	x		60	2.3	100	2021	[43]
x				120	2.2	100	2021	[25]
x			x	68	-	90	2022	[44]
	x	x	x	730	1.6	50	2022	[45]
		x		-	-	90	2022	[46]
x	x	x		120	3.5	90	2022	[47]
x				120	2.3	90	2023	[48]

Table 1.3: Overview of public data for fuel cell air supply compressors. (*) FC stack power has been estimated with eq. (1.2).

P_C kW	n 1×10^3 min	P_{FCS} kW	$\Pi_{C,t\text{-}t}$ -	$\dot{m}$ g s^{-1}	Reference
12	135	100	2	110	[27]
14.4	110	92*	2.3	102	[42]
10	100	40	2.3	60	[43]
12	120	-		-	[35]
15	120	-	-	-	[37]
-	100	72.5*	2.2	80	[17]
-	50	272*	2.2	300	[34]
-	15.9	150	2.4	150	[29]
-	100	36*	3	40	[41]
-	110	69*	3.2	76	[32]
32	92	150 to 260	2.5	320	[49]
22.5	120	70 to 150	2.6	150	[49]
5	150	30 to 70	2.1	77	[49]
-	-	10 to 15	2.6	15	[50]
-	-	15 to 30	2.5	40	[50]
-	110	30 to 50	2.5	58	[50]
-	95	50 to 100	2.5	108	[50]
-	95	90 to 150	2.8	144	[50]
-	-	100 to 130	3.3	144	[50]
-	-	120 to 140	3.2	180	[50]
-	-	250 to 280	3.6	360	[50]
1	280	5 to 15	1.6	13	[30]

1.4 Structure of the Thesis

The first chapter introduces the work, focusing on hydrogen fuel cells for mobile applications and why an electric compressor is needed. It also explains the need for an electric compressor in a FC system. An overview of the research on electric compressors in the application is given.
The second chapter covers the basics of high-speed electric machines, including

different applications and machine types, as well as the challenges in their design.
The third chapter deals with the modeling of the compressor, including its scaling and the dimensioning of the turbine. In addition, the mechanical design of the rotor shaft is described, including the strength calculation of the retaining sleeve and the magnet. The magnetic design of high-speed machines is also described, and a new approach to calculating air gap flux density is presented. Losses of the machine are calculated and the temperature distribution in the electric machine is determined by a 2D FEA.
After modeling, the reference machine that was designed and built as part of this work is presented in the fourth chapter. It was not designed using the modeling presented here, but using conventional FEA. Therefore, this machine can be used as a reference for validation of the presented methodology.
Chapter 5 describes the validation of the machine, which is compared to all aspects of the modeling in Chapter 3 to verify its quality.
Chapter 6 transfers the developed system modeling to a wide range of applications by extending the application range and analyzing systems with a compressor power of $10\,\mathrm{kW}$ to $40\,\mathrm{kW}$. The study demonstrates the trade-off between minimizing losses and minimizing footprint using a two-parameter optimization approach. In addition, the effect of circumferential speed on system characteristics is analyzed.
The final chapter provides a summary of the work and suggests areas for future improvement.

Chapter 2

High-Speed Electric Machines

This chapter provides an overview of high-speed electric machines. As will be shown in the further sections of this work, *high-speed* is used synonymously with high circumferential speeds. This definition was proposed in [51]. There, high-speed starts at a circumferential speed of $100\,\mathrm{m\,s^{-1}}$ and goes up to $250\,\mathrm{m\,s^{-1}}$. The limit of $250\,\mathrm{m\,s^{-1}}$ was exceeded in some publications, induction machines (IMs) and synchronous machines (SMs) were designed, which have higher circumferential speeds. The basics of electric machines can be found in the works of [52, 53]. In addition to the applications of high-speed electric machines, this chapter discusses the design challenges associated with higher speeds. The design aspects described cover magnetic design, mechanical design, and thermal design.

2.1 Applications of High-Speed Electric Machines

High-speed electric machines are of interest in a number of applications. One reason for using electric machines instead of conventional drives, such as internal combustion engines or hydraulic drives, is the demand for a small CO_2 footprint. [54].

2.1.1 Oil and Gas Applications

As already mentioned, high-speed does not imply a high rotational speed. Gas compression is required at many points in the chemical, oil and gas industries, primarily for gathering, transmission and downstream processing of the gas. To reduce the carbon footprint, electric drives are used instead. Other benefits of a high-speed electric drive include an oil-free application when magnetic bearings are used and the ability to connect directly to the compressor. This eliminates the gearbox and the entire lubrication system, resulting in increased efficiency, availability and safety. [54, 55]
In [55, 56] the power range for this application is given from 3 to 15 MW and a speed range from 6000 to 15 000 min^{-1}. IMs are mainly used for these applications, but SMs with permanent magnet rotors are also used with a retaining sleeve to hold the magnets in place. For the IMs, a laminated rotor design is possible as well as a massive solid rotor design. The maximum tip speed of a laminated rotor is approximately 180 $\mathrm{m\,s}^{-1}$, while it can be increased to 250 $\mathrm{m\,s}^{-1}$ for a solid rotor design. In the solid shaft design a technology is used, which forms a bond on atomic base between the rotor squirrel cage and the steel body of the shaft. Thus, the shaft can be considered as one piece. Another option for a solid shaft design is to mill open slots into the steel rotor and no copper is used [56]. More details on the rotor design of high-speed electric IM and SM are provided in Section 2.2.1.

2.1.2 Air Compressors and Blowers

The use of electric driven air compressors is a fast growing market for high-speed machines. In 2011, air compression for industrial processes consumed about 60 TW h per year in the EU [57]. At the same time, net electricity generation in the EU was 2789 TW h and therefore air compression is responsible for 2.2 % of total consumption [58]. For the US, [57] mentions figures of up to 16 % of net electricity consumption. Various studies give different ranges, which are summarized in [59]. It is also mentioned that one way to increase the efficiency of these systems is to use variable speed drives and high efficiency electric machines.
One application that is coming into focus is the use of electric air compressors to supply oxygen to a hydrogen fuel cells. The application is described in detail in Section 1.2. The use of compressed air increases the efficiency and power density of the overall system, which is especially important for mobile applications [20]. In addition, energy can be recovered by feeding the fuel cell exhaust gas into a

turbine on the other side of the rotor [25]. Directly driven compressors are able to run oil free and therefore prevent any pollution in the process air if necessary. Applications like this could be in the food and beverage industries, pharmaceutical industries and high quality painting industries [54]. The power requirement varies from up to $400\,\mathrm{kW}$ and $65\,000\,\mathrm{min}^{-1}$ to $15\,\mathrm{kW}$ and $150\,000\,\mathrm{min}^{-1}$. For lower pressure ratios, centrifugal blowers can be used. Blowers are usually defined by their lower pressure ratio, which is in the range of 1.2 to 1.8 [60]. They can be used, for example, in wastewater treatment plants. When using centrifugal blowers, the drive requires a high-speed machine. Direct driven centrifugal blowers therefore offer the highest efficiency compared to conventional blower systems.

2.1.3 Spindles

Spindles are used in cutting processes. High tool speeds are required to ensure high volumetric material removal. Belt drives have been used for low-cost solutions, but this solution is limited by the maximum rotational speed. The focus of research and development has shifted to the development of directly driven tools using high-speed motors. Drilling, grinding, and milling are the main spindle applications. The different speeds required for milling applications in different materials are shown in Table 2.1. As can be seen, the speed for milling is highly dependent on the material that is being machined. For grinding, the speed is much higher and can be higher than $100\,000\,\mathrm{min}^{-1}$.
Three types of motors are used for spindle applications. IMs are the most common due to their simplicity and robustness. Switched Reluctance Machine (SRM) are also in use but their power factor is low in comparison to PMSM which are the solution of choice for higher speeds. The total power and speed

Table 2.1: Typical milling applications speed [61].

Applications	n in min^{-1}
Metal	4500 – 12 000
Stones	8000 – 12 000
Glass/Marble	8000 – 12 000
Wood	18 000 – 25 000
Aluminium	30 000 – 40 000

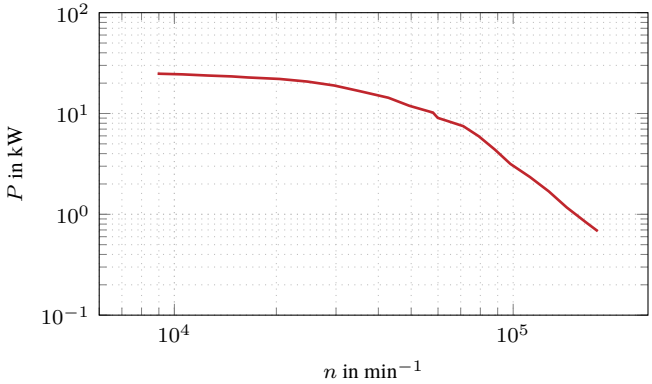

Figure 2.1: Rotational speed of spindles and their power requirement. [61]

requirements can be seen in Fig. 2.1. The maximum power requirement is 24 kW at 9000 min^{-1} and reaches 180 000 min^{-1} and 1 kW. Demands for higher speeds are already known and published by [62] with the goal to reach 1×10^9 min^{-1}. [61]

2.1.4 Turbo Molecular Pumps

Turbomolecular pumps are used to create and maintain the high vacuum levels required for many research and industrial applications. The creation of a vacuum environment by a Turbomolecular Pump (TMP) is essential in the production of semiconductors, dye chemicals, plastics and solar cells. Vacuums of up to 1×10^{-11} mbar can be achieved with TMP [63]. To meet the requirements of TMP applications, motors are needed that can achieve high speeds up to 90 000 min^{-1} at relatively low power levels. Achieving this requires a sophisticated machine design. During the operation of a TMP, the rotor is subjected to high-speeds in a deep vacuum, which can lead to potential heat exchange problems [64]. These heat exchange problems arise because heat dissipation is limited to radiation due to the vacuum environment. In addition, the high-speeds within the TMP result in the accumulation of frictional heat, further constraining the design. Magnetic and/or ceramic shaft bearings are used to minimize friction and prevent oil contamination. However, the use of these high quality materials comes at a cost. Due to the high-speed and low power of the pump, the mar-

ket is predominantly dominated by PM brushless DC motors as the preferred choice for TMPs. The choice of PM machines has become very noticeable as manufacturers offer magnetically levitated shaft bearings, which are either permanent magnets for small pumps or a combination of dynamic and permanent magnetic fields for contactless shaft support. These TMP provide bearings that never degrade and ensure a true absence of oil vapor backstreaming. [54, 65]

2.1.5 Micro Gas Turbine

A Micro Gas Turbine (MGT) refers to a compact gas turbine that integrates a high-speed electric generator on a single shaft. It can reach speeds of up to $120\,000\,\mathrm{min}^{-1}$, while typical power ratings range from $30\,\mathrm{kW}$ to $1\,\mathrm{MW}$. These turbines are primarily used in stationary power generation scenarios where space is limited. They can be fueled by a variety of fuels such as natural gas, biogas, propane, butane, diesel, and kerosene. Microturbines have few moving parts, high efficiency, low emissions, and have waste heat recovery capabilities to maximize efficiency to achieve overall efficiencies above $80\,\%$. [66]. MGT operate in a narrow speed range and require high power density, making Surface Mounted Permanent Magnet Synchronous Machine (SPMSM) the preferred choice. The microturbine system consists of several components, including a compressor, combustor, turbine, alternator, and optionally a heat exchanger and generator. In non-recovery systems, the process involves mixing compressed air with fuel, which is then combusted under constant pressure conditions. The resulting hot gas expands through a turbine, generating useful work. Simple cycle microturbines offer advantages such as lower cost, higher reliability, and a greater amount of heat available for combined heat and power (CHP) applications compared to recuperated units. Recuperated MGT incorporate a sheet metal heat exchanger that recovers some heat from the exhaust stream. This recovered heat is then transferred to the incoming airflow. The preheated air is used in the combustion process. By preheating the air, less fuel is required to reach the desired temperature at the turbine inlet. Recuperated units have higher efficiencies and thermal-to-electric ratios than nonrecuperated units. In addition, they result in fuel savings of approximately $30\,\%$ to $40\,\%$ due to the preheating process. [65, 67]

2.2 Design of High-Speed Electric Machines

In this section, the various machine designs for different types of applications are introduced. The designs of the two main machine types, IM and SM, are shown and compared. Further, the design challenges of high-speed machines are explained.

2.2.1 State-of-the Art

As seen in Section 2.1, the variety of applications and power ranges for high-speed drives vary a lot. Different types of machines are used in a wide range of applications. Published data is summarized in Table 2.2 and Table 2.3. All machines have a circumferential speed v_c greater than $100\,\mathrm{m\,s^{-1}}$. The speed range for IM goes up to $367\,\mathrm{m\,s^{-1}}$, while the speed range for SM reaches a limit earlier at $306\,\mathrm{m\,s^{-1}}$. In Fig. 2.5 all machines are compared in terms of speed n and output power P_{out}. The data set is divided into four groups. IM and SM are separated, and also the speed range is divided into $v_c < 200\,\mathrm{m\,s^{-1}}$ and $v_c > 200\,\mathrm{m\,s^{-1}}$. IMs are mainly used for lower speeds ($n < 100\,000\,\mathrm{min^{-1}}$) and high power requirements.

2.2.1.1 High-Speed Induction Machines

In Figs. 2.2 (a) to 2.2 (d) the four different rotor designs used in high-speed IM are shown. A solid metal shaft, shown in Fig. 2.2 (a), is the simplest rotor design. It has its advantages at the highest circumferential speeds due to its mechanical robustness. The disadvantage of the design is the relatively high resistivity of the shaft material and therefore a low efficiency of the machine [68]. At the rotor surface, the harmonic flux components are concentrated and cause significant losses. Thus, the rotor losses limit the overall power density of the machine. In addition, the eddy currents counteract their cause and push the time-varying magnetic field out of the rotor.
The axially-slitted solid rotor, shown in Fig. 2.2 (b), represents an advancement over the smooth solid rotor configuration by incorporating axial slots into the rotor surface [69]. The purpose of this slitting technique is to direct the fundamental flux component into the rotor while providing a higher impedance path for eddy currents flowing along the rotor surface. However, it is important to note that slitting results in an increase in air gap friction losses, which can potentially outweigh the benefits of reduced eddy current losses, especially at the circumferential speeds being considered. In addition, the mechanical strength of

the rotor is compromised by the presence of slots and the resulting notch stresses. Another advancement in rotor design is the application of a copper alloy coat-

Table 2.2: High-speed IM in literature, sorted in order of circumferential speed. [65]

v_c $\mathrm{m\,s^{-1}}$	Rotor OD mm	Type	P_{out} kW	n 1×10^3 min	Ref.
367	70	solid coated	60	100	[70]
342	109	solid coated	300	60	[71]
290	369	laminated	2000	15	[72]
283	90	solid coated	60	60	[73]
250	398	laminated	8000	12	[74]
236	90	solid caged	50	50	[73]
204	325	solid slitted	8000	12	[69]
193	330	solid caged	2610	11.16	[75]
185	118	laminated	100	30	[76]
182	348	laminated	6000	10	[77]
180	39	laminated	10	90	[78]
177	28	solid	6.3	120	[68]
176	24	laminated	0.63	140	[79]
168	80	laminated	35	40	[80]
153	195	laminated	350	15	[81]
144	90	solid coated	0.7	24	[73]
140	89.1	laminated	200	30	[82]
138	50	laminated	65	30.6	[73]

ing to the solid rotor, resulting in electromagnetic anisotropy [83, 84], as shown in Fig. 2.2 (c). This copper alloy coating serves the dual purpose of acting as an infinite number of rotor bars and end rings. Such a design not only maintains mechanical robustness, but also achieves higher efficiencies compared to the simple solid rotor configuration. In [71] a 300 kW, 60 000 $\mathrm{min^{-1}}$ IM with a copper-coated solid rotor used in an air compressor application is shown. This particular topology is commonly used in machines with the highest circumferential speeds, as indicated in Table 2.2. However, it should be noted that the presence of the coating results in a significantly larger magnetic air gap between the stator iron and rotor iron compared to induction machines with copper bars, resulting in a poorer power factor. In [73, 85] the authors have conducted a study

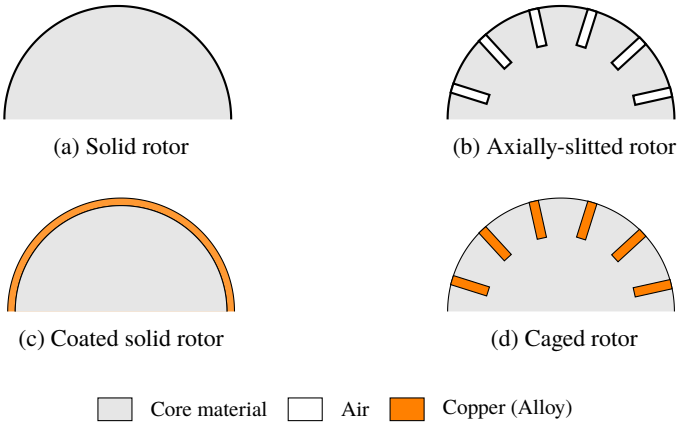

Figure 2.2: IMs solid rotor designs for high-speed applications. Only one half of the rotor is shown.

exploring the use of a solid rotor combined with a squirrel cage as shown in Fig. 2.2 (d). This innovative rotor design aims to utilize the mechanical strength of a solid rotor while taking advantage of the electromagnetic performance associated with a squirrel cage rotor. The research highlights certain challenges in manufacturing this particular topology in terms of drilling slots in solid steel. As a result, the designs feature open rotor slots. The authors compare the squirrel cage solid rotor to an existing copper coated solid rotor in a 60 kW, 60 000 min^{-1} machine. The results indicate that squirrel cage rotors improve power density and efficiency compared to the coated rotor. It is important to note, however, that this improvement comes at the expense of reduced mechanical robustness. In [74], different solid rotor designs are compared against a laminated rotor topology. The results show the laminated configuration's higher efficiencies and higher power factor. So, laminated technology is preferable when mechanical loads can be handled.

2.2.1.2 High-Speed Permanent Magnet Machines

Permanent magnet machines are mostly used to achieve higher efficiencies compared to IMs and higher power densities. In Table 2.3 a selection of different machines found in literature are sorted by circumferential speed. Compared

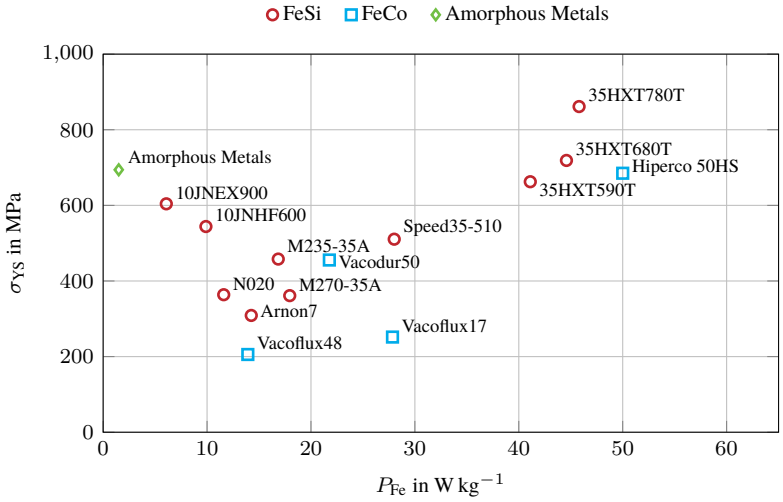

Figure 2.3: Yield strength over the core losses at a magnetic flux density of 1 T and a frequency of 400 Hz for various core materials. [65, 86]

to the IMs shown before, the rotor outer diameter has a maximum of 150 mm compared to almost 400 mm. The speed range goes up to 306 m s^{-1}. Surface Mounted Permanent Magnet Synchronous Machines (SPMSMs) are typically used in preference to IPMs for high-speed applications. Two reasons explain this phenomenon. First, loads in high-speed machine applications often require more torque at higher speeds, which SPMSMs meet well since they provide constant torque. Second, a non-magnetic, high-strength sleeve can withstand the high loads typically encountered in such applications. This increases the air gaps in high-speed machines. To reduce the air gap length and improve magnetic performance, IPM could be considered. An IPM's design in [87] relies on the strength of its core material. Notch stresses in the rotor limit its high-speed performance. Another limitation is the relationship between yield strength and core loss shown in Fig. 2.3. Material strength generally decreases as core losses decrease, except for high silicon steels like 10JNEX900, 10JNHF600 and amorphous metals. This causes high rotor losses and the risk of too high temperatures at the magnet. High-strength electrical steel sheets can't match the performance of the sleeve material in SPMSMs because they lack the specific strengths needed

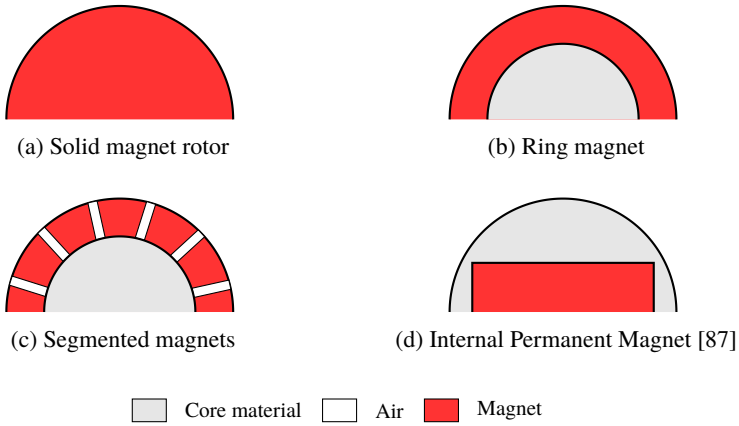

Figure 2.4: Main rotor concepts for High-Speed Permanent Magnet Synchronous Machine (HSPMSM), sleeve is not shown in the drawing for designs in (a)-(c). Design of the Internal Permanent Magnet Synchronous Machine (IPM) does not require a sleeve.

for this purpose. As the comparison shows, three main groups of materials are used as sleeve materials: Inconel, titanium, and fiber-reinforced plastics, which can be reinforced with glass or carbon fibers. According to [56], SMs have some disadvantages compared to IMs, for example, material availability, handling of the rotor, a reduced lifetime and also cost [54].
In the rotor design of HSPMSMs the four designs shown in Figs. 2.4 (a) to 2.4 (d) are used. The sleeves are not shown in the sketches, but are mandatory for high speed applications, except for the solution shown in Fig. 2.4 (d). The first design in Fig. 2.4 (a) uses a solid magnet. It maximizes the magnet material per rotor volume and increases the demagnetization strength of the machine [88]. The ring magnet (Fig. 2.4 (b)) and the segmented magnet (Fig. 2.4 (c)) have the same magnetic performance, but the segmentation reduces the sleeve stresses.
All machines shown in Tables 2.2 and 2.3 are compared in Fig. 2.5. Dividing the data into two groups of v_c shows that increasing v_c allows for higher performance. For $v_c < 200\,\mathrm{m\,s^{-1}}$ the maximum speed limit is at $n < 150\,000\,\mathrm{min^{-1}}$. Higher speeds can only be achieved with higher circumferential speeds. For SMs, the vast majority of machines in these applications are designed with surface mounted magnets.

Table 2.3: High-speed SM in literature, sorted in order of circumferential speed. [65]

v_c m s^{-1}	Rotor OD mm	Type	Sleeve Material	P_{out} in kW	n 1×10^3 min	Ref.
306	39	SPMSM	titanium	15	150	[88]
294	47	SPMSM	titanium	22	120	[89]
292	37.2	SPMSM	glas fibre	15	150	[88]
288	25	SPMSM	carbon fibre	2	220	[90]
261	10	SPMSM	titanium	1	500	[91]
251	20	SPMSM	Inconel	5	240	[92]
233	89.4	SPMSM	SiFe	11	50	[77]
230	22	SPMSM	titanium	2	200	[93]
213	34	SPMSM	Inconel 718	15	120	[37]
200	24.5	SPMSM	carbon fibre	1.5	150	[94]
192	24.5	SPMSM	glass fibre	1.5	150	[95]
175	83.6	SPMSM	carbon fibre	40	40	[96]
172	16.48	SPMSM	titanium	2	200	[97]
161	77	SPMSM	carbon fibre	40	40	[98]
130	20	IPM	Amorph. metal	15	125	[87]

2.2.2 Design Challenges

In the next section, design challenges of HSPMSM will be explained. First, the mechanical challenges will be discussed. Second, the electrical challenges, including losses, are discussed, which leads directly to the third topic, thermal management of the machine.

2.2.2.1 Mechanical

This section describes the loads on the rotor assembly. First, the basic loads are explained. Second, the material selection for the sleeve and the magnet is discussed. Finally, the overall challenges are briefly addressed.

Rotor Loads

The rotor assembly faces a number of different loads that add up. The loads are independent of the rotor design of the SPMSM. The magnet requires a support

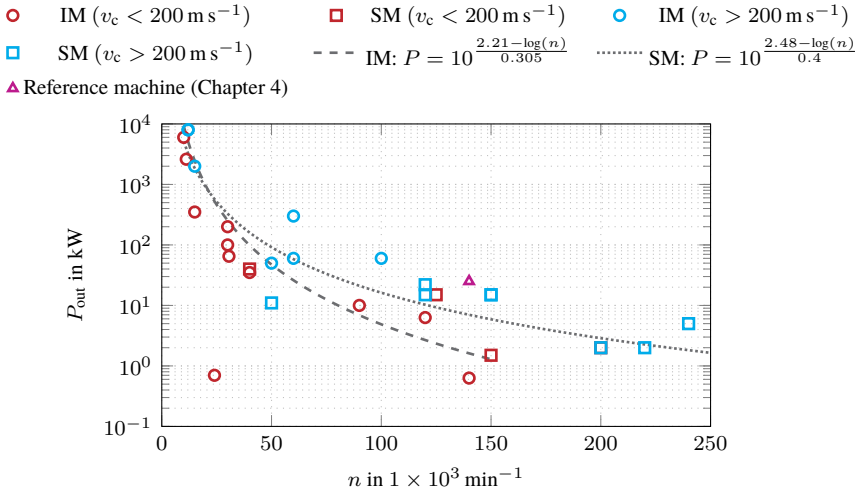

Figure 2.5: High-speed machines compared to each other in reference to rotational speed and power output.

sleeve because it is not capable of withstanding high tensile loads. Therefore, the most important design consideration is to ensure that the rotor assembly is rigid and that the magnet is held in place under all conditions. It is also necessary to prevent the magnet from being overloaded in the tensile direction. The cylindrical coordinate system is used for these calculations. Therefore, compression is in the negative radial direction. Strain is in the positive radial direction.
The load cases can be divided into two main types. The first is the static load and the second is the dynamic load. The static load describes the load due to the interference fit required to create a compressive load on the magnet. The outer diameter of the magnet is larger than the inner bore diameter of the sleeve. For assembly, the sleeve is thermally joined by heating the sleeve and cooling the magnet. Then, the two parts can be assembled due to their thermal expansion. As the two parts are assembled and have reached similar temperatures again a compressive load is created on the magnet. The sleeve, on the other hand, is stretched in a positive radial direction.
The dynamic load case considers the loads resulting from the rotation of the shaft. Due to the centrifugal forces acting on the parts, both materials will elongate.

Since they are not materially bonded, the two components elongate separately. The elongation and stresses are proportional to the angular velocity ω^2. In addition to the two loads, the temperature dependent elongation has to be considered for both load cases. The magnet materials of Samarium Cobalt Alloy (Sm_2Co_{17}) or Neodym iron boron magnet (NdFeB) have different temperature expansions compared to the available sleeve materials. For example, NdFeB is often associated with thermal expansion rates smaller than $0\,\mathrm{W\,m^{-1}\,K^{-1}}$, perpendicular to the magnetization direction. In these cases, material selection becomes difficult because the operating temperature can cause significant elongation of the sleeve material if metallic materials are used. Fiber-reinforced sleeves therefore have lower coefficients of expansion.

Sleeve Materials

As seen in the previous part, the material selection for SPMSM sleeves comes down to four materials. These four materials can be divided into two main groups. Firstly, non-magnetic metals and secondly, fiber reinforced plastics. The metals typically used are Titanium and in particular TiAl6V4 or Inconel 718. The choice of material is limited to non-magnetic materials for obvious reasons. In addition, the material should have a high electrical resistivity to minimize eddy current losses. The main focus on the material is the specific strength. Just looking at the stresses caused by the rotation of the shaft, it can be deduced that the ratio of the yield strength σ_{YS} and the material density ρ ($\frac{\sigma_{\mathrm{YS}}}{\rho}$) must be maximized to minimize the sleeve thickness. With a minimal sleeve thickness the influence on the magnetic performance is reduced. The result of this design approach is a sleeve with minimal sleeve thickness. In Fig. 2.6 a material selection diagram of non-magnetic materials is shown. The x-axis shows the derived parameter $\frac{\sigma_{\mathrm{YS}}}{\rho}$ and the y-axis shows the resistivity of the sleeve material. The resistivity is the second important parameter to include in the material selection to reduce the losses in the sleeve. Besides the resistivity, the thickness of the material also affects the amount of losses, since they are proportional to $\frac{t_{\mathrm{S}}}{\rho_{\mathrm{el}}}$. Therefore, materials on a line with a slope of -1 will have equal performance in terms of thickness and losses. Moving the line further to the upper right corner will eliminate the least fitting materials first. There are four major groups of materials in the figure. In brown are the fiber reinforced plastic materials, in purple are the titanium materials, in red are the nickel based materials and in turquoise are the stainless steel materials. The most often used materials are summarized with specific parameters in Table 2.4.

Table 2.4: Mechanical properties of Inconel 718, TiAl6V4 and Carbon Fiber Reinforced Materials (CFRP) and Glas Fiber Reinforced Materials (GFRP) [99, 100].

Material	ρ	E	ν	α	σ_{YS}	ρ_{el}
	$\mathrm{kg\,m^{-3}}$	GPa	-	$\mathrm{\mu m\,m^{-1}\,K^{-1}}$ ($\parallel$ / $\perp$)	MPa	$\mathrm{\mu\Omega\,cm^{-1}}$
Inconel 718	8221	203	0.296	13.1	1090	120
TiAl6V4	4430	114	0.342	8.9	880	170
CFRP	1550	135	-	0.2/30	2200	3030
GFRP	1900	45	-	8/35	1200	$\rightarrow\infty$

Besides material strength, sometimes also expressed as $\sqrt{\frac{\sigma_{\mathrm{YS}}}{\rho}}$, thermal conductivity has a significant impact on machine performance [101]. Fiber-reinforced sleeves have lower losses due to their high resistivity, but they also have lower thermal conductivity. Therefore, most of the rotor losses are in the magnets of the rotor. The thermal conductivity is not as high as for metal sleeves and therefore the resulting magnet temperature can be higher.

Magnet Material

HSPMSMs are selected when the application requires high power densities. The most common material is Sm_2Co_{17} due to its high temperature capability. The second material with even higher energy density at room temperature is NdFeB. The disadvantage of NdFeB is the lower temperature resistance. The operating maximum is at $T_{\mathrm{M}} = 180\,^{\circ}\mathrm{C}$ compared to $T_{\mathrm{M}} = 250\,^{\circ}\mathrm{C}$ for Sm_2Co_{17}. The temperature gradient for the remanence flux density of NdFeB is $0.12\,\%\,\mathrm{K^{-1}}$ compared to $0.035\,\%\,\mathrm{K^{-1}}$. From a mechanical point of view, both materials have high compressive strength, which is usually sufficient for all load cases. The main disadvantage of both materials is their low tensile strength. The Sm_2Co_{17} has a tensile strength of $35\,\mathrm{MPa}$ to $40\,\mathrm{MPa}$ compared to a tensile strength of $75\,\mathrm{MPa}$ for NdFeB. The choice of material must be carefully considered and is always specific to the application of the electrical machine. The thermal expansion of NdFeB can become negative perpendicular to the direction of magnetization, which can cause problems with the compression of the magnet at high temperatures. Both material properties are summarized in Table 2.5. In Fig. 2.7 the magnetization and demagnetization characteristics of NdFeB and Sm_2Co_{17} are

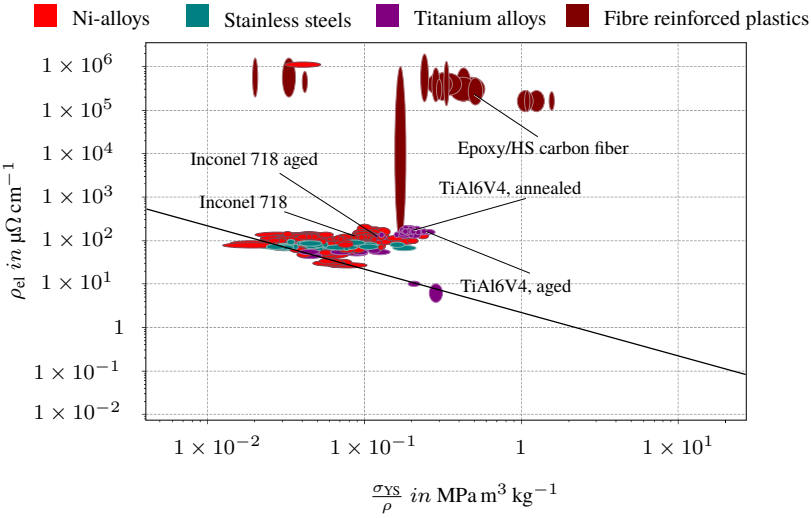

Figure 2.6: Material selection diagram for a hollow rotating disc. Y-axis showing the electric resistivity and the specific yield strength on the x-axis. Four material groups are shown which are suitable for sleeves: Nickel based alloys, stainless steels, titanium alloys and fiber reinforced plastics. Fiber reinforced plastics are the best suited materials with High-strength (HS) carbon fibers in the upper right of the graph, which indicates a high resistivity and a high specific strength.

Table 2.5: Comparison of magnet materials NdFeB and Sm_2Co_{17}. Thermal expansion factor α in $\parallel$ and $\perp$ direction relative to the magnetization direction, temperature coefficient of induction $\alpha(Br)$, Young's modulus E, Poisson's ratio ν, tensile strength σ_t, compression strength σ_c, density ρ, and maximum operating temperature T_{max}. [D1–D4]

Material	α µm m^{-1} K^{-1} ($\parallel$ / $\perp$)	$\alpha(Br)$ % K^{-1}	E GPa	ν -	σ_t MPa	σ_c MPa	ρ kg m^{-3}	T_{max} °C
NdFeB	7/−1	−0.12	150	0.24	75	1050	7600	180
Sm_2Co_{17}	11/13	−0.035	160	0.27	40	800	8300	250

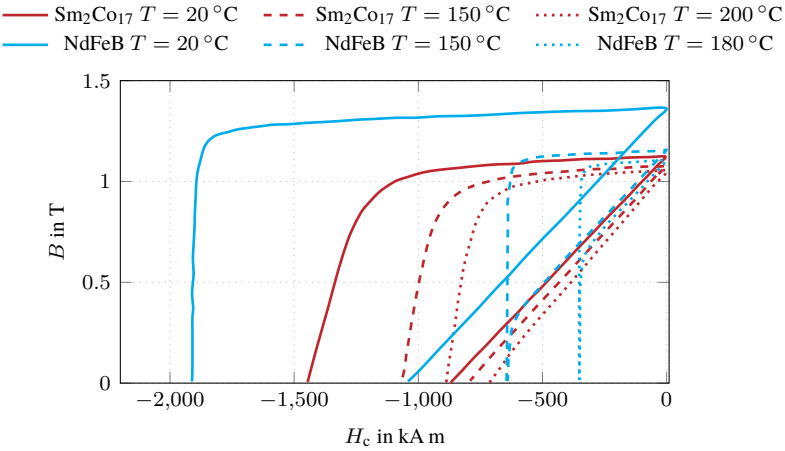

Figure 2.7: Magnet Material Magnetization Curves for NdFeB of the type N45UH and Sm_2Co_{17} of the type 32H. [D1, D5]

shown under different temperature conditions. The horizontal axis represents the magnetic field strength H_c, while the vertical axis shows the magnetic flux density B. The curves corresponding to NdFeB and Sm_2Co_{17} are plotted for temperatures of 20 °C, 150 °C, 180 °C, and 200 °C, with each material and temperature condition distinguished by specific line styles. For the NdFeB there is no demagnetization curve above 180 °C. It can be noticed that the knee point of the NdFeB magnet is visible in the quadrant shown and there is a risk of demagnetization during operation. This area is not visible for the Sm_2Co_{17} for temperatures up to 200 °C.

2.2.2.2 Losses

The limitations of HSPMSM are mechanical. High rotational speeds also lead to high frequency dependent losses and therefore challenges to the thermal management of the machine. The losses that occur in the machine are described in the following section.

Copper Losses

A major component of total losses are copper losses. This loss contribution can

be divided into three main parts. First, the direct current (DC) losses or ohmic losses that occur due to the winding resistance. Second, the losses due to skin effect and proximity effect. And third, the current displacement caused by an external field. The skin effect is a phenomenon in which high-frequency AC currents tend to flow near the surface of a conductor rather than through its entire cross-section. The proximity effect is a phenomenon in which the magnetic fields of adjacent conductors carrying high-frequency AC currents interact, causing a distortion in the distribution of current within each conductor. Both effects result in an increase in resistance and a corresponding decrease in current carrying capacity at higher frequencies. Both of these effects are important in high frequency applications. For electric machines with electric frequencies below 3 kHz, the skin effect will play a minor role since the skin depth is still 1.2 mm. The frequency dependent skin depth is calculated with:

$$\delta = \sqrt{\frac{2\rho_{\mathrm{el}}}{\omega\mu_0\mu_{\mathrm{r}}}} \tag{2.1}$$

In the equation given, ρ_{el} is the conductor resistivity, ω is the speed of rotation, μ_{r} is the relative permeability of the conductor, and μ_0 is the permeability of free space. The diameter of a single winding is expected to be significantly less than twice the skin depth. Regarding the DC losses, a notable property is that a large fraction of the losses occur in the winding head, especially for distributed windings. Due to its configuration and the fact that there is typically only a single pole pair, the winding head forms a large arc. Consequently, it is possible for more than 50 % of the losses to accumulate in the winding head. This phenomenon is critical to consider in the design of electric machines, as cooling the winding head is typically more challenging than cooling the windings in the slots.
Eddy current losses are primarily influenced by the external magnetic field. The conductors in the slots and the permanent magnets generate a magnetic flux in the stator core. While this flux is primarily concentrated in the core material, it also extends into the slots, resulting in what is called leakage flux. The leakage flux in the slots produces an alternating magnetic field, which in turn causes eddy currents in the conductors. These eddy currents increase the current density on the side of the conductor facing the slot opening. According to Ampère's law, the leakage flux near the slot opening increases, resulting in a concentration of current toward the slot opening. These effects are illustrated in Fig. 2.8.
Such phenomena are of particular importance in automotive applications, where hairpin windings characterized by large conductor cross sections are increasingly used [102, 103]. These effects have also been studied in [104] for high-speed

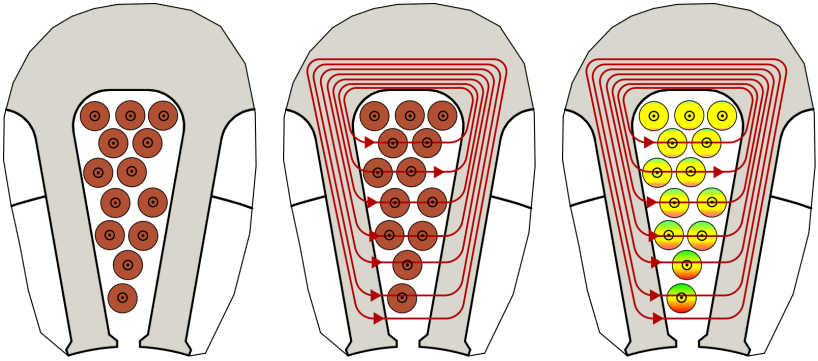

(a) Conductor placement (b) Flux through the slot (c) Current displacement

Figure 2.8: Leakage flux through a stator slot, illustrating the influence of the current displacement in the conductors (c).

machines operating at electric frequencies up to 2 kHz. In certain applications, stranded wires are used. However, litz wires are generally suboptimal because they have a relatively low fill factor and poor thermal conductivity due to the substantial amount of insulation material required [105, 106]. In general, losses can be effectively predicted using finite element analysis (FEA), as demonstrated in [107].

Core Losses

The second major component of the total losses in HSPMSMs are the core losses. These are generally calculated using the Bertotti model. The core losses, denoted as P_{Fe}, are given by the following expression:

$$P_{\mathrm{Fe}} = k_{\mathrm{h}} f \left(\hat{B}\right)^2 + k_{\mathrm{c}} \left(f\hat{B}\right)^2 + k_{\mathrm{e}} \left(f\hat{B}\right)^{1.5}. \tag{2.2}$$

The core losses depend mainly on the electric frequency, f, and the amplitude of the flux density, $\hat{B}$. [108]. These losses are divided into three components: hysteresis losses, characterized by the pre-factor k_{h}, eddy current losses with the pre-factor k_{c}, and excess losses with the pre-factor k_{e}. These factors are assumed to be constant over the operating range and are specific for each core material. The electric frequency of a drive is determined by its speed and the number

of pole pairs. Typically, a pole pair number of one is picked for HSPMSM to minimize the frequency. As a result, it is advantageous for the machine to operate at lower rotational speeds in order to reduce these losses.
The eddy current losses can be expressed as follows:

$$P_{\mathrm{c}} = \frac{\pi^2 \sigma \hat{B}^2 d^2 f^2}{4}, \tag{2.3}$$

where σ denotes the electric conductivity of the lamination material and d represents its thickness. Two factors must be considered when selecting materials for HSPMSM: sheet thickness (d) and material conductivity. Reducing the thickness of the core material will reduce losses. Materials are available with thicknesses as low as 50 µm. Standard materials typically have a thickness of 0.35 mm. For high performance applications, thinner materials are more commonly used, particularly those in the non-oriented material class, with thicknesses ranging from 0.1 mm to 0.3 mm. Reducing the sheet thickness results in lower core stacking factors, which in turn increases the flux density in the core material. The second factor in reducing eddy current losses is to reduce the conductivity, σ.This is typically achieved by increasing the silicon content of the core material. While this results in a significant reduction in conductivity, it also affects the magnetic properties of the material. Soft magnetic steels typically contain about $3\,\%$ silicon, which increases the resistivity by a factor of four. JFE Steel, for example, is able to increase the silicon content to $6.5\,\%$, which further increases the resistivity. A non-oriented NO20 material has a resistivity of $52\,\mu\Omega\,\mathrm{cm}^{-1}$ [D6]. In contrast, a JFE material, 10JNFH600, with a silicon content of $6.5\,\%$ has a resistivity of $82\,\mu\Omega\,\mathrm{cm}^{-1}$ [D7].
The differences in the magnetization curves of these materials can be observed in Fig. 2.9, where measurements were made using the Epstein frame. The NO20 material has a significantly higher permeability at lower field strengths compared to the high-silicon material, which has a lower permeability. The resulting differences in losses are shown in Fig. 2.10, with measurements taken at 400 Hz and 2000 Hz for both materials. It can be observed that the NO20 material has higher losses in both cases, although the deviation is minimal at 400 Hz. The most significant difference in performance occurs at higher frequencies, such as 2000 Hz, where the losses at a polarization of 1.2 T are $176.5\,\mathrm{W\,kg}^{-1}$ for the NO20 material and $91.7\,\mathrm{W\,kg}^{-1}$ for the 10JNFH600 material. This comparison highlights the advantages and disadvantages that must be considered when selecting materials for HSPMSM.

Another material not included in this comparison is amorphous metal, which has been studied in [87]. This material has even lower losses than the materials discussed here and has a higher yield strength, making it suitable for rotor applications. A more detailed comparison between amorphous metals and high silicon steels can be found in [109].

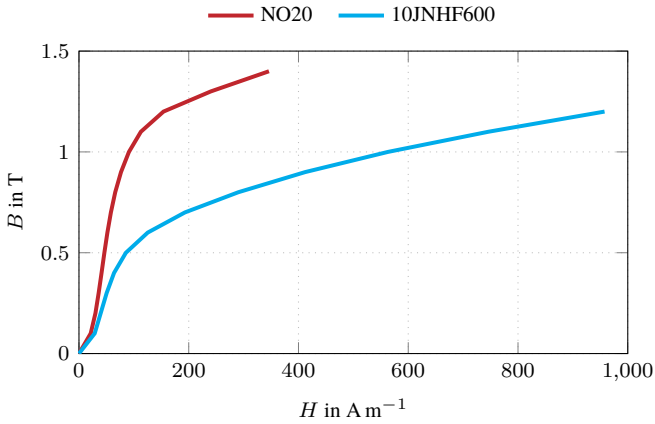

Figure 2.9: BH-curves of a NO20 silicon steel from Tata Steel compared with a 10JNHF600 from JFE, measured on an Epstein frame.

Windage Losses

Windage losses in electric machines refer to the power dissipation due to aerodynamic effects associated with rotating components. In particular, the rotor surface plays a significant role in these losses. Windage losses are primarily caused by the friction between the rotor and the surrounding air, as well as the high velocity in the narrow air gap between the rotor and the stator. These losses can significantly affect the efficiency and performance of electric machines and are therefore a critical consideration in the design and operation of such systems. Windage losses can be expressed by:

$$P_{\text{wind}} = kC_{\text{f}}\pi\rho_{\text{air}}\omega^3 {r_{\text{S}}}^4 l_{\text{Fe}} \tag{2.4}$$

In this equation, k is a roughness factor that assumes a value of 1 for an ideal smooth rotor and stator surface. The term C_{f} represents the coefficient of friction,

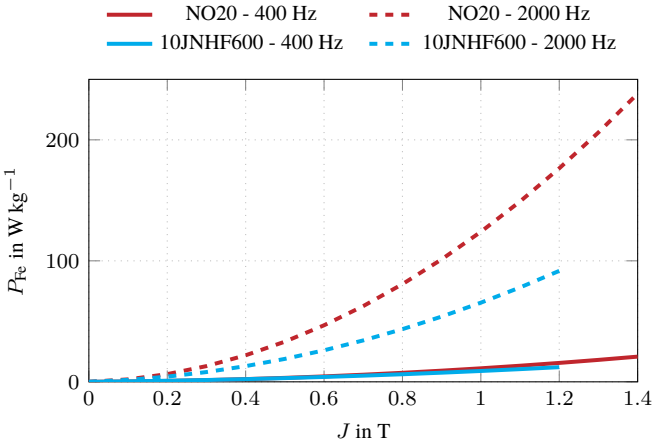

Figure 2.10: Power Loss of a NO20 silicon steel from Tata Steel compared with a 10JNHF600 from JFE at 400 Hz and 2000 Hz, measured in an Epstein frame.

which is further explained in Section 3.2.7.4. In addition, the speed ω, the sleeve or outer rotor radius r_S and the length of the axial air gap l_{Fe} are integral parts of the equation. Depending on the design of the shaft and the winding head, the length of the air gap can be longer than l_{Fe}. It is particularly noteworthy that the air gap losses have a cubic dependence on the circumferential speed, $v_c = \omega\, r_S$, and a linear dependence on the rotor area, $2\pi r_S \cdot l_{Fe}$.

Chapter 3

Multi-Physics Modeling of High-Speed Electric Machines

This chapter presents and explains in detail the modeling of a high-speed electric machine. The chapter is divided into three parts. First, the scaling of the turbomachinery is described in 3.1.1, and the strength of the rotor assembly and the bending eigenfrequencies are discussed in 3.1.2. Next, in 3.2, the magnetic properties of the synchronous motor are modeled according to a one-dimensional radial field. A new approach is presented to determine the air gap field for HSPMSM, which uses machine learning and static finite element analysis (FEA) results to train the models. Variations in air gap permeability due to slotting are accounted for by the air gap relative permeability function. The thermal design of the motor is verified with a 2D FEA simulation and details are described in 3.3. The chapter concludes with a description of the overall design process, which is the combination of the steps presented.

3.1 Aerodynamic Components and Mechanical Shaft Design

3.1.1 Scaling of Compressor and Turbine

As described in Section 1.2 a fuel cell requires pressurized air to increase the efficiency and power density of the system. According to [18, 110, 111] the centrifugal compressor is the most suitable compressor technology to fulfil the requirements of a PEM fuel cell. According to [111] the centrifugal compressor has its main advantages in the small size, low weight, the oil-free bearing system and the well fitting operating pressure. In addition, the centrifugal compressors require the smallest amount of space [18]. Furthermore, an electric compressor has the option to apply a radial turbine to recuperate energy which is left in the cathode exhaust air stream of the fuel cell. Depending on the aerodynamic operating point the turbine can provide up to $40\,\%$ of the compressor power [112]. These two aerodynamic components define the required torque and speed of the electric machine. Compared to an electric turbocharger, the recuperated power of the turbine will always be smaller compared to the input power of the compressor. This is because both components use the same air flow and the turbine inlet temperature is in a range of $70\,°\mathrm{C}$ to $85\,°\mathrm{C}$ and therefore contains less energy than the compressor outlet air flow [110]. The required machine will always be operated as a motor and never as a generator.

3.1.1.1 Centrifugal Compressor Design

A centrifugal compressor, also called a radial compressor, transfers energy from a spinning compressor wheel to a working gas. This causes the gas to accelerate and gain kinetic energy. Centrifugal compressors have the benefit of providing higher pressure ratios when dealing with lower flow rates compared to axial compressors. They are widely utilized in various industries such as oil and gas, power units, turbochargers, and gas turbines. As shown in Fig. 3.1, the compressor is build of five main parts: the inlet duct, the wheel, the diffuser, the volute, and the outlet duct. The inlet of the compressor is usually a straight pipe. The wheel is a rotating set of blades, which gradually transfers energy to the working gas. The gas enters the compressor in an axial direction, accelerates, and is discharged in a radial direction in the radial diffuser. The exit flow velocity of the gas from the wheel can reach transonic speeds. The radial diffuser plays a crucial role in converting the kinetic energy of the working gas into potential energy, especially pressure. It accomplishes this by increasing the cross-sectional area, which leads

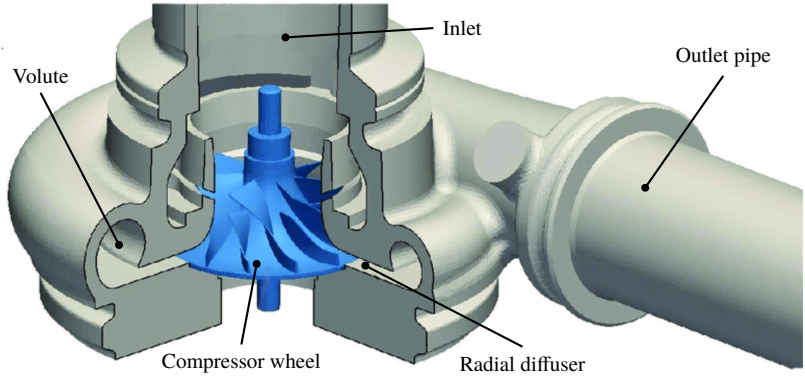

Figure 3.1: Components of a centrifugal compressor and its build up [113]

to a gradual reduction in flow velocity. There are two main types of diffusers: vaneless and vaned, each suitable for different application scenarios. The volute serves as a component that collects the flow from the diffuser and redirects it in a circumferential direction, ultimately delivering it to the compressor outlet pipe. As the flow enters the volute, its velocity is further reduced within the flow channel, resulting in an increase in static pressure. [113]
A compressor map provides a graphical representation of the performance characteristics of a compressor. For this study, the selected compressor served as a baseline due to its excellent performance in fuel cell applications, particularly in the power range of 90 kW to 130 kW. Its compressor map is shown in Fig. 3.2, in which the x-axis represents the volumetric flow rate $\dot{V}_{\text{corr}}$, while the y-axis shows the pressure ratio $\Pi_{\text{C,t-t}}$, defined as:

$$\Pi_{\text{C,t-t}} = \frac{p_{2,\text{tot}}}{p_{1,\text{tot}}}, \tag{3.1}$$

where $p_{2,\text{tot}}$ and $p_{1,\text{tot}}$ are the total pressures at the compressor outlet and inlet, respectively. Total pressure is a thermodynamic property that reflects the combined energy content of a moving gas and includes both static and dynamic pressure. The compressor map also shows critical operating limits. On the left side, the surge line marks the limit below which low flow rates and high pressure ratios cause flow instability, potentially leading to high thrust loads and system failure. On the right side of the map is the system characteristic, which indicates the up-

per flow capability of the compressor. At a corrected flow rate of $0.16\,\mathrm{m^3\,s^{-1}}$, the throttling limit is reached where the inlet flow reaches sonic speeds. Dashed lines within the map represent contours of constant corrected circumferential velocity measured at the compressor wheel outside diameter d_2. In addition, colored lines are included to indicate the constant isentropic efficiency. The isentropic efficiency of the compressor is defined as

$$\eta_{\mathrm{C,is}} = \frac{\Pi_{\mathrm{C,t\text{-}t}}^{\left(\frac{\kappa-1}{\kappa}\right)} - 1}{\frac{T_{\mathrm{tot,out}}}{T_{\mathrm{tot,in}}} - 1}, \tag{3.2}$$

where κ is the isentropic exponent of the working gas, and $T_{\mathrm{tot,in}}$ and $T_{\mathrm{tot,out}}$ are the total temperatures at the inlet and outlet of the compressor, respectively.

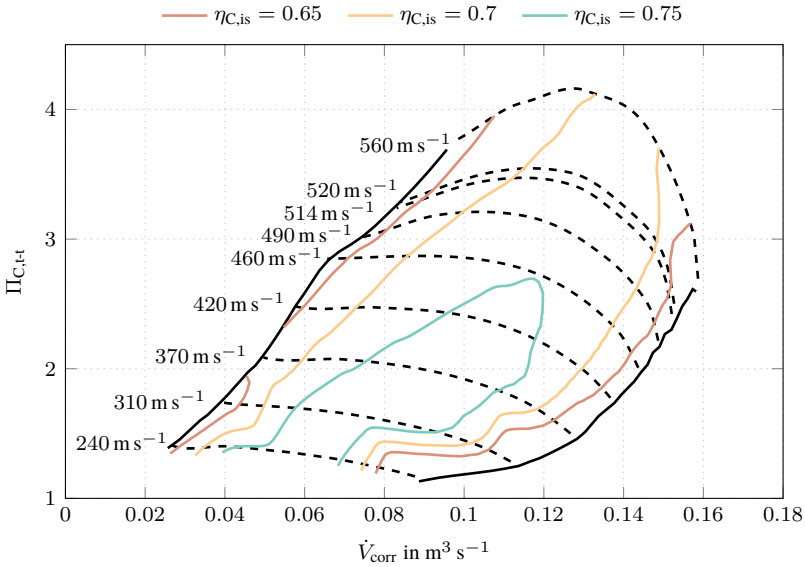

Figure 3.2: Compressor map showing the operating range of a centrifugal compressor. Lines of constant corrected speed and constant isentropic efficiency are shown. The compressor map is limited by the surge line on the left and by the system characteristics on the right. Maximum corrected peripheral speed $u_{\mathrm{c,corr}}$ defines the mechanical limit.

Compressor Map Scaling

Compressor scaling is a common practice in the design process of new compressors. A validated and robust design is typically used as a baseline to determine the performance characteristics and operating range of a new compressor. Several basic assumptions are taken from the existing literature. It is assumed that the trim, defined as the ratio of the inlet diameter to the outlet diameter, denoted by $\frac{d_1}{d_2}$, remains constant. Consequently, as the outer diameter increases, the inlet diameter also increases proportionally. The following scaling relations are used, taken from [26]:

$$\dot{V}_{\text{new}} = \dot{V}_{\text{old}} \left(\frac{d_{2,\text{new}}}{d_{2,\text{old}}} \right)^2 \tag{3.3}$$

$$\Pi_{\text{new}} = \Pi_{\text{old}} \tag{3.4}$$

Where $\dot{V}_{\text{new}}$ is the scaled volumetric flow rate, $\dot{V}_{\text{old}}$ is the base volumetric flow rate, and $d_{2,\text{new}}$ and $d_{2,\text{old}}$ are the new and old outer wheel diameters, respectively. It is further assumed that the characteristics of the diffuser and the volute remain identical. The pressure ratio of the compressor and the circumferential speed are described with eq. (1.1). It is seen that the pressure ratio $\Pi_{\text{C,t-t}}$ is a function of $f({u_{\text{c,corr}}}^2)$. Regarding efficiency, which is crucial to determine the required input power, this study uses the approach proposed in [114, 115]. These authors analyzed compressors with similar characteristics but different sizes, using different data sets to correlate the external wheel diameter d_2 with the maximum isentropic efficiency $\eta_{\text{CW,max}}$. The proposed scaling relationship has the form

$$\Delta\eta_{\text{CW,new}} = c \cdot \ln \left(\frac{d_{2,\text{new}}}{d_{2,\text{old}}} \right) \tag{3.5}$$

$$\eta_{\text{CW,new}} = \Delta\eta_{\text{CW,new}} + \eta_{\text{CW,old}} \tag{3.6}$$

where the factor c ranges from 0.032 to 0.036. The variation of c for different wheels is illustrated in Fig. 3.3, showing only a small influence between cases. Since no specific database is available for the reference compressor wheel in this study, a value of $c = 0.034$ is chosen, as shown in eq. (3.6).
In general, larger outside diameters result in reduced relative gap losses within the compressor, leading to an overall increase in efficiency [116].
The above correlations for compressor wheels of different sizes allow the determination of the maximum efficiency under the new boundary conditions of $\dot{V}_{\text{corr}}$ and $\Pi_{\text{C,t-t}}$, based on the specified wheel. Consequently, the output will include

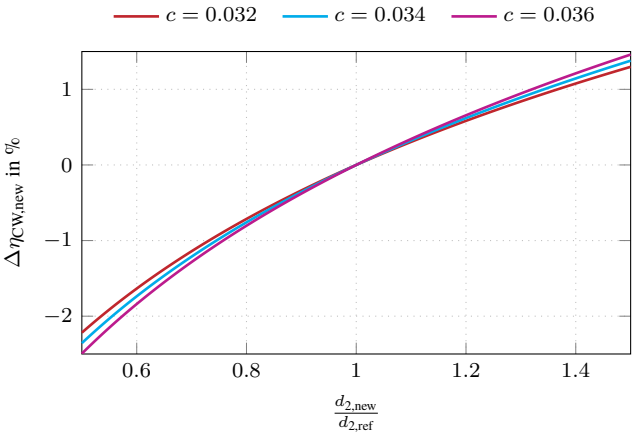

Figure 3.3: Comparison of the different scaling approaches suggested by [114, 115].

$d_{2,\text{new}}$. To calculate the compressor power P_C, the required shaft power is given by:

$$P_\text{C} = \rho_1 \dot{V}_\text{corr} c_\text{p} T_1 \left(\Pi_{\text{C,t-t}}{}^{\left(\frac{\kappa-1}{\kappa}\right)} - 1 \right) \eta_{\text{CW,new}}{}^{-1} \tag{3.7}$$

Here the mass flow of air is represented by $\rho_1 \dot{V}_\text{corr}$, and T_1 is the compressor inlet temperature. Together, these factors provide a comprehensive framework for determining the performance characteristics of the compressor.

3.1.1.2 Turbine Dimensioning

The goal of the turbine sizing approach is to obtain the turbine wheel dimensions and a good estimate of the turbine efficiency, since this defines the nominal operating point of the electrical machine. It is well known in turbocharger design that radial turbines have their optimum efficiency at a blade speed ratio $\frac{u_4}{c_0}$ of about 0.7. This ratio can be derived for ideal conditions and is given in [117]. The blade speed ratio is determined by the circumferential speed of the turbine wheel u_4. This speed ratio is influenced by factors such as the speed of the electric machine, the turbine wheel diameter and the isentropic outflow velocity c_0. The latter represents the speed obtained when the total to static enthalpy $\Delta h_{\text{T,t-st,is}}$ is

completely converted into kinetic energy by an isentropic process. This velocity can be expressed by:

$$\frac{{c_0}^2}{2} = \Delta h_{\text{T,t-st,is}} \tag{3.8}$$

The enthalpy difference can be calculated by:

$$\Delta h_{\text{T,t-st,is}} = c_{\text{p}}\, T_4 \left(1 - \frac{1}{\Pi_{\text{TW}}}\right)^{\left(\frac{\kappa-1}{\kappa}\right)}. \tag{3.9}$$

In here the turbine inlet temperature is denoted with T_4 and the turbine pressure ratio with Π_{TW}, which is defined as the ratio of inlet pressure $p_{\text{4,tot}}$ to outlet pressure $p_{\text{3,tot}}$:

$$\Pi_{\text{TW}} = \frac{p_{\text{4,st}}}{p_{\text{3,tot}}} \tag{3.10}$$

For this work the blade speed ratio is assumed to be in the theoretical maximum of

$$\frac{u_4}{c_0} = \sqrt{\frac{1}{2}}, \tag{3.11}$$

although in reality the maximum efficiency is reached at a lower ratio [117]. With $\Delta h_{\text{T,t-st,is}}$ the isentropic spouting velocity and the circumferential speed of the wheel can be determined for a given speed n, which also determines the outer diameter of the wheel. The pressure ratio across the turbine is derived from the operating point of the compressor and a pressure drop across the fuel cell divided by the atmospheric pressure. To scale the turbine diameter with the wheel size, the maximum efficiencies of different turbines were used. The following relation was derived:

$$\eta_{\text{T,is}} = 0.102 \cdot \ln\left(d_4\right) + 0.283 \tag{3.12}$$

Therefore, the outer dimension of the turbine wheel and the efficiency are determined. The turbine power P_{T} is calculated:

$$P_{\text{T}} = m_{\text{T}} \Delta h_{\text{T,t-st,is}} \eta_{\text{T,is}}. \tag{3.13}$$

Here m_{T} describes the turbine mass flow. With both power and speed, all other parameters such as shaft torque can be determined.

3.1.1.3 Wheel Dimensions

For the later analysis of the natural frequency of the shaft, the mass, and volume of the compressor and turbine wheel must be known. It is assumed that these dimensions are scaled with the same ratio as the outside diameters. The scaling of the compressor wheel length is therefore determined by

$$l_{\mathrm{CW,new}} = \frac{d_{2,\mathrm{new}}}{d_{2,\mathrm{old}}}\, l_{\mathrm{CW,old}} \tag{3.14}$$

Where the old compressor wheel length is denoted by $l_{\mathrm{CW,old}}$.

3.1.2 Shaft Design with a Cylindrical Magnet

This section presents an analytical description of the deformation and stress behavior of the two primary components of the electric machine rotor. Ensuring the mechanical integrity of the rotor assembly is critical for safe operation. The focus is on the rotor design with a cylindrical magnet and a protective sleeve, as shown in Fig. 3.4. At the center of the shaft is a cylindrical magnet made of Sm_2Co_{17} because of its high energy density at elevated temperatures. The magnet is contained within a sleeve made of either Inconel 718 or TiAl6V4, materials known for their high specific strength and electrical resistivity. Fiber-reinforced plastics were excluded to ensure manufacturability. The strength and stability of these components are at the core of the rotor design. In addition, natural frequency calculations, including estimation of airfoil bearing dimensions, are presented.
The sleeve design is a critical aspect of the rotor assembly. Due to the low tensile strength of the magnet material, the sleeve provides structural support to prevent rotor failure due to centrifugal forces at high angular speeds. The magnet, which can withstand compression up to $800\,\mathrm{MPa}$, is highly susceptible to tensile failure at only $40\,\mathrm{MPa}$. To mitigate this, the sleeve is designed with an interference fit that creates a compressive bias on the magnet. This compressive stress counteracts the centrifugal forces and ensures safe operation. Thermal effects are also considered, as the differential thermal expansion between the sleeve and the magnet changes the joint pressure. These aspects are analyzed in the following sections.

3.1.2.1 Load Cases

Stability is ensured by analyzing six load cases, outlined in Table 3.1. Load cases 1 and 2 are based on standstill interference, and cases 3 and 4 are based on

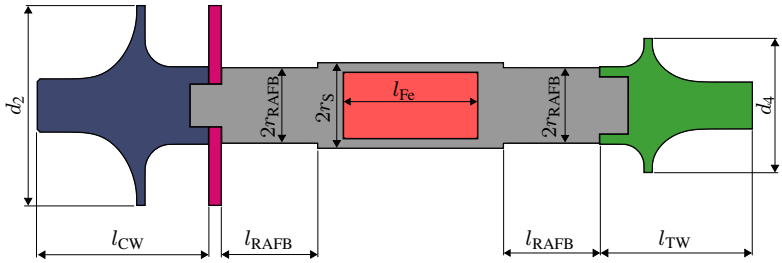

Figure 3.4: Schematic of the rotor configuration, showing the compressor wheel (blue), turbine wheel (green), and cylindrical magnet (red) contained in a sleeve. The shaft (gray) includes the sleeve and radial bearing seats, while the thrust bearing disc is colored magenta.

operation at maximum speed. For these cases, a safety factor of 1.2 is applied. Load cases (5, 6) simulate overspeed conditions where the sleeve is required to prevent catastrophic rotor failure, with a reduced safety factor of 1.0. In all scenarios, the joint pressure must remain above 0 MPa to prevent uncontrolled magnet movement.

Table 3.1: Load cases and design criteria for sleeve design

Case No.	Speed min^{-1}	Temperature °C	SF -	σ_{J} MPa
1	0	20	1.2	> 0
2	0	$T_{\mathrm{R,max}}$	1.2	
3	n_{max}	20	1.2	
4	n_{max}	$T_{\mathrm{R,max}}$	1.2	
5	$1.2 \cdot n_{\mathrm{max}}$	20	1.0	
6	$1.2 \cdot n_{\mathrm{max}}$	$T_{\mathrm{R,max}}$	1.0	

3.1.2.2 Approach

The effects influencing the load on the magnet and sleeve are analyzed below.

Thermal Elongation

Thermal elongation, the tendency of materials to expand with temperature, is described by eq. (3.15). A linear and isentropic behavior is assumed, and the thermal elongation is described by:

$$\varepsilon_{\mathrm{T}} = l_0 \cdot \alpha \cdot (T_2 - T_1), \tag{3.15}$$

where l_0 is the reference length at room temperature, α is the coefficient of thermal expansion, T_1 is the reference temperature, and T_2 is the operating temperature.

Rotational Elongation

The rotational strain is assumed to have linear material behavior and no plastic deformation. Since the design goal is to keep all stresses below the yield strength, this assumption is valid for the materials considered. For the rotor design considered, two geometries must be considered. The magnet can be described as a solid rotating disc. Furthermore, the sleeve can be described as a rotating ring. The application is considered as a plane axisymmetric problem:

$$\varepsilon_{\mathrm{rr}} = \frac{\partial u_{\mathrm{r}}}{\partial r}, \quad \varepsilon_{\theta\theta} = \frac{u_{\mathrm{r}}}{r}, \quad \varepsilon_{r\theta} = 0 \tag{3.16}$$

where u_{r} describes the displacement of a material point in radial direction, $\varepsilon_{\mathrm{rr}}$, $\varepsilon_{\theta\theta}$ are the radial and tangential strains. The shear strain $\varepsilon_{r\theta}$ can be neglected in the plane problem. The axial directions are shown in Fig. 3.5, where the stresses are marked with σ. The indices correspond to the strains ε. To model the disc, a thin rotating disc with constant angular velocity ω is considered. The acceleration acting on an element is $-\omega^2\, r$. This results in an internal acceleration per unit volume of $F_{\mathrm{a}} = -\rho\, r\, \omega^2$. This force causes stresses in the disc. The equation of motion for a plane axisymmetric problem is:

$$\frac{\partial \sigma_{\mathrm{rr}}}{\partial r} + \frac{1}{r}\left(\sigma_{\mathrm{rr}} - \sigma_{\theta\theta}\right) + \rho r \omega^2 = 0 \tag{3.17}$$

With Hooke's law that problem can be described as a static problem:

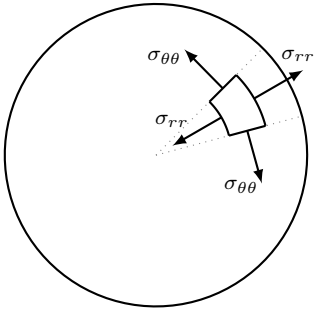

Figure 3.5: Stress components in a plane axisymmetric problem

$$\sigma_{\mathrm{rr}} = \frac{E}{1-\nu^2}\left(\varepsilon_{\mathrm{rr}} + \nu\varepsilon_{\theta\theta}\right) \tag{3.18}$$

$$\sigma_{\theta\theta} = \frac{E}{1-\nu^2}\left(\varepsilon_{\theta\theta} + \nu\varepsilon_{\mathrm{rr}}\right), \tag{3.19}$$

where E is Young's modulus and ν is Poisson's ratio. The differential equation is derived from eq. (3.17) with the formulation of Eqs. (3.18) and (3.19) and is given by:

$$\frac{d^2u_{\mathrm{r}}}{dr^2} + \frac{1}{r}\frac{du_{\mathrm{r}}}{dr} - \frac{1}{r^2}u = -\frac{1-\nu^2}{E}\rho r\omega^2 \tag{3.20}$$

The general solution for the strain and stresses of eq. (3.20) is given by:

$$\sigma_{\mathrm{rr}} = A\frac{1}{r^2} + 2C - \frac{1}{8}(3+\nu)\rho\omega^2 r^2, \tag{3.21}$$

$$\sigma_{\theta\theta} = -A\frac{1}{r^2} + 2C - \frac{1}{8}(1+3\nu)\rho\omega^2 r^2, \tag{3.22}$$

$$\varepsilon_{\mathrm{rr}} = \frac{1}{E}\left[(1+\nu)\frac{A}{r^2} + 2(1-\nu)C - \frac{3}{8}\left(1-\nu^2\right)\rho\omega^2 r^2\right], \tag{3.23}$$

$$\varepsilon_{\theta\theta} = \frac{1}{E}\left[-(1+\nu)\frac{A}{r^2} + 2(1-\nu)C - \frac{1}{8}\left(1-\nu^2\right)\rho\omega^2 r^2\right], \tag{3.24}$$

$$u_{\mathrm{r}} = \frac{1}{E}\left[-(1+\nu)\frac{A}{r^2} + 2(1-\nu)Cr - \frac{1}{8}\left(1-v^2\right)\rho\omega^2 r^3\right]. \tag{3.25}$$

The boundary condition of zero radial stresses at the outer diameter r_o of the disc:

$$\sigma_\mathrm{rr}(r = r_\mathrm{o}) = 0 \tag{3.26}$$

To ensure finite stresses and strains at $r = 0$ for a solid disc the solution for A and C becomes:

$$A = 0, \quad C = \frac{1}{16}(3+\nu)\rho\omega^2 {r_\mathrm{o}}^2 \tag{3.27}$$

Further, the stresses and displacements for a solid disc are

$$\sigma_\mathrm{rr}(r) = \frac{3+\nu}{8}\rho\omega^2 \left[{r_\mathrm{o}}^2 - r^2\right], \tag{3.28}$$

$$\sigma_{\theta\theta}(r) = \frac{3+\nu}{8}\rho\omega^2 \left[{r_\mathrm{o}}^2 - \frac{1+3\nu}{3+\nu} r^2\right], \tag{3.29}$$

$$u_\mathrm{r}(r) = \frac{3+\nu}{8}\rho\omega^2 \frac{1-\nu}{E} r \left[{r_\mathrm{o}}^2 - \frac{1+\nu}{3+\nu} r^2\right]. \tag{3.30}$$

For a hollow disc the same general solution is applied, but the boundary conditions change as,

$$\sigma_\mathrm{rr}(r_i) = 0, \quad \sigma_\mathrm{rr}(r_\mathrm{o}) = 0, \tag{3.31}$$

where r_i is the inner radius of the hollow disc. Therefore, the terms A and C from the general solution in Eqs. (3.21) to (3.25) leads to:

$$A = -\frac{1}{8}(3+\nu)\rho\omega^2 {r_\mathrm{i}}^2 {r_\mathrm{o}}^2, \quad C = \frac{1}{16}(3+\nu)\rho\omega^2 \left({r_\mathrm{i}}^2 + {r_\mathrm{o}}^2\right) \tag{3.32}$$

From that the stresses and displacements follow for the hollow disc as

$$\sigma_\mathrm{rr}(r) = \frac{3+\nu}{8}\rho\omega^2 \left[r_i^2 + {r_\mathrm{o}}^2 - r^2 - \frac{{r_\mathrm{i}}^2 {r_\mathrm{o}}^2}{r^2}\right], \tag{3.33}$$

$$\sigma_{\theta\theta}(r) = \frac{3+\nu}{8}\rho\omega^2 \left[r_i^2 + {r_\mathrm{o}}^2 - \frac{1+3\nu}{3+\nu} r^2 + \frac{{r_\mathrm{i}}^2 {r_\mathrm{o}}^2}{r^2}\right], \tag{3.34}$$

$$u_\mathrm{r}(r) = \frac{3+\nu}{8}\rho\omega^2 \frac{1-\nu}{E} r \left[r_i^2 + {r_\mathrm{o}}^2 - \frac{1+\nu}{3+\nu} r^2 + \frac{1+\nu}{1-\nu}\frac{{r_\mathrm{i}}^2 {r_\mathrm{o}}^2}{r^2}\right]. \tag{3.35}$$

With this set of equations, the stresses and strains for both rotor components can be calculated. The two parts are therefore considered separately. The solution for the two parts is shown in Figs. 3.6 (a) and 3.6 (b). To understand which positions of the two parts need to be calculated and analyzed, it is important to look at

the results for the single part. In Fig. 3.6 (a) the solid disc is shown. The stress maximum occurs in the center of the disc. Both radial and tangential stresses have their maximum in the center. The radial stresses become zero at the outer radius because it was already defined in the boundary conditions. The tangential stresses will not be zero, but will also decrease outward. The maximum strain will occur at the outer radius. For the hollow disc in Fig. 3.6 (b), the stresses and strains are different from the inner radius to the outer radius. The maximum stresses are the tangential stresses at the inner radius, which then decrease toward the outer radius. The radial stresses are zero at the inner and outer radius, but reach a maximum in between depending on the given geometry. Strain is more constant along the radius, but also reaches a maximum near the outer radius. It can be concluded that for the investigated case the radial and tangential stresses of the solid disk reach their maximum at $r = 0\,\mathrm{mm}$ and for the hollow disk the tangential stresses reach their maximum at $r = r_\mathrm{i}$. In the later results, the stresses are calculated at these two locations.

Cylindrical Interference Fit

In general, interference fits are divided into elastic, elastic-plastic, and fully plastic fits [118]. For the following design, only the elastic interference fit is considered. Due to the high rotational speeds, the influence of the fit must be taken into account in order to calculate the actual joint pressure in all operating conditions. The interference fit between the magnet and the sleeve is calculated using [118]. To determine the contact pressure for $n = 0$, the support variable K is defined as:

$$K = \frac{E_\mathrm{O}}{E_\mathrm{I}} \left(\frac{1 + {Q_\mathrm{I}}^2}{1 - {Q_\mathrm{I}}^2} - \nu_\mathrm{I} \right) + \frac{1 + {Q_\mathrm{O}}^2}{1 - {Q_\mathrm{O}}^2} + \nu_\mathrm{O}. \tag{3.36}$$

For a solid inner part K simplifies to

$$K = \frac{E_\mathrm{O}}{E_\mathrm{I}} \left(1 - \nu_\mathrm{I}\right) + \frac{1 + {Q_\mathrm{O}}^2}{1 - {Q_\mathrm{O}}^2} + \nu_\mathrm{O}, \tag{3.37}$$

where $E_\mathrm{O}, E_\mathrm{I}$ describe the young's modulus of the outer and inner part, $\nu_\mathrm{O}, \nu_\mathrm{I}$ are the Poisson's ratio of the outer and inner part. Further,

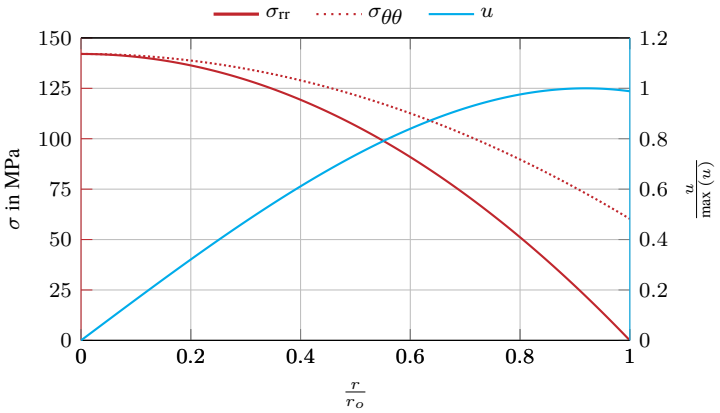

(a) Solid rotating disc

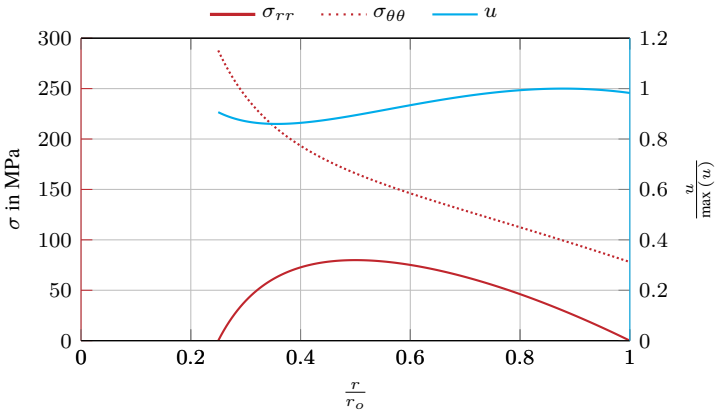

(b) Hollow rotating disc

Figure 3.6: Nominal stresses of a solid rotating disc (a) and a hollow rotating disc (b)

$$Q_{\mathrm{O}} = \frac{d_{\mathrm{Oi}}}{d_{\mathrm{Oo}}} \tag{3.38}$$

$$Q_{\mathrm{I}} = \frac{d_{\mathrm{Ii}}}{d_{\mathrm{Ii}}} \tag{3.39}$$

are defined where d_{Oi} and d_{Ii} equals the joint diameter d_{J}, d_{Oo} the outer diameter of the sleeve and d_{Ii} the inner diameter of the magnet. If the magnet is a solid disc given by $d_{\mathrm{Ii}} = 0$, Q_{I} becomes 0. The joint pressure p is

$$p_{\mathrm{J,o}}(\omega = 0) = \frac{\xi_{\mathrm{w}} E_{\mathrm{O}}}{K}, \text{with} \tag{3.40}$$

$$\xi_{\mathrm{w}} = \frac{U_{\mathrm{W}}}{d_{\mathrm{J}}} \tag{3.41}$$

in which ξ_{w} is the related effective overlap of the joint and U_{W} the geometrical effective overlap of the two parts.

Rotating Interference Fit

High rotational speeds and high circumferential speeds result in higher stresses and loads due to centrifugal force. The outer part of the interference fit usually expands more than the inner part of the joint due to the higher centrifugal force. The joint pressure decreases and the load that can be transferred between the two parts decreases. Therefore, this load case must be considered. The effective overlap ξ_{w} as the rotor spins is given in [119],

$$\xi_{\mathrm{w}} = \frac{1}{E_{\mathrm{O}}} \left(\left[\frac{E_{\mathrm{O}}}{E_{\mathrm{I}}} \left(\frac{1 + {Q_{\mathrm{I}}}^2}{1 - {Q_{\mathrm{I}}}^2} - \nu_{\mathrm{I}} \right) + \frac{1 + {Q_{\mathrm{O}}}^2}{1 - {Q_{\mathrm{O}}}^2} + \nu_{\mathrm{O}} \right] p_{\mathrm{J,n}} + \frac{K {d_{\mathrm{J}}}^2 \rho_{\mathrm{O}} \omega^2}{16 {Q_{\mathrm{O}}}^2} \right) \tag{3.42}$$

in which K is defined by:

$$K = 3 + \nu_{\mathrm{O}} + (1 - \nu_{\mathrm{O}}) \, {Q_{\mathrm{O}}}^2 - \frac{E_{\mathrm{O}} \rho_{\mathrm{I}}}{E_{\mathrm{I}} \rho_{\mathrm{O}}} {Q_{\mathrm{O}}}^2 \left[1 - \nu_{\mathrm{I}} + (3 + \nu_{\mathrm{I}}) \, {Q_{\mathrm{I}}}^2 \right]. \tag{3.43}$$

To determine the joint pressure $p_{\mathrm{J,n}}$ the lift of speed ω_{lift} needs to be known which is described by:

$$\omega_{\mathrm{lift}} = \frac{4 Q_{\mathrm{O}}}{d_{\mathrm{J}}} \sqrt{\frac{E_{\mathrm{O}} \xi_{\mathrm{w}}}{K \rho_{\mathrm{O}}}} \tag{3.44}$$

Further, the joint pressure $p_{\mathrm{J,n}}$ is defined as

$$p_{\mathrm{J,n}} = \left[1 - \left(\frac{\omega}{\omega_{\mathrm{lift}}}\right)^2\right] p_{\mathrm{J,o}}. \tag{3.45}$$

The joint pressure introduces stresses in the two components. As the magnet is a full disc, the two stress components σ_{rr} and $\sigma_{\theta\theta}$ are

$$\sigma_{\mathrm{rr}} = \sigma_{\theta\theta} = -p_{\mathrm{J,n}} \tag{3.46}$$

and therefore independent of the radius. For the sleeve the stresses are defined as:

$$\sigma_{\mathrm{rr}} = -\frac{{Q_{\mathrm{O}}}^2}{1 - {Q_{\mathrm{O}}}^2}\left[\left(\frac{d_{\mathrm{Oo}}}{2r}\right)^2 - 1\right] p_{\mathrm{J,n}}, \tag{3.47}$$

$$\sigma_{\theta\theta} = -\frac{{Q_{\mathrm{O}}}^2}{1 - {Q_{\mathrm{O}}}^2}\left[\left(\frac{d_{\mathrm{Oo}}}{2r}\right)^2 + 1\right] p_{\mathrm{J,n}} \tag{3.48}$$

For the sleeve $\sigma_{\mathrm{rr}}(d_{\mathrm{Oo}}) = 0\,\mathrm{MPa}$ and $\sigma_{\mathrm{rr}}(d_{\mathrm{J}}) = -p_{\mathrm{J,n}}$. To determine the equivalent stress for plane stresses, the von Mises stresses are calculated by:

$$\sigma_{\mathrm{eq}} = \sqrt{{\sigma_{\mathrm{rr}}}^2 + {\sigma_{\theta\theta}}^2 - \sigma_{\mathrm{rr}} \cdot \sigma_{\theta\theta}} \tag{3.49}$$

In Fig. 3.7 the results are shown for an exemplary geometry with a solid inner shaft with $d_{\mathrm{J}} = 40\,\mathrm{mm}$ and a hub with $d_{\mathrm{Oo}} = 70\,\mathrm{mm}$ and $p_{\mathrm{J,o}} = 10\,\mathrm{MPa}$. It shows that the stresses in the shaft are constant for radial and tangential stresses and have a negative sign, indicating a compression of the shaft. The equivalent stress is also indicated by $p_{\mathrm{J,o}}$. The stresses in the hub reach their maximum at d_{Ii} and decrease until they reach $p_{\mathrm{J,o}}$ at $r = \frac{d_{\mathrm{Oo}}}{2}$. This completes the determination of the different load cases a shaft of a HSPMSM is exposed to during operation. The next step is to combine all the loads.

3.1.2.3 Superposition of Shaft Loads

As mentioned above, a linear elastic material behavior is assumed and therefore a superposition of loads can be considered. The calculation is completed for all six defined load cases described in Table 3.1. It is important to determine the stresses for the minimum and maximum overlap of the two parts, since the max-

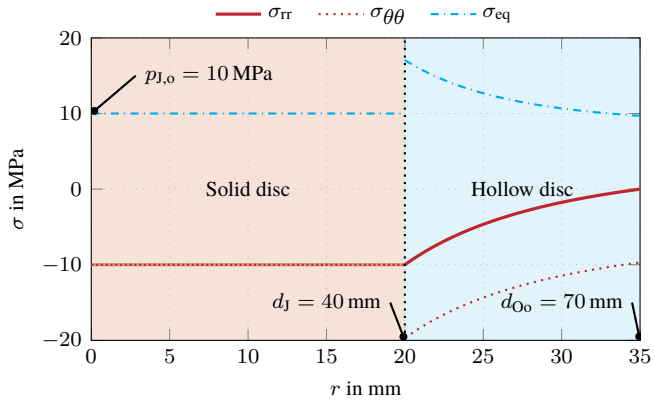

Figure 3.7: Radial, tangential and von Mieses stresses for an exemplary geometry with a contact pressure of 10 MPa at 0 min^{-1}

imum overlap is critical for the sleeve and the minimum overlap is the critical overlap for the magnet. In addition, the minimum and maximum operating temperatures must be considered. Depending on the thermal expansion factor, the main overlap will increase or decrease as the temperature increases. For example, Inconel 718 has a higher coefficient of thermal expansion than Sm_2Co_{17}, so the overlap decreases with increasing temperature. Titanium, on the other hand, has a smaller coefficient of thermal expansion than Sm_2Co_{17}, so the overlap increases with increasing temperature.

3.1.2.4 Failure Hypothesis for Magnets

For magnetic materials such as NdFeB and Sm_2Co_{17}, the equivalent stress hypothesis is not valid because of their imbalance in compressive and tensile strength. Therefore, the modified Mohr-Coulomb theory is used [120]. Since the problem is two-dimensional, the maximum allowable stresses are shown in Fig. 3.8. The radial stresses σ_{rr} are plotted on the x-axis and the tangential stresses $\sigma_{\theta\theta}$ are plotted on the y-axis. The colored area in the plot shows the safe operating range for the material. It can be seen that the absolute values of the maximum allowable tensile stress σ_t and the compressive strength σ_c are very different. In Table 2.5 the properties for the two studied magnetic materials are shown. For Sm_2Co_{17} the compressive strength σ_c is about 20 times higher than

for σ_t. Therefore, the maximum principal stress in the tensile direction that can be tolerated for the magnet is the yield stress.

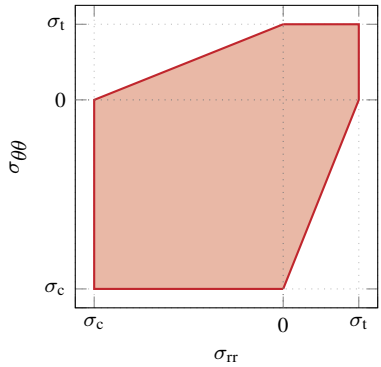

Figure 3.8: Mohr-Coulomb failure envelope for a plane stress condition, showing the safe stress region (shaded in red) defined by the tensile strength (σ_t) and compressive strength (σ_c) in the σ_{rr}-$\sigma_{\theta\theta}$ plane.

3.1.3 Aerodynamic Gas Bearings

In the application of a hydrogen fuel cell electric compressor, there is a requirement to be oil-free due to the cleanliness requirements of the fuel cell. Therefore, gas bearings are used. Gas bearings can be divided into two functional groups. First, the self-acting (hydrodynamic) type and second, the externally pressurized (hydrostatic and hybrid) types. In a self-acting bearing, the load capacity is generated by the relative motion between the rotor and the stationary part of the bearing. The viscous shear in the fluid film draws the lubricant into an aerodynamic wedge, creating a pressure gradient. Only the pressure gradient is responsible for the load carrying capacity, rigidity, and damping of the bearing. As a general effect, increasing the rotor speed increases the load capacity [121, 122]. In the market of electric compressors, the hydrodynamic type is used. Two different designs are used. On the one hand, herringbone grooved journal and thrust bearings, which belong to the subcategory of rigid gas bearings. On the other hand the foil bearings as shown in Fig. 3.9, which belong to the compliant bearings [121]. Foil bearings have the advantage of high load capacity, tolerance to misalignment, manufacturing error and thermal gradients. These are the main

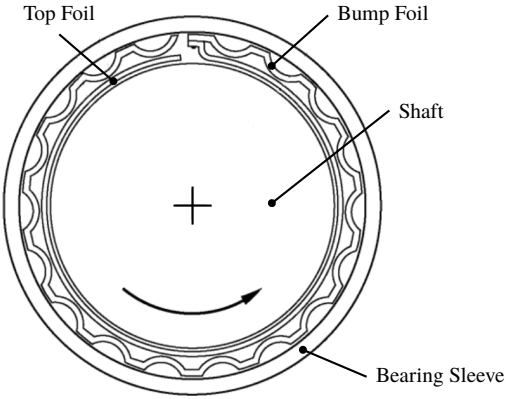

Figure 3.9: Components and build up of an air foil bearing [123].

disadvantages of herringbone bearings. As seen in Fig. 3.9, the bearing consists of a stationary sleeve, a bump foil, a top foil and the rotating shaft.
Bearing design is not a major topic of this thesis. Since the bearing design affects the natural frequency of the shaft, it is necessary to dimension the bearings with the focus on the bearing diameter and length. Therefore, the bearing design of the developed electric compressor is used as a baseline design. The circumferential speed of the bearings is kept at $200\,\mathrm{m\,s^{-1}}$. The ratio of width to diameter is kept at 1.25. For rotor designs with a sleeve circumferential speed above $200\,\mathrm{m\,s^{-1}}$, the diameter of the bearings is reduced by $1.5\,\mathrm{mm}$. The thrust bearing, which carries the axial load of the system, is scaled only in the outer diameter and has the same diameter as the outer diameter of the compressor wheel.

3.1.4 Modal Analysis of the Rotor

The modal analysis is done with a FEA simulation in ANSYS Mechanical. For this purpose, a simplified and fully parametrized 3D model is set up, which can be scaled according to the previously derived dimensions, shown in Fig. 3.4. The objective of the study is to find the maximum allowable active length of the machine. Therefore, the first bending eigenfrequency must be determined. The first bending eigenfrequency should be 1.2 times higher than the maximum operating speed, which is a common value for electric machine designs. To find the maximum active length efficiently, the natural frequency is calculated for four

different active lengths of the rotor. From these four solutions, the maximum active length is interpolated and used as the maximum allowed active length. The maximum speed is already defined by the maximum compressor operating point and therefore the compressor and turbine wheel dimensions are defined.

3.2 Magnetic Domain

This section describes the modeling of the magnetic domain. The focus is on the modeling of the rotor field.

3.2.1 Assumptions and Simplifications

Analytical calculations of electric machines are described in many publications such as [52, 53]. They are usually done with the following assumptions.

- Due to the relatively small air gap widths in relation to the bore radius, the round machine geometry can be converted into a plane machine geometry.
- The machine geometry is further simplified into a geometry with a smooth air gap on both sides.
- Air gap flux density in radial direction is assumed to be constant.
- The windings of the stator are integrated directly into the air gap. For this purpose, equivalent current filaments are denoted at the centers of the respective slots.
- The iron of the machine is assumed to be magnetically infinitely conductive $\mu_{\mathrm{Fe}} \rightarrow \infty$
- The resulting air gap field has only a radial component. The tangential field is neglected.
- A perfect mechanical symmetry is assumed (neglect of eccentricities and other irregularities in the mechanical structure).

These assumptions need to be checked and made sure that they fit the applications under consideration, since these are geometry related. In this work, the focus is on the first three assumptions.

Plane machine geometry The rotationally symmetrical rotor can be unwound into a plane machine geometry if the air gap length is negligible compared to the stator bore radius and the rotor radius. For HSPMSM with high circumferential speeds and high rotational speeds, the magnet requires a sleeve to protect it. As seen in a later chapter for the reference machine, the ratio of $\frac{\delta}{r_{\mathrm{M}}}$ is about 0.5 and about 0.33 for $\frac{\delta}{r_{\mathrm{B}}}$. This already shows that a plane machine geometry cannot be assumed.

Smooth Air Gap on Both Sides

The rotor surface is smooth in the design under consideration. The stator is slotted and therefore can not be assumed to be smooth. In particular, the induced flux harmonics must be taken into account when calculating the rotor eddy current losses. The influence of slotting is considered with relative permeance functions. Therefore, a new approach is derived which has already been published in the authors' work [E8].

Constant Radial Air Gap Flux Density

The air gap flux density cannot be assumed to be constant at a given angular position in the radial direction. Even a linear scaling over the length of the air gap is not suitable due to leakage flux which closes itself in the air gap, as shown in Section 3.2.2.

3.2.2 Air Gap Flux

The most important part of the magnetic domain modeling is the determination of the radial air gap flux density of the machine. It is the basis for calculating the machine power and losses. The modeling is divided into two parts. The stator field excitation curve which is taken directly from textbooks like [52, 53, 124] and the modeling of the rotor field. The modeling of the rotor field is adapted to the application limits, which do not correspond to the assumptions of the textbooks.

3.2.2.1 Field Excitation Curve

The analytic equations of the field excitation curve of a stator winding are calculated on the basis of a distributed, two-layer winding consisting of m strings, which is spatially symmetrical with

$$\alpha_{\mathrm{m,mech}} = \frac{2\pi}{mp}. \tag{3.50}$$

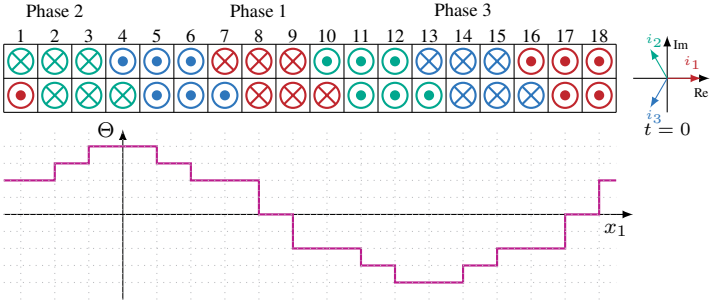

Figure 3.10: Stator field excitation curve at $t = 0$ with exemplary configuration shown for $q = 3$ and $y = 1$.

Here m denotes the number of phases and p the number of pole pairs. For the special case of a single-layer winding, the pole pitch τ_p is equal to the coil span y, and the number of turns per coil w_c of a two-layer winding is half that of a single-layer winding. It is possible to specify any current form $i(t)$. To distinguish between field cause and field effect, the former are indexed by k and the latter by k'. Fig. 3.10 shows the slot layout of a two-layer stator winding and the associated magnetic excitation curve when sinusoidal and filamentary currents are specified at the time $t = 0$. The staircase-shaped magnetic excitation curve can be calculated with the aid of a complex Fourier series, taking into account all harmonics, with

$$\underline{\Theta}_1\left(x_1, t\right) = \sum_{k'=1}^{m} \frac{w}{\pi} i(t) \sum_{s} \frac{{}^{s}k_{\mathrm{w},k_1}}{s} \exp j\left[s\left(k'-1\right)\frac{2\pi}{mp} - s x_1\right], \tag{3.51}$$

as described in [125]. In here s is the harmonic order. Further, the series winding number is defined as:

$$w = 2pqw_\mathrm{c} \tag{3.52}$$

for a two-layer winding, where w_c is the number of turns of the coil and q is the number of slots per pole and per phase. The winding factor is given by:

$${}^{s}k_{\mathrm{w},k_1} = \sin\left(\frac{s\pi y}{2p\tau_\mathrm{p}}\right) \frac{\sin\left(\frac{s\pi}{2pm}\right)}{q\sin\left(\frac{s\pi}{2pmq}\right)} \tag{3.53}$$

the associated winding factor of the k-th phase. Since the phase magnetomotive force (MMF) is periodic to the number of pole pairs, this must also apply to all its harmonics. It is therefore sufficient to summation with

$$s = p(2a + 1), a = 0, \pm1, \pm2, \ldots, \pm\infty. \tag{3.54}$$

The field excitation curve of the stator can then be transposed to the flux density with

$$B_{\delta,\text{Stator}}(x_1, t,r) = \mu_0 \frac{\Theta(x_1,t)}{\delta} \Lambda(x_1,r). \tag{3.55}$$

where Λ is the permeance function describing the effect of slotting, $B_{\delta,\text{Stator}}$ is the stator part of the air gap flux, and μ_0 is the magnetic field constant. The detailed determination of Λ is described in Section 3.2.3.

3.2.2.2 Rotor

This subchapter describes the magnetic modeling of the rotor field. The specific properties of the cylindrical magnet are examined and common approaches for SPMSM are studied and compared with FEA results. A new approach using a Neuronal Network (NN) to predict the permanent magnet field is proposed. To take into account the influence of the stator slot opening on the air gap field, NNs are trained with static FEAs.

In common modeling of SPMSMs, the magnet height is assumed to be constant and simplified as a rectangular magnet. Therefore, the resulting air gap field is constant across the width of the magnet. Thus, the air gap flux density (B_δ) for a magnet of constant height and small air gap can be calculated analytically by:

$$B_\delta = \frac{B_\text{R}}{1 + \frac{\delta}{h_\text{PM}} \frac{\mu_\text{PM}}{\mu_0}}, \tag{3.56}$$

where B_R is the remanence flux density of the magnet, δ is the length of the magnetic air gap, h_PM is the height of the magnet, μ_PM is the magnetic permeability of the magnet, and μ_0 is the magnetic field constant. This approach is tested with the FEA model shown in Fig. 3.11 (b). A C-shaped core with ideal material properties is modeled with $\mu_\text{Fe} \to \infty$ and a Permanent Magnet (PM) with $B_\text{R} = 1.05\,\text{T}$ and $\mu_\text{PM} = 1.06$ is placed in the air gap. The magnet height and the air gap length are varied in a range of $h_\text{PM} = \{4,6,..,30\}$ mm and $\delta = \{1,2,..,10\}$ mm. In Fig. 3.11 (a) the results are shown for a constant magnet height of $h_\text{PM} = 10\,\text{mm}$ and a variation of the air gap length. It can be seen that the results cal-

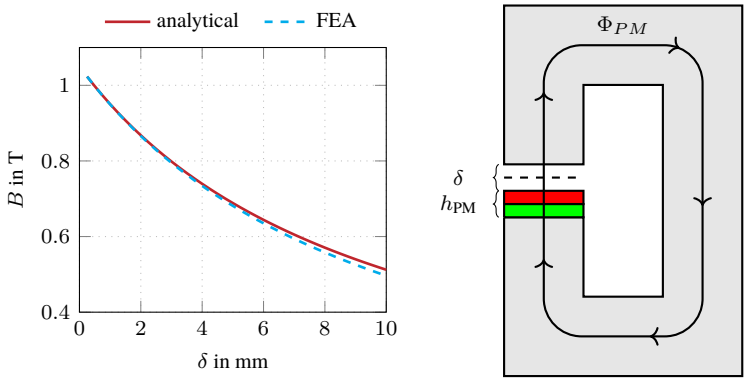

(a) $h_{\mathrm{PM}} = 10\,\mathrm{mm}$ (b) Sketch of FEA

Figure 3.11: Analysis of plane PM flux density with an ideal core material.

culated with eq. (3.56) agree well with the FEA results. As the air gap length increases, a small deviation can be seen. This is most likely due to the leakage flux closing around the air path and not over the core material. Further results from the same parameter study with a variation of the magnet height for different air gap lengths are shown in Fig. 3.12. It is observed that increasing the magnet height leads to an increase of the air gap flux density independent of the air gap width. The larger the air gap width, the larger the gradient of B_δ over the height of the magnet. As already seen in Fig. 3.11 (a), B_δ decreases with increasing air gap length. Overall, the results of eq. (3.56) agree very well with the results of FEA for a wide range of parameters.

In a second step, it is examined whether the approach can be applied to the proposed machine design. Since a diametrical magnetization results in a sinusoidal magnetic field, it is only tested if the amplitude, $\hat{B}_\delta$, can be determined. Therefore, a parameter study is performed with a static FEA. The model of the static FEA is shown in Fig. 3.13. It includes the cylindrical magnet with diametrical magnetization with its specific height h_{PM} and the air gap length δ. As in the previous analysis, the core material is ideal and $B_{\mathrm{R}} = 1.05\,\mathrm{T}$. To compare the numerical results with the analytical description, the flux density is evaluated at the magnet surface, since the surface area increases with radius r and $\hat{B}_\delta$ therefore decreases, but for eq. (3.56) constant surface areas are assumed. The results

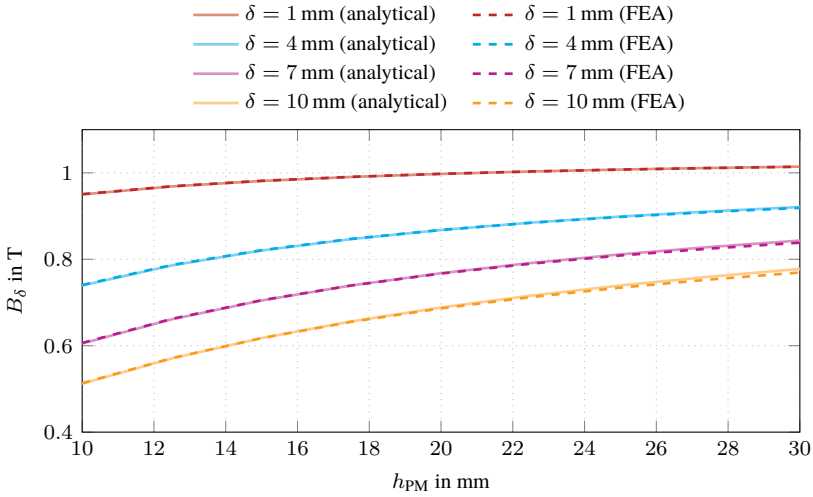

Figure 3.12: Analysis of plane PM flux density with ideal core material. Variation of magnet height h_{PM} and air gap length δ. Solid lines are the analytical results, dashed lines are the FEA results.

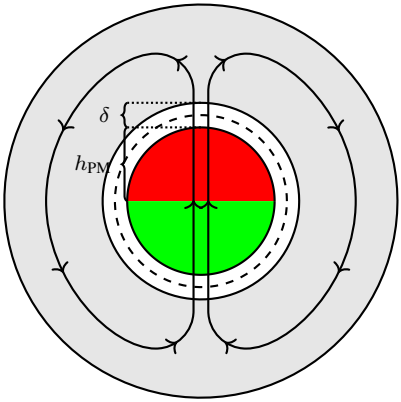

Figure 3.13: Model for analyzing the air gap flux density of a cylindrical solid permanent magnet with an ideal core material.

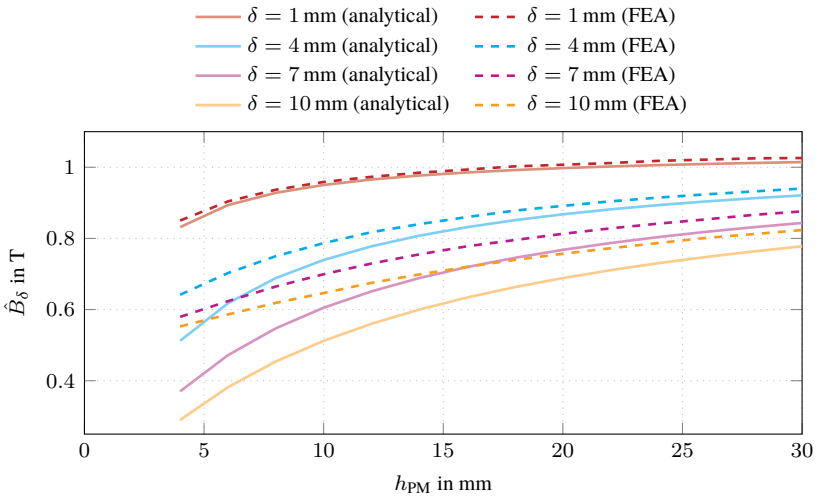

Figure 3.14: Cylindrical PM flux density analysis with ideal core material according to model Fig. 3.13, with variation of air gap length δ and magnet height h_{PM}. Solid lines are the analytical results, dashed lines are the FEA results.

are shown in Fig. 3.14. As expected, the highest values for $\hat{B}_\delta$ are obtained for small air gaps. The approach outlined in eq. (3.56) gives good results for small air gaps over the entire parameter range. For larger values of h_{PM}, the analytical and numerical results agree well, but with a tendency to larger deviations with increasing air gap lengths. In particular, for small magnet heights the deviations are larger, and for increasing air gaps the deviations between the analytical and numerical solution deviate by a factor of 2 for $\delta = 10\,\mathrm{mm}$. Overall, the gradient of $\hat{B}_\delta$ is much flatter compared to the analytical solution. The designs with small magnets must be taken into account when analyzing HSPMSM. Therefore, it is concluded that the increasing curvature with respect to the air gap length has a significant influence on the accuracy of eq. (3.56). Since the designs will most likely have larger air gaps due to the need for a sleeve and small radii due to the strength limitation of the rotor assembly, it is obvious that the approach is not accurate enough to model the PM flux for the application. When considering the flux density amplitude, it is important to consider the flux density curve over the length of the air gap. This is because the air gap area can not be assumed to

be constant. To analyze this, the air gap was divided into seven equally spaced segments, as shown in Fig. 3.15, and the flux density amplitude was evaluated at each point. This allowed the creation of a flux density curve, $\hat{B}_\delta(r)$, shown in Fig. 3.16. It is evident that the decrease is non-linear, indicating the need for a non-linear approach. This is counterintuitive since the area increases linearly with $A \propto \pi r$. This phenomenon is also described in [126].

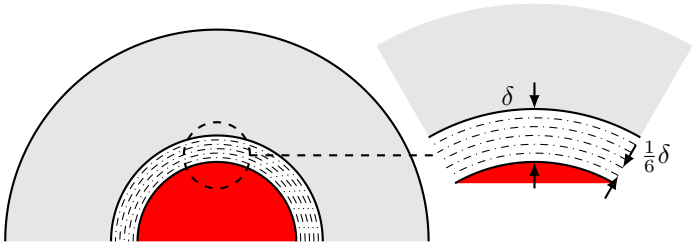

Figure 3.15: General model setup of the rotor field showing the evaluated radii in the air gap. Air gap divided into seven equally spaced segments; Counting starts from the magnet outwards.

Using Neuronal Networks to determine PM flux

For the analysis, the air gap is divided into seven segments as shown in Fig. 3.15. Static simulations were performed for the parameters $h_{\mathrm{PM}} = 4\,\mathrm{mm}$ to $30\,\mathrm{mm}$, with $2\,\mathrm{mm}$ as step size and $\delta = 1\,\mathrm{mm}$ to $12\,\mathrm{mm}$ in a $1\,\mathrm{mm}$ step size.

To determine $\hat{B}_\delta(r)$, a NN was trained using the MATLAB® Deep Learning Toolbox. The basics of NN can be found in [127] and are not discussed further in this work. The focus of this work is the use of the toolbox and the possibilities it offers. The training data included the parameters mentioned above. This training set was divided into three sub-sets. The training set contained $70\,\%$ of the data. In addition, the validation and test data sets contained $15\,\%$ each. The network consists of 1 hidden layer with 15 neurons. The result is a NN that can predict the flux amplitude at seven locations of the air gap and is further denoted as $N_{\mathrm{PM}}(\delta,h_{\mathrm{PM}})$. It is shown that the air gap flux density $\hat{B}_\delta$ can be normalized by the magnet remanence flux density B_{R} and therefore a material substitution can

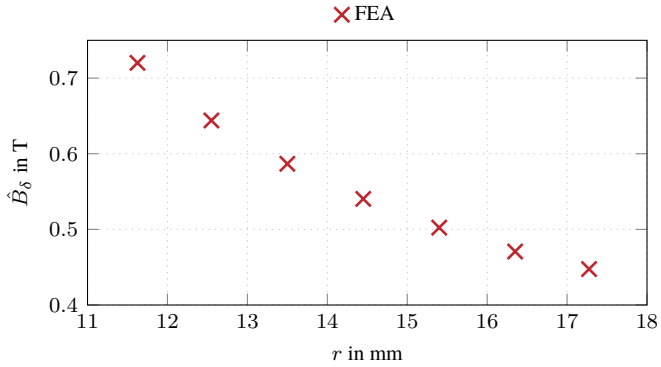

Figure 3.16: FEA results showing the variation of the radial air gap flux density over the machine radius.

be performed without any new calculation and training. For the later analysis, the flux density in the air gap must be known continuously. Therefore, a second order polynomial fit is used to calculate $\hat{B}_\delta(r)$. And assuming the field is sinusoidal, the radial rotor field can be calculated as

$$\boldsymbol{B}_{\delta,\mathrm{PM}}(r,\varphi) = N_{\mathrm{PM}}(\delta,h_{\mathrm{PM}})(r)\cos(\varphi). \tag{3.57}$$

3.2.3 Stator Slotting - Conformal Mapping

For PMSM, the stator side is usually slotted and therefore affects the air gap flux. Although air gap windings and slotless machines are commonly used for HSPMSM, the power density of machines with air gap windings is lower. The advantages of slotless machines are the constant torque and the sinusoidal air gap field, which results in lower rotor losses. For the same power, the slotless machine requires more magnetic material to achieve the same power. This results in higher circumferential speeds and higher mechanical stresses. It also requires more copper, which adds to the overall cost of a slotless design. [128, 129]. Due to the high power requirements of the reference machine, only the slotted designs are examined in this work. The cogging torque in high-speed machines with sleeves is relatively small due to the large air gap, and therefore is not a critical factor in the design of an electric compressor.
For analytical calculations, the Carter factor k_{C} was introduced in 1901. It de-

scribes the extension of the physical air gap length δ by k_C [52, 126]. This approach can determine the average flux density in the air gap, but not the detailed shape of the flux density. Therefore, conformal mapping [124, 126, 130, 131] or a separation approach [132] is used. For these solutions some simplifications have been made. The permeance of the slotted air gap region can be calculated by the conformal mapping method with a magnetic unit potential applied between the stator and rotor iron surfaces and no magnets present, and by assuming infinitely deep rectangular stator slots.
Zhu and Howe [126, 133–135] study the analytic description of SPMSM in detail. Based on these publications, [136] uses conformal transformations to calculate the radial and tangential air gap flux. The authors considered only a single stator slot, which does not affect the flux of the neighboring slot. This assumption can only be made because the neighboring slots do not impact each other. This assumption can not be made for the designs studied in this work. Furthermore, a flux concentration beneath the teeth can be observed for SPMSM machines [137]. These effects are not present in the solution presented by [124]. Thus, none of the known solutions fits the problem at hand. Therefore, a new method is proposed to determine the permeance function.

To model the effect of slotting, the previous 1D radial model without slots

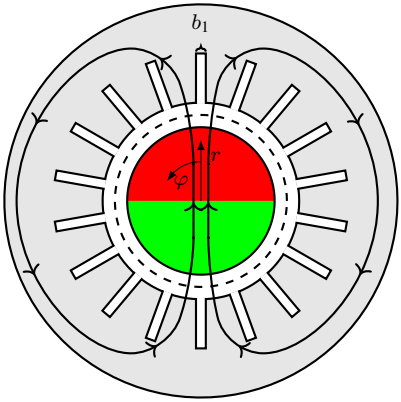

Figure 3.17: Modeling slotting in FEA

was extended by slots with slot opening width b_1. The model used is shown in Fig. 3.17. This level of detail is sufficient to model the influence of the slot opening as shown in [136], since most of the flux enters the tooth in the lower part

of the stator tooth due to $\mu_{\mathrm{Fe}} \to \infty$. This reduces the complexity of the model and the rest of the slot geometry is not modeled. Therefore, different models were created to represent different stator configurations. The data set is therefore extended by $b_1 = 1\,\mathrm{mm}$ to $3\,\mathrm{mm}$ in $0.5\,\mathrm{mm}$ steps. The air gap flux density B_δ is determined at the seven locations as shown in Fig. 3.15. This time, however, not only the amplitude is considered, but also the field distribution over $360°$. Therefore, it is possible to determine the permeance functions Λ as:

$$\Lambda_{\delta,h_{\mathrm{PM}},b_1}(r,\varphi) = \frac{\boldsymbol{B}_{\delta,\mathrm{h_{PM}},\mathrm{b_1}}(r,\varphi)}{\boldsymbol{B}_{\delta,\mathrm{h_{PM}}}(r,\varphi)}, \tag{3.58}$$

where $\boldsymbol{B}_{\delta,\mathrm{h_{PM}}}(r,\varphi)$ describes the air gap flux for a stator core without slots at r and φ. $\boldsymbol{B}_{\delta,\mathrm{h_{PM}},\mathrm{b_1}}(r,\varphi)$ is the corresponding air gap flux density of the stator core with slots. This results in a description of the permeance functions $\Lambda_{\delta,\mathrm{h_{PM}},\mathrm{b_1}}(r,\varphi)$ for each data point and is evaluated at the seven defined positions from Fig. 3.15.

Permeance Functions with Neuronal Networks

With the wide range of static FEA results, more NNs are trained. Testing has shown that for good results, a single NN should be trained for each position in the air gap. As before, the same net parameters were used with $70\,\%$ of the data used for training. For validation and testing, the data set contained $15\,\%$ each. Here, 1 hidden layer with 25 neurons are used. The resulting nets are noted as $\boldsymbol{N}_{\Lambda,i}$, where $i = 1,..,7$ is the index for each position in the air gap, starting at the outer magnet radius and ending at the stator bore radius. To calculate $\Lambda(r)$ for any r, a surface fit is performed and thus a function of $\Lambda(r,\varphi)$ is generated. For a more detailed understanding of the permeance function, the details are shown in Fig. 3.18. It shows the permeance function for $\frac{1}{18}$ of the circumference of the air gap as a contour plot. On the inside of the surface plot is the magnet surface. On the outer side is the stator surface and the slot opening. The radius of the sleeve is also shown to understand how the field is affected at the sleeve surface. It can also be seen that the permeance function is greater than 1 in a significant portion of the air gap. Additionally, it is seen that the permeance function has its maximum with overshoot near the slot opening, but decreases rapidly as it goes further towards the center of the machine.

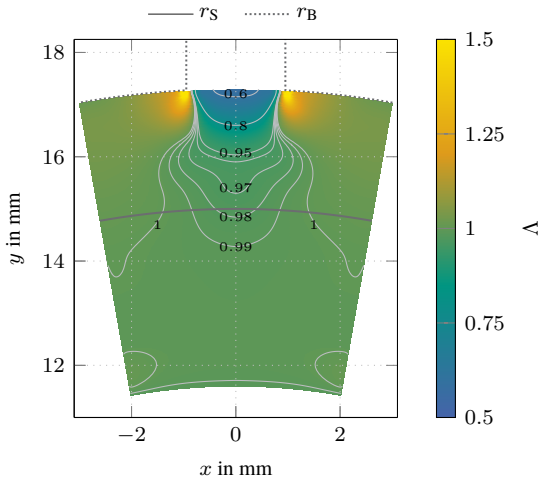

Figure 3.18: Permeance function for the reference machine. For an air gap segment over one stator slot.

3.2.3.1 Machine Air Gap Flux Density

In the next step the overall air gap flux density can be calculated. Therefore, the two flux densities $B_{\delta,\text{Rotor}}$ and $B_{\delta,\text{Stator}}$ can be summed up as

$$B_\delta(r,\varphi,t) = B_{\delta,\text{Rotor}}(r,\varphi,t) + B_{\delta,\text{Stator}}(r,\varphi,t) \tag{3.59}$$

Both fields need to be evaluated at the same radial position r. The opposing field of the stator is not considered when determining the magnetic operating point. This can be done at this point, as the amplitude of the stator field is small compared to the rotor field. As already introduced in Section 3.2.2.1 and eq. (3.55) the permeance function needs to be applied to the rotor and to the stator field. It needs to be taken care of the relative movement between the rotor and the stator. Therefore, the permeance function is static and is not moving, but the rotor and the rotating stator fields are. With that done, B_δ can be calculated at any position in the air gap.

3.2.4 Flux Linkages and Inductances

The turns of a coil, which are placed in two infinite narrow slots are completely passed through with the magnetic flux Φ_c. Therefore, the magnetic flux linkage for each coil can be determined with

$$\Psi_\delta = w_\mathrm{c}\Phi_\mathrm{c} = w_\mathrm{c}\frac{p}{\pi}\tau_\mathrm{p} l_\mathrm{Fe}\int_{\varphi_\mathrm{c}-\frac{y}{2}}^{\varphi_\mathrm{c}+\frac{y}{2}} B_\delta(r_\mathrm{B},\varphi,t)\,d\varphi. \tag{3.60}$$

The coil span is described by y and φ_c is the angle of the coil center. To calculate the flux linkage of the coils, the magnetic flux density at the bore radius r_B must be considered. This has to be done for each coil of each phase. Thus, the three-phase flux linkage can be determined and then transformed to the rotating dq reference frame. [138]
This describes only the main flux linkage of the machine. From here, the main inductances of the machine can be calculated with

$$L_\mathrm{q,main} = L_\mathrm{d,main} = \frac{\Psi_\mathrm{q,main}}{i_\mathrm{q}} \tag{3.61}$$

Where $L_\mathrm{q,main}$ and $L_\mathrm{d,main}$ are the inductances in the d and q directions. These two are equal because of the surface mounted permanent magnets. Furthermore, Ψ_q describes the flux linkage in q direction and i_q is the current in q axis.

3.2.4.1 Leakage Inductances

In addition to the fields that form the torque, the stator and rotor also generate fields that do not contribute to the formation of torque. These fields are called leakage fields and are only associated with the stator or rotor itself. Due to their size and geometry, HSPMSMs have a significant amount of leakage flux. The literature distinguishes between four different leakage fields. Slot leakage, tooth tip leakage, winding head leakage and harmonic leakage. All types are shown in Fig. 3.19. The latter is not scattering in the classical sense, but includes all harmonic fields that deviate from the fundamental wave theory. In the presented approach, the harmonic leakage is already included. Therefore, only the other three parts need to be considered. For the tooth tip leakage and the slot leakage an approach of [140] is used. The author's approach analyzes the inductive parameters of slot leakage in two-layer windings of unsaturated rotating electric machines. The author assumes the following:

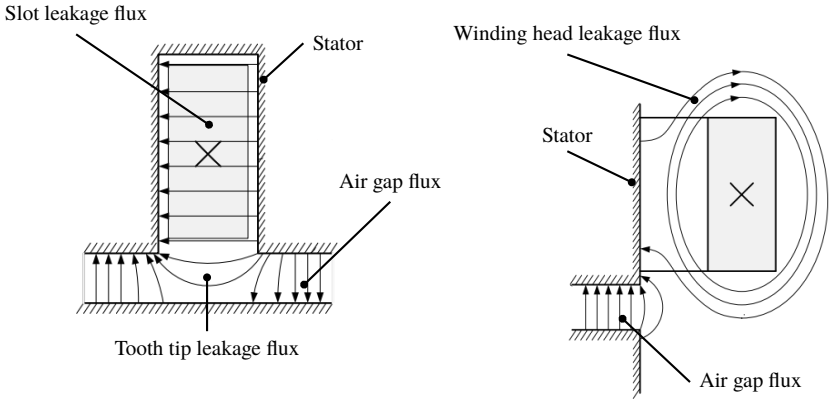

(a) Stator slot cross-section (b) Winding head cross-section

Figure 3.19: Air gap flux and the flux leakages in an electric machine [139]

- The magnetic field lines are parallel inside the slot and perpendicular to its axis of symmetry.
- The teeth's magnetic saturation and the voltage drop in iron related to the local field lines are neglected.
- The current distribution J in the conductors is uniform (but it can be different between the two layers, such as in the shortened pitch winding cases).

The proposed algorithm uses the well-known approaches for trapezoidal slots and discretizes the arbitrary slot geometry into small trapezoidal segments. Therefore, the slot is divided into several segments as shown in Fig. 3.20 (a). In this work, the coordinate system is on the inner diameter of the stator bore compared to the slot ground as done in [140]. The discretization of the slot assigns a width to each height x. Therefore, the following geometric relationships must be determined for each layer of the slot:

$$\begin{aligned} w_{m,k} &= \frac{w_k + w_{k-1}}{2} \\ \alpha_k &= \frac{w_k - w_{k-1}}{2w_{m,k}}. \end{aligned} \tag{3.62}$$

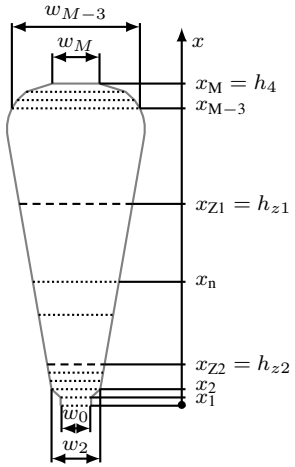

(a) Discretization of the arbitrarily shaped slot and the height-width table table. Coordinate system in the slot opening compared to [140]

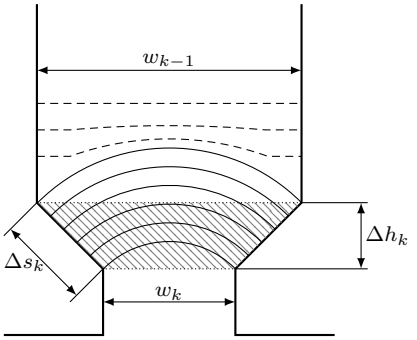

(b) Modification of the elementary layer thickness.

Figure 3.20: Slot geometry and modifications proposed by [140]

As shown in Fig. 3.20 (a), the slot is divided into two parts, the upper part for winding layer one and the lower part for winding layer two. The inductances are calculated separately and therefore the areas of the slot are assigned to each layer. The two boolean variables S_1 and S_2 describe this and are set as follows:

$$S_1 = \begin{vmatrix} 1 \; x_k > h_{z1} \\ 0 \; x_k \leq h_{z1} \end{vmatrix} ; S_2 = \begin{vmatrix} 1 \; x_k > h_{z2} \\ 0 \; x_k \leq h_{z2} \end{vmatrix}. \tag{3.63}$$

There, h_{z1} describes the height that divides the slot space into two equal cross-sections, taking into account an unfilled area at the bottom of the slot. Further, h_{z2} is the boundary where no more traces can be placed. These variables define all trapezoidal layers with respect to all other layers. Therefore, the self-

inductance of the two layers and their mutual inductance can be calculated by using the sums:

$$\begin{aligned}
\frac{\Lambda_1}{\mu_0 l_{\mathrm{Fe}}} &= \left\{ \sum_{k=1}^{N} \left[\frac{\Delta s_k}{w_{m,k}} \left(S_1 K_1\left(\alpha_k\right) + \overline{S_1} K_0\left(\alpha_k\right) \right) \right] + \frac{\Delta h_{\mathrm{sg}}}{b_1} \right\} \\
\frac{\Lambda_2}{\mu_0 l_{\mathrm{Fe}}} &= \left\{ \sum_{k=1}^{N} \left[\frac{\Delta s_k}{w_{m,k}} \overline{S_1} \left(S_2 K_1\left(\alpha_k\right) + \overline{S_2} K_0\left(\alpha_k\right) \right) \right] + \frac{\Delta h_{\mathrm{sg}}}{b_1} \right\} \\
\frac{\Lambda_{12}}{\mu_0 l_{\mathrm{Fe}}} &= \left\{ \sum_{k=1}^{N} \left[\frac{\Delta s_k}{w_{m,k}} \overline{S_1} \left(S_2 K_M\left(\alpha_k\right) + \overline{S_2} K_0\left(\alpha_k\right) \right) \right] + \frac{\Delta h_{\mathrm{sg}}}{b_1} \right\} \\
&\begin{cases}
L_{\sigma 1} = w^2 \Lambda_1 \\
L_{\sigma 2} = w^2 \Lambda_2 \\
M_{\sigma 12} = w^2 \Lambda_{12}
\end{cases}
\end{aligned} \tag{3.64}$$

Therefore, the following description of the geometry factors K_1, K_0 and K_M are required:

$$\begin{cases}
K_1(\alpha) = \dfrac{1}{16\alpha^2} \left(\dfrac{(\alpha-1)^4}{2\alpha} \log \dfrac{1+\alpha}{1-\alpha} - \alpha^2 + 4\alpha - 1 \right) \\
\qquad\quad \approx \dfrac{1}{3} - \dfrac{\alpha}{3} + \dfrac{\alpha^2}{5} \left(\begin{array}{c} \text{approximations for} \\ -0.1 < \alpha < 0.1 \end{array} \right) \\
K_0(\alpha) = \dfrac{1}{2\alpha} \log \dfrac{1+\alpha}{1-\alpha} \approx 1 + \dfrac{\alpha^2}{3} \\
K_M(\alpha) = \dfrac{1}{4\alpha} \left[1 - \dfrac{(\alpha-1)^2}{2\alpha} \ln\left(\dfrac{1+\alpha}{1-\alpha} \right) \right] \approx \dfrac{1}{2} - \dfrac{\alpha}{3} + \dfrac{\alpha^2}{6}
\end{cases} \tag{3.65}$$

In addition, Δh_{sg} is defined as

$$\Delta h_{\mathrm{sg}} = \delta \left(1 - \frac{2\xi_{\mathrm{a}} \arctan\left(\xi_{\mathrm{a}}\right) - \ln\left({\xi_{\mathrm{a}}}^2 + 1\right) + 2\ln(2)}{\pi \xi_{\mathrm{a}}} \right) \tag{3.66}$$

Δh_{sg} represents, depending on the sign, the increase or decrease of the equivalent height of the slot. This accounts for the field line fringing inside the air gap, corresponding to its opening. For PMSM, Δh_{sg} is usually positive and therefore

the leakage inductance contribution is positive. However, it can become negative if the air gap is small in comparison to the slot opening, as in induction machines. The missing factor ξ_{a} is defined by

$$\xi_{\mathrm{a}} = \frac{2\delta}{b_1}. \tag{3.67}$$

To compensate for the field distortions that occur when the edges of the slot profile are not parallel, the field lines exit the iron-air interface perpendicularly and are curved to maximize the permeance of their path (see Fig. 3.20 (b)). For this reason, the author suggests using the length of the edge Δs_k instead of the height of an element.

$$\Delta s_k = \sqrt{\Delta {h_k}^2 + \left(\frac{w_k - w_{k-1}}{2}\right)^2} \tag{3.68}$$

The leakage inductance for a single slot can be used to determine the slot leakage inductance and the tooth tip inductance of a double layer winding. In eq. (3.69) the formulation for a three-phase double layer winding is noted. The following equation is valid only for $mq - y \leq q$:

$$L_{\sigma,\,\mathrm{sl}} = \frac{w^2}{2qp}\left[\Lambda_1 + \Lambda_2 + \left(1 - \frac{mq - y}{2q}\right) 2\Lambda_{12}\right] \tag{3.69}$$

Furthermore, the inductance of the winding head is part of the modeling. Therefore, the approach proposed by [141] is used to estimate the length of the winding head. In this paper, the winding length is determined for different winding layouts and the formulations are described. In the following, the winding length is determined by the stator active length l_{Fe} and the additional winding head length, which is a factor based on the average slot radius and the ratio of slots to poles. This is summarized in the factor k_c.

$$l_{\mathrm{wh}} = k_c \frac{2\pi r_{\mathrm{w}}}{N} \tag{3.70}$$

$$k_c = \frac{\pi}{4}\frac{N}{p} \tag{3.71}$$

The inductance of the winding head leakage is determined by a common formula without differentiating between single layer and double layer windings.

The winding head leakage is determined by the winding head length of a coil head l_{wh} and the relative leakage conductance λ_{wh}. The reference values are the relative leakage conductances suggested in the literature. For this work, the relative leakage conductance $\lambda_{\text{wh}} = 0.3$ is used according to [139]. This value gives good results in practice for three-phase distributed two-layer windings.

$$L_{\text{wh}} = 2\mu_0 l_{\text{wh}} \frac{w^2}{p} \lambda_{\text{wh}} \tag{3.72}$$

Thus, the total leakage inductance L_σ can be determined by summing all three determined leakage inductances.

$$L_\sigma = L_{\sigma,\,\text{sl}} + L_{\text{wh}} \tag{3.73}$$

Where $L_{\sigma,\,\text{sl}}$ contains the two parts of the slot leakage flux and the air gap leakage flux.

3.2.5 Phase Resistance

The phase resistance of the entire machine is the last parameter of the machine model to be determined. As already described for the calculation of the winding head inductance, the same calculation can be used (eq. (3.70)). In addition to the winding head length, the active length must be added to obtain the total winding length l_{c}.

$$l_{\text{c}} = l_{\text{wh}} + l_{\text{Fe}} \tag{3.74}$$

With the winding length l_{wh}, the conductor cross section A_{c}, the specific resistance ρ_{c} and the number of turns the winding resistance R_{l} can be calculated:

$$R_{\text{l}} = \frac{2 l_{\text{c}} w \rho_{\text{c}}}{A_{\text{cond}}} \tag{3.75}$$

It is important to note that l_{c} is only including a half turn and therefore needs to be multiplied by the factor of 2.

3.2.6 Inner Torque

With the three phase flux linkages and the leakage inductances, the machine parameters can be transformed to the rotor oriented dq reference frame. The details and transformations are not explained in this work, but can be found in any basic

literature on electric machines. For the calculation of the electric torque T_{el} the machine parameters Ψ_{PM} must be known. Therefore, the flux linkages for the no-load operating point, with $i_{\mathrm{d}} = i_{\mathrm{q}} = 0$, are calculated and transformed to the dq reference frame. The flux linkage in the d-direction is defined as

$$\Psi_{\mathrm{d}} = \Psi_{\mathrm{PM}} + L_{\mathrm{d}} i_{\mathrm{d}} \tag{3.76}$$

For the no load operating point the permanent magnet flux linkage Ψ_{PM} is equal to Ψ_{d}. In a second step, the current dependent inductances are determined with the operating point of any load current $i > 0\,\mathrm{A}$. With eq. (3.61) the main inductance L_{d} and L_{q} is determined. Knowing the inductances, the leakage inductances can be added to the main inductances. And the total flux linkages can be calculated.

$$\begin{aligned} \Psi_{\mathrm{d}} &= \Psi_{\mathrm{d,main}} + L_{\sigma} i_{\mathrm{d}} \\ \Psi_{\mathrm{q}} &= \Psi_{\mathrm{q,main}} + L_{\sigma} i_{\mathrm{q}} \end{aligned} \tag{3.77}$$

Therefore, the parameters of the stationary machine model are determined and the inner torque and the required voltages of the machine can be determined.

$$T_{\mathrm{el}} = \frac{3}{2} p \Psi_{\mathrm{PM}} i_{\mathrm{q}} \tag{3.78}$$

This is only the case for fully symmetric machines where L_{d} is equal to L_{q} and the reluctance torque of the electric machine is zero.

3.2.7 Machine Losses

As described in Section 2.2.2.2, the losses in HSPMSM are highly dependent on the electric frequency. As it is already defined by the rotor design, the maximum number of poles in the investigated concept is two. The losses and their frequency dependency are one of the main reasons for choosing a design with only one pole pair. In the proposed model, the core losses, the rotor eddy current losses, the DC copper losses and the friction losses on the rotor surface are considered.

3.2.7.1 Core Losses

The standard approach to determine the core losses of an electric machine during the design process is the use of FEA. The transient solution of the model gives detailed information about the flux density distribution and its variation with

time. In FEA the Bertotti models are used [D8]. To have a proper comparison with the FEA, the same model is used as in Ansys Maxwell.

$$P_{\mathrm{Fe}} = C_{\mathrm{dc}} k_{\mathrm{h}} f \left(\hat{B}\right)^2 + k_{\mathrm{c}} \left(f\hat{B}\right)^2 + k_{\mathrm{e}} \left(f\hat{B}\right)^{1.5} \tag{3.79}$$

$$C_{\mathrm{dc}} = 1 + k_{\mathrm{DC}} {B_{\mathrm{dc}}}^2 \tag{3.80}$$

The DC loss component is listed for completeness and is relevant for the rotor core parts but not for the stator parts since the stator has no pre-magnetization and will always have a mean flux density of zero over time. The electric frequency f and the flux density amplitude $\hat{B}$ are seen to be the main determinants of the losses. At high speeds the eddy current losses become dominant. As described in eq. (2.3), the sheet thickness is an important factor to keep the losses small. To determine the losses, the flux density amplitude needs to be determined. Therefore, the air gap flux density $B(r_{\mathrm{B}},t,\varphi)$ is used as a basis. In the next step it is assumed that the flux density has only a radial component and that all the flux from the center of one slot opening to another is evenly distributed in a stator tooth. Therefore, a flux amplitude is determined in each tooth. The stator yoke is considered as a ring of height

$$h_{\mathrm{y}} = \frac{d_{\mathrm{O,S}}}{2} - r_{\mathrm{B}} - h_4. \tag{3.81}$$

In here $d_{\mathrm{O,S}}$ describes the stator outer diameter, r_{B} is the bore radius and h_4 the slot height. To estimate the amplitude of the stator yoke flux, the following assumption is made:

$$\hat{B}_y = q\overline{\hat{B}_T}\frac{b_2}{h_{\mathrm{y}}} \tag{3.82}$$

Therefore, only the main magnetic flux component is used and the magnetic flux density $\overline{\hat{B}_T}$ is scaled by the stator tooth width b_2 multiplied by the number of slots per phase and pole and divided by the height of the stator yoke. With the amplitude of the flux density determined, the core losses can be calculated.

3.2.7.2 Rotor Eddy Current Losses

One of the most critical aspects in the design of a HSPMSM is the determination of the temperature and losses in the rotor. In Fig. 3.21 the cross section of the investigated rotor design is shown. The cylindrical magnet is protected by a metal sleeve.

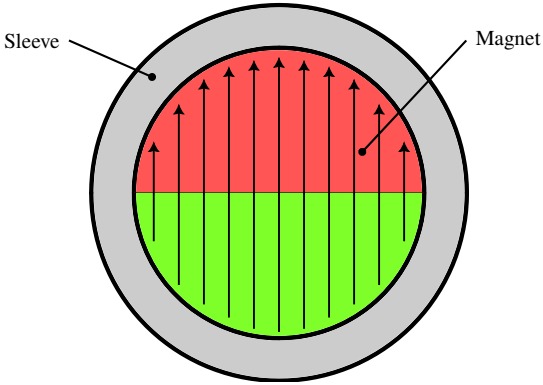

Figure 3.21: Rotor cross-section with the cylindrical magnet, the sleeve and the magnetization direction.

A simplified method proposed in [142] to determine the PM eddy current loss caused by the stator slot is presented. The mean value of the eddy current losses of the PMs or in this work, the sleeve can be expressed as [142].

$$\overline{P_{\mathrm{c}}} = \frac{\sigma l_{\mathrm{Fe}} t_{\mathrm{S}} B_{\delta 0}(r)^2 \omega^2 {r_{\mathrm{S}}}^2 w_{\mathrm{S}}}{2} \sum_n K_n^2 \left[1 - \left(\frac{s}{\pi n w_{\mathrm{S}}} \sin \frac{\pi n w_{\mathrm{S}}}{s} \right)^2 \right]. \quad (3.83)$$

Here $B_{\delta 0}$ is the amplitude of the fundamental air gap flux density and K_n is the coefficient of the Fourier series of the modulation function obtained by the conformal mapping method [142, 143]. For easier handling, the flux density of the center air gap position in the static state can be used to calculate the coefficients K_n. The radial position must be taken into account. Furthermore, the average sleeve width w_{S} and the slot width s are defined:

$$w_{\mathrm{S}} = 2\pi \frac{(r_{\mathrm{S}} + r_{\mathrm{M}})}{2} \quad (3.84)$$

$$s = r_{\mathrm{B}} \frac{2\pi}{N} \quad (3.85)$$

Ou [87] found that this method does not consider the variation of the eddy current in the thickness direction of PM, therefore the calculation error at high speed is large. To solve this problem, the PM is divided into x layers in thickness, then

the coefficients K_n are replaced by $K_n(r_\mathrm{S})$. For this work, only the losses in the sleeve are considered, so the proposed formula is modified and is expressed as

$$\begin{aligned}\overline{P_\mathrm{c}} = &\int_{r_\mathrm{M}}^{r_\mathrm{S}} \frac{\sigma l_\mathrm{Fe} t_\mathrm{S} B_{\delta 0}(r)^2 \omega^2 {r_\mathrm{S}}^2 w_\mathrm{S}(r)}{2x} \\ &\cdot \sum_n K_n(r)^2 \left[1 - \left(\frac{s}{\pi n w_S(r)} \sin \frac{\pi n w_S(r)}{s}\right)^2\right] dr\end{aligned} \tag{3.86}$$

where $w_\mathrm{S}(r)$ is the average width of the sleeve segment and $K_n(r)$ are the coefficients of the Fourier series of the flux density at the radius r. In this way it is possible to determine the eddy current losses in the sleeve. In general, the currents in the stator windings will not be sinusoidal as assumed in the calculations for this work. The rotor eddy current losses will therefore be significantly affected by the current ripples. In [87] it is also shown that the losses are significant.

3.2.7.3 Copper Losses

In the copper losses, only the DC copper losses are considered, although the AC losses are usually a significant part due to proximity effects in HSPMSM. Only FEA is able to determine the AC losses accurately and is therefore not considered in this work. With the determination of the phase resistance R_1 and the knowledge of the RMS value of the phase current i_RMS, the losses can be determined for the three-phase winding.

$$P_\mathrm{DC} = 3 R_1 {i_\mathrm{RMS}}^2 \tag{3.87}$$

3.2.7.4 Windage Losses

In addition to the mechanical limitation, rotor windage losses are also a challenge for high-speed motors. In general, the rotor windage losses P_wind can be calculated by [144]

$$P_\mathrm{wind} = k_1 C_\mathrm{f} \pi \rho_\mathrm{air} \omega^3 {r_\mathrm{S}}^4 l_\mathrm{Fe} \tag{3.88}$$

Here k is the roughness coefficient, its value is 1 for smooth surfaces and 2.5 for axially slit surfaces [145]. C_f is the friction coefficient, ρ_air is the density of air in kg m^{-3} and ω is the angular velocity of the rotor. To improve the heat dissipation ability of the stator, the stator is encapsulated with epoxy resin. Then the inner surface of the stator becomes a smooth surface and the roughness coefficient is

equal to 1. It can be found that by encapsulating the stator with epoxy resin, not only the heat dissipation ability of the stator is improved, but also the rotor windage loss can be reduced. To determine the windage losses, the coefficients of friction and the Reynolds number must be determined. The Couette-Reynolds number is required, which is a dimensionless number that describes the tangential gas flow characteristics. It is expressed as

$$\mathrm{Re}_\delta = \frac{\rho_{\mathrm{air}} \omega r_{\mathrm{S}} \delta_{\mathrm{mech}}}{\mu} \tag{3.89}$$

in which μ describes the dynamic viscosity of air and δ_{mech} the gap between the sleeve and the bore inner radius. Further, the friction coefficient can be determined as

$$\begin{cases} C_{\mathrm{f}} = 0.515 \frac{\left(\frac{\delta_{\mathrm{mech}}}{r_{\mathrm{S}}}\right)^{0.3}}{\mathrm{Re}_\delta{}^{0.5}}, & 500 < \mathrm{Re}_\delta < 10^4 \\ C_{\mathrm{f}} = 0.0325 \frac{\left(\frac{\delta_{\mathrm{mech}}}{r_{\mathrm{S}}}\right)^{0.3}}{\mathrm{Re}_\delta{}^{0.2}}, & 10^4 < \mathrm{Re}_\delta \end{cases} \tag{3.90}$$

Air density and dynamic viscosity must be considered as a function of temperature.

3.3 Thermal Modeling

This section presents the thermal modeling of the electric machine. The main focus of this work is the development of a preliminary design tool for an electric compressor with air foil bearings. The thermal behavior of the system depends on numerous factors, including bearing losses, which could not be modeled due to the lack of a reliable loss model, and the need for ventilation flows to maintain bearing temperatures. In addition, the influence of the compressor and turbine on the thermal household was excluded because it depends on external parameters such as the fuel cell exhaust and inlet temperatures, which are beyond the scope of this study. Consequently, the focus is placed on the electric machine, where a simplified 2D FEA model is developed to evaluate the heat conduction. The geometry is created in ANSYS Maxwell, and the meshing and solving are performed in MATLAB® using the PDE toolbox. Boundary conditions and heat transfer mechanisms are described in detail in this section.

3.3.1 Cooling Boundaries

The critical temperatures and therefore performance limiting factors are the copper temperatures and the magnet temperatures. It is well known that the maximum copper temperature is limited by the temperature classification of the copper wire. For this type of application, the temperature class is chosen to be H (180 °C). For the magnet, Sm_2Co_{17} is selected and therefore a temperature limit of 200 °C is considered.

3.3.1.1 Liquid Cooling

As in the reference machine, liquid cooling with water and glycol is assumed. For the selected model, the liquid cooling itself is not modeled. Due to the expected heat transfer into the liquid cooling, it is assumed that the stator surface has a constant temperature. This is possible because the liquid temperature itself does not vary much between the inlet and outlet. As an example, heating one liter of a water-glycol mixture (50/50) with 100 W, the temperature difference can be determined as follows:

$$\Delta T = \frac{\dot{q}}{c_\mathrm{p} \cdot \dot{m}} = \frac{100\,\mathrm{J\,s^{-1}} \cdot \frac{60\,\mathrm{s}}{\mathrm{min}}}{3500\,\mathrm{J\,kg^{-1}\,K^{-1}} \cdot 1.11\,\mathrm{kg\,s^{-1}}} = 1.54\,\mathrm{K} \tag{3.91}$$

For the expected application volume flows of more than six liters per minute can be assumed. So for a power loss of 1 kW the temperature rise is only about 2.6 K.

3.3.2 Heat Transfer in the Air Gap

The heat from the rotor must be dissipated through the air gap to the stator. Air is a poor conductor of heat, but in the air gap the air is swirled by high rotational and circumferential speeds, which can improve heat transfer. In theory, heat transfer can be by convection and radiation. In this application, convection is dominant. This is because the temperatures are below 200 °C. [146]. The heat dissipation can be improved with forced ventilation, for example with an air flow through the air gap. The heat transfer coefficient of the air gap is required to calculate the temperature rise of the rotor.

3.3.2.1 Flow Modes

As the rotor speed increases, the flow mode of the air gap changes from pure laminar flow to Taylor vortices and finally to turbulent flow, and the heat convec-

tion capability is continuously improved. Generally, the flow modes of the air gap are divided into four modes as follows [147, 148]. To predict the transition

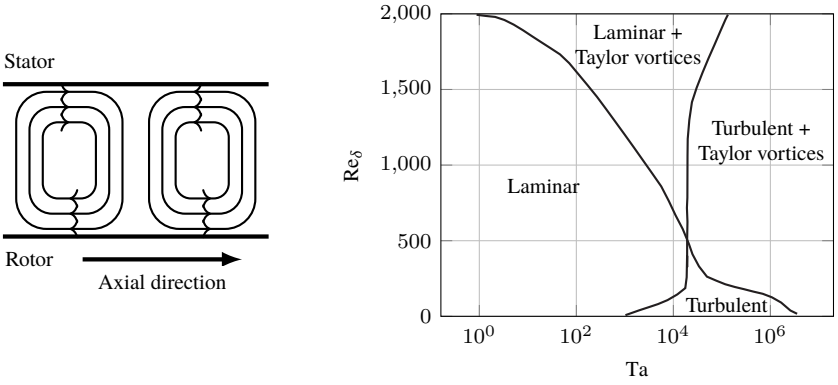

(a) Taylor vortices

(b) Flow regimes as a function of Re_δ and Ta

Figure 3.22: Flow regimes in the air gap of electric machines [148].

of flow modes, the Reynolds number Re is commonly used. It is a dimensionless quantity that represents the ratio of inertial forces to viscous forces in a fluid and describes the turbulence that occurs in the flow. In an annular air gap between the stator and rotor, it can be expressed as introduced in eq. (3.89)

$$\mathrm{Re} = \frac{\omega \delta_{\mathrm{mech}} r_{\mathrm{S}}}{\nu_{\mathrm{air}}} \tag{3.92}$$

Another non-dimensional quantity, which is used in annular geometries is Taylor number Ta which is based on the mean angular radius r_{avg} of the bore radius r_{B} and the sleeve radius, which is defined as

$$r_{\mathrm{avg}} = \frac{r_{\mathrm{B}} + r_{\mathrm{S}}}{2}. \tag{3.93}$$

It is the ratio of the centrifugal to the viscous forces and can be expressed as [144, 149]

$$\mathrm{Ta} = \frac{\omega^2 {\delta_{\mathrm{mech}}}^3 r_{\mathrm{avg}}}{{\nu_{\mathrm{air}}}^2} \tag{3.94}$$

The critical Taylor number is 1700. For larger values, the Taylor vortices are formed and the following approach can be used to determine the convective heat transfer coefficient. To calculate the heat transfer, the Nusselt number Nu is used, which is a dimensionless description of the heat transfer. It is defined as

$$\mathrm{Nu} = \frac{h d_\mathrm{h}}{\lambda} \tag{3.95}$$

where h is the convective heat transfer coefficient and λ is the thermal conductivity of the fluid. The hydraulic diameter is denoted by d_h and is defined as $d_\mathrm{h} = 2\delta_\mathrm{mech}$. Becker and Keyes [150] define Nu as

$$\mathrm{Nu} = 0.409 \cdot \left(\frac{\mathrm{Ta}}{F_\mathrm{g}}\right)^{0.241}, \qquad 10^4 < \mathrm{Ta} < 10^7. \tag{3.96}$$

The range of the Taylor number is sufficient to be considered in this work, as shown in Fig. 3.23. For a small rotor with $r_\mathrm{S} = 7.5\,\mathrm{mm}$ and an air gap $\delta = 0.5\,\mathrm{mm}$, Ta is reached before $20\,000\,\mathrm{min}^{-1}$. For larger rotors and larger air gaps, Ta increases and therefore does not need to be considered. It can happen that the range of $\mathrm{Ta} > 10^7$ is reached. Therefore the definition of Becker and Kaye is still used, since no other definition is available. The geometry factor F_g is defined as follows. There are many factors defined in the literature. The one used is found in many publications and is therefore used [147].

$$F_\mathrm{g} = \frac{\pi^4}{1697 \cdot S} \left(1 - \frac{\delta_\mathrm{mech}}{2 \cdot r_\mathrm{avg}}\right)^{-2} \tag{3.97}$$

$$\begin{aligned} S = 0.0571 &\left(1 - 0.652 \frac{\frac{\delta_\mathrm{mech}}{r_\mathrm{avg}}}{1 - \frac{\delta_\mathrm{mech}}{2 r_\mathrm{avg}}}\right) \\ +0.00056 &\left(1 - 0.652 \frac{\frac{\delta_\mathrm{mech}}{r_\mathrm{avg}}}{1 - \frac{\delta_\mathrm{mech}}{2 r_\mathrm{avg}}}\right)^{-1}. \end{aligned} \tag{3.98}$$

3.3.3 2D-FEA Thermal Modeling

A 2D-FEA is used to determine the component temperature and especially the critical temperatures. This approach does not include the influence of the turbomachinery on the system. A lumped parameter model would be the proposed

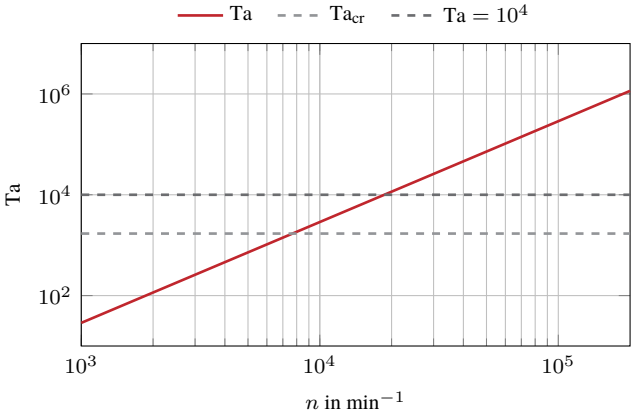

Figure 3.23: Taylor number Ta as a function of the rotational speed n for a rotor radius $r_S = 7.5\,\text{mm}$ with a mechanical air gap length of $\delta_{\text{mech}} = 0.5\,\text{mm}$

approach for modeling the entire system to include the details of bearing losses and compressor losses.

3.3.3.1 Model

The machine geometry and loss distribution can be assumed to be symmetric. Therefore, the system can be simplified to the smallest symmetrical part, which is a segment of a single stator slot. This can be determined by the first law of thermodynamics, since the energy balance for all N machine segments is equal. The geometry of the rotor and stator is straightforward and needs no further explanation. To get a more realistic model of the slot, the winding is modeled with individual conductors. An algorithm places conductors in both layers to achieve the desired winding configuration. The conductor is modeled with its insulation material. A constant material thickness of $0.033\,\text{mm}$ is assumed. The slot insulation and the phase separator are also modeled. The material thickness is $0.2\,\text{mm}$.
Since the model is symmetric, there is no tangential heat flow across the boundaries of the model. The outer temperature of the stator is set to $T_{\text{cool}} = 60\,°\text{C}$. The heat transfer from the rotor to the stator is modeled as described above. The resulting Nu is multiplied by the thermal conductivity of the air. In addition, the

material specifications summarized in Table 3.2 are used.
Due to the application, only the static temperature distribution is of interest for the results. Therefore, only the static solution is considered. This further reduces the simulation time compared to a transient simulation. If overload cases would be considered in other use cases, it should be considered to use transient models to determine the overload capability of the machine.

Table 3.2: Material parameters used for the thermal simulation of the machines

	Material -	ρ $\mathrm{kg\,m^{-3}}$	c_p $\mathrm{J\,kg^{-1}\,K^{-1}}$	λ $\mathrm{W\,m^{-1}\,K^{-1}}$
Stator	NO20	7600	449	21
Winding	Cu	8920	368	385
Lacquer	-	1440	1000	0.22
Potting	-	1850	1100	0.7
Insulation paper	Nomex-Kapton-Nomex	868	1956	0.12
Sleeve	Inconel 718	8820	449	13.1
	TiAl6V4	4430	538	7.2
Magnet	Sm_2Co_{17}	8400	377	11

3.4 Design Procedure

This section outlines the overall multi-physics design process. The previous sections address the design of a HSPMSM, which includes the determination of the compressor and turbine dimensions if a turbine application is considered (Section 3.1.1). Following this design step, the mechanical design phase focuses on the strength analysis of the sleeve and magnet assembly (Section 3.1.2). It also includes the determination of the natural frequency of the shaft assembly. The magnetic design is then optimized, with detailed subtopics discussed in Section 3.2. The final step in the design process is the thermal validation (Section 3.3).

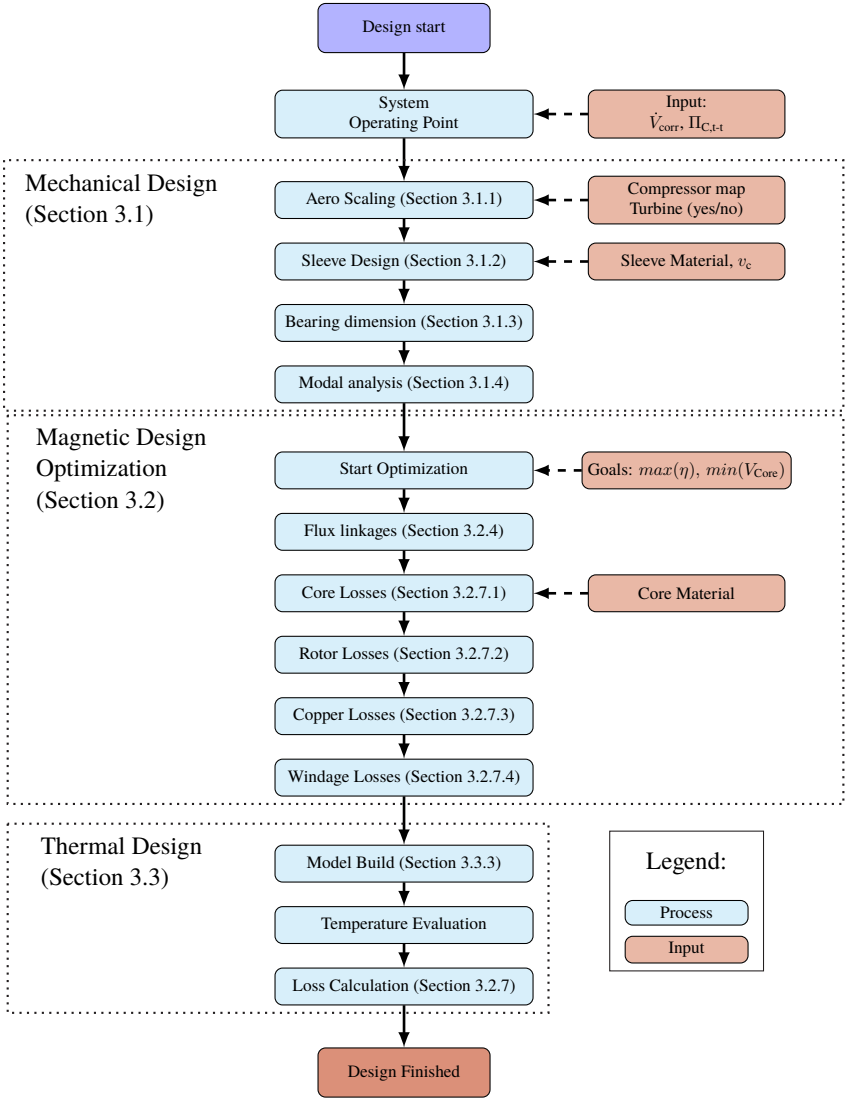

Figure 3.24: Design Flowchart

3.4.1 Boundaries

A design process is guided by the constraints and goals set. The design approach presented focuses on the application and the requirements usually derived from the application. For a fuel cell system, the requirement is a volume flow $\dot{V}_{\text{corr}}$ and a pressure ratio $\Pi_{\text{C,t-t}}$ to be provided by the electric compressor. In addition, it could be specified whether a turbine should be added to the system to increase efficiency. These are the main input parameters for the design process. The safety factors for the design process are described in Section 3.1.2. More information can be found in the corresponding section. The goal of system design is to maximize efficiency. Therefore, the design objective for determining the aerodynamic components and the electrical machine is to minimize losses.

3.4.2 Design Process

The detailed design process is shown in Fig. 3.24. The description of the design process focuses on the determination of the relevant machine parameters in order to perform a consistent sizing that meets the system requirements. The first step in any design process is to determine the design objectives. In addition, the circumferential speed range of the electric machine and the shaft material must be specified. In this work, only isotropic materials are considered. Therefore, the design process starts with the optimization of the compressor, which is the main load of the machine, in order to determine the following variables. On the one hand, the geometric dimensions of the compressor wheel are determined. On the other hand, the operating point of the compressor is determined, which includes the efficiency of the compressor. This results in the speed n at which the system will operate, the efficiency $\eta_{\text{C,is}}$ and therefore the required shaft torque T_{sh}. If necessary, the turbine size and efficiency are determined. Therefore, the regenerated power P_{T} and the torque T_{TW} are determined. This results in the required torque to be supplied by the electric machine T_{EM}. The next step is to calculate the overall dimensions of the shaft. This involves calculating the bearing diameter and length. It is followed by dimensioning the sleeve thickness and the resulting magnet diameter. By specifying the circumferential speed of the rotor v_{c}, the outer radius of the sleeve is calculated with

$$r_{\text{S}} = \frac{v_{\text{c}}}{\omega_{\text{max}}}, \tag{3.99}$$

where ω_{max} is the maximum expected speed. In the design process and in the presented results, an overspeed of $5\,\%$ is considered. To find the minimal ap-

plicable sleeve thickness, a binary search is used. Therefore, the solution space is discretized in $0.05\,\mathrm{mm}$ steps. Starting with $1\,\mathrm{mm}$ and going up to the outer sleeve radius r_S. Therefore, only a limited number of designs will be calculated. In addition to the stress requirements, the algorithm also determines the overlap of the sleeve magnet interference fit and its minimum and maximum overlap and checks if the combination can still be assembled according to DIN 7190 [118]. If both conditions are met, the minimum sleeve thickness is found and all shaft dimensions are determined except for the active length l_Fe of the electric machine. This cannot be determined at this point, but the maximum length can be determined because it is limited by the eigenfrequency of the shaft. Therefore, the maximum length is determined by a parameter sweep with four different lengths. With the maximum allowed frequency $f_\mathrm{cr} = 1.2 \cdot \frac{n_\mathrm{max}}{60}$ it is interpolated to the critical active length of the proposed design.
In the next step, the electromagnetic design of the machine is calculated and optimized. The goal of the optimization is to minimize losses. Other factors such as volume are included in a multi-parameter optimization. All kinds of objectives can be implemented if needed. To reduce the optimization time and the number of parameters, some constraints have to be discussed.
Since the rotor geometry is already determined in its cross-section, the optimization focuses on the stator and winding design. Therefore, the parameters can be divided into two groups. On the one hand the winding parameters, which are the number of slots per phase and pole q, the coil span y and the number of turns per coil w_c. On the other hand, the stator slot geometry is defined by the tooth width b_t, the slot opening b_1, the air gap length δ, the slot height h_4 and the active length l_Fe. All other geometry parameters can be calculated by assuming parallel tooth edges, a constant radius at the bottom of the slot and constant tooth foot heights. For the outer diameter, constant cross-sections are assumed. Therefore, the stator outer diameter $d_\mathrm{O,S}$ increases with the stator tooth width by a factor of q. It is not necessary to optimize this geometry as the effects are not considered in the proposed methodology. In Table 3.3 the limits of each parameter are summarized for the study presented in the results chapter. During the calculations, geometry checks are performed to avoid overlapping of the tooth geometry. The number of slots per pole per phase q is also used to limit the coil span.
For optimization, the genetic algorithm from Matlab is used to find the maximum efficiency. The DC supply voltage is limited to a maximum of $600\,\mathrm{V}$. Since the optimization uses a Maximum Torque per Ampere (MTPA) approach, the constraint does not accept an operating point in the field weakening range of the machine. The associated maximum current results from the power demand.

Table 3.3: Optimization parameter range

Parameter	Unit	Lower limit	Upper limit
q	-	1	4
y	-	0	q
w_c	-	3	20
b_1	mm	1.5	3
b_t	mm	1.5	10
h_4	mm	r_S	$1.5 \cdot r_\mathrm{S}$
δ_mech	mm	0.5	3.5
l_Fe	mm	2.5	l_cr

Furthermore, the cooling surface of the stator must be larger than the required surface when

$$\pi d_\mathrm{O,S} l_\mathrm{Fe} > \frac{P_\mathrm{all}}{3000\,\frac{\mathrm{W}}{\mathrm{m^2K}} \cdot 15\,\mathrm{K}}. \tag{3.100}$$

Here P_all describes all losses of the machine and $d_\mathrm{O,S}$ is the outer diameter of the stator. This boundary condition has proven to keep the stator and rotor temperatures in an acceptable range. It reduces computation time and prevents unrealistic results that would exceed the temperature limits. The assumption determines a surface area needed to dissipate the machine losses with an assumed heat transfer coefficient of $3000\,\mathrm{W\,m^{-2}\,K^{-1}}$ and a temperature difference of $15\,\mathrm{K}$. In addition, the average tooth flux density is limited to $1.2\,\mathrm{T}$. After determining the optimal stator geometry and winding configuration for the application, the thermal performance of the machine is evaluated. To do this, the FEA for the machine is set up and solved. The temperatures from the static solution are fed back into the electromagnetic model to determine the actual new operating point as a function of the magnet temperature T_M and the temperature dependent losses. This loop is continued until the temperature changes are less than $0.5\,\mathrm{K}$.

Chapter 4

Reference Machine for an Electric Compressor

This chapter provides a design summary of the electric compressor prototype. The electric compressor is designed for a fuel cell application. The modeling approach from Chapter 3 is validated in Chapter 5 with the machine design presented in this chapter. Therefore, the design is briefly summarized. The bearing design and the compressor design are not part of this work. Only the basic information is given for these components.

4.1 Requirements

The electric compressor is to be used in a fuel cell application. The geometric constraints and requirements given by the provided aerodynamic components are summarized in Table 4.1. The provided compressor wheel has an outer diameter of $d_2 = 70\,\text{mm}$ and a continuous power requirement P_C of $25\,\text{kW}$ at $140\,000\,\text{min}^{-1}$. The ratio of the inlet diameter to the outlet diameter is $\frac{d_1}{d_2} = 0.6$. A turbine wheel is attached to the other end of the shaft to recover energy in the fuel cell exhaust gas stream. However, the machine should be able to run at nominal power P_C without the turbine. The provided turbine wheel has an outer diameter of $d_3 = 47\,\text{mm}$ and a length of $l_\text{TW} = 47.5\,\text{mm}$. These requirements give a nominal torque of $T_\text{EM} = 1.71\,\text{N m}$. The power and torque requirements of the compressor are shown in Fig. 4.1. The black lines indicate the operating range of the compressor. The operating point of the compressor is given by

Table 4.1: Geometric data of compressor and turbine

Parameter	Symbol	Unit	Value
Volume flow	$\dot{V}_{\text{corr}}$	$\text{m}^3\,\text{s}^{-1}$	0.12
Compressor pressure ratio	$\Pi_{\text{C,t-t}}$	-	3.4
Turbine pressure ratio	Π_{TW}	-	2.9
Compressor inlet diameter	d_1	mm	42
Compressor outlet diameter	d_2	mm	70
Turbine diameter	d_3	mm	47
Compressor wheel length	l_{CW}	mm	54
Turbine wheel length	l_{TW}	mm	47.5
Shaft speed	n	min^{-1}	140 000

$\dot{V}_{\text{corr}} = 0.12\,\text{m}^3\,\text{s}^{-1}$ and $\Pi_{\text{C,t-t}} = 3.4$. This defines the speed and torque required by the machine without energy recovery from the turbine. The operating point also defines the maximum speed n_{max}. In addition, the lines of constant torque are added to the figure in blue. Thus, the line of constant power and the line of constant torque will cross at the nominal operating point. Therefore, the rated operating range of the machine is the speed line on the left side towards the surge line and on the right side limited by the rated torque. Note that the speed limit is a hard limit that usually cannot be exceeded. The torque limit on the other hand can most likely be exceeded if the thermal limits are not reached with the rated current. In general, this effect can be seen in all compressor maps and must be kept in mind when discussing the performance of electric compressors.

4.2 Design Overview

With the given turbomachinery requirements, the design of the electric machine was carried out. The power electronics was predetermined and gave additional constraints of $i_{\text{RMS}} = 55\,\text{A}$. V_{DC} was chosen to be $750\,\text{V}$. All geometric parameters are summarized in Table 4.2. Due to the high mechanical speeds, the number of pole pairs p was selected to be one in order to keep the electric frequency f as low as possible and thus to keep the frequency dependent losses low. The cross-section of the machine is shown in Fig. 4.3 (a). The active part of the rotor consists of a cylindrical magnet made of Sm_2Co_{17} with diametral magnetization.

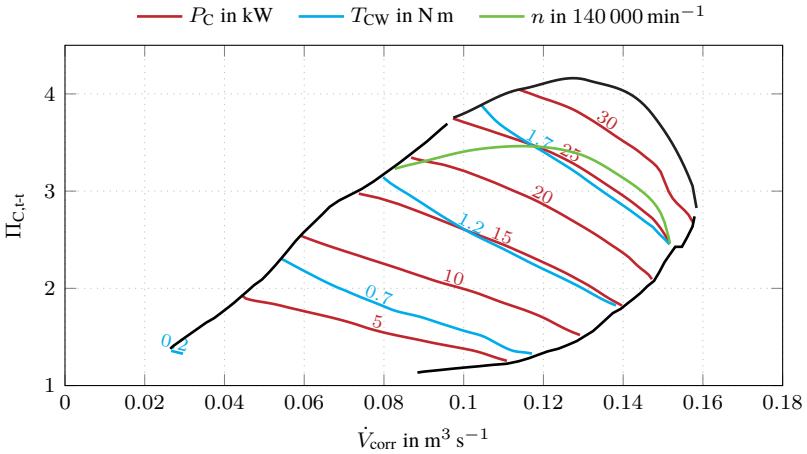

Figure 4.1: Compressor map showing lines of constant power and torque requirement for the compressor.

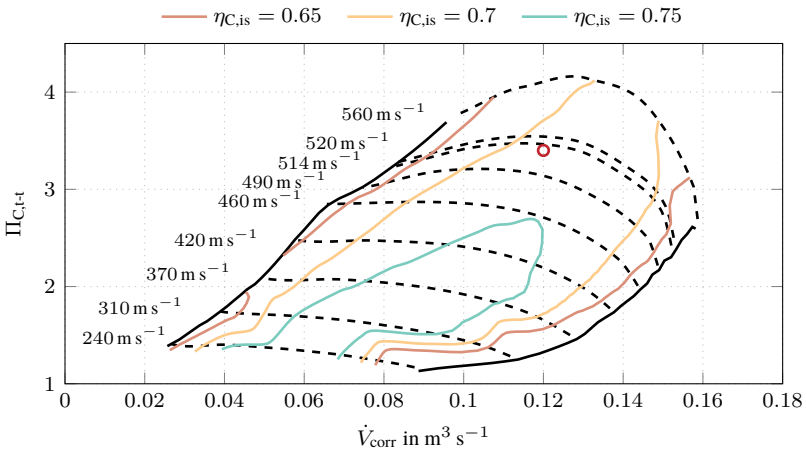

Figure 4.2: Compressor map showing lines of constant corrected circumferential speed and constant isentropic efficiency.

This makes the air gap field sinusoidal. The magnet material has a remanence flux density B_R of $1.11\,\mathrm{T}$ and a coercive field strength H_c of $-834.5\,\mathrm{kA}$. To prevent the magnet from bursting, a metal sleeve made of Inconel 718 is fitted around the magnet to compress it. The outer radius of the rotor $r_\mathrm{S} = 15\,\mathrm{mm}$ and the thickness of the sleeve $t_\mathrm{S} = 3.4\,\mathrm{mm}$. The magnet radius $r_\mathrm{M} = 11.6\,\mathrm{mm}$ and the stator bore radius $r_\mathrm{B} = 17.3\,\mathrm{mm}$. Thus, mechanical air gap δ_mech remains at $2.3\,\mathrm{mm}$ and the magnetic air gap δ has a length of $5.7\,\mathrm{mm}$. The stator design space was limited because the outer diameter $d_\mathrm{O,S}$ was given with a diameter of $105\,\mathrm{mm}$. The machine has 18 slots with a two-layer distributed winding and $q = 3$. The coil span y of the stator winding is chosen to be 8 to reduce the harmonics in the air gap field and to reduce the rotor losses. Further details of the slot geometry are given in Table 4.2.

Table 4.2: Geometric data of the machine

Parameter	Symbol	Unit	Value
Slot opening width	b_1	mm	1.9
Stator teeth width	b_2	mm	3
Stator slot height	h_1	mm	21.4
Number of phases	m	-	3
Turns per coil	w_c	-	11
Parallel strands	a	-	2
Wire diameter	d_Cu	mm	0.511

In addition to the data presented, a scaled cross section of the machine is shown in Fig. 4.3 (a). The winding configuration is color coded. In Fig. 4.3 (b) the details of the slot dimension are shown and the symbols for each dimension are inscribed on the drawing. The machine has water jacket cooling. It is designed to operate with a volume flow of $10\,\mathrm{dm^3\,min^{-1}}$ and a maximum inlet temperature of $60\,^\circ\mathrm{C}$. The machine can be additionally cooled, if necessary, with a ventilation air flow from the compressor. In addition to the losses of the electric machine, the compressor and the bearing system give a significant heat input into the system.

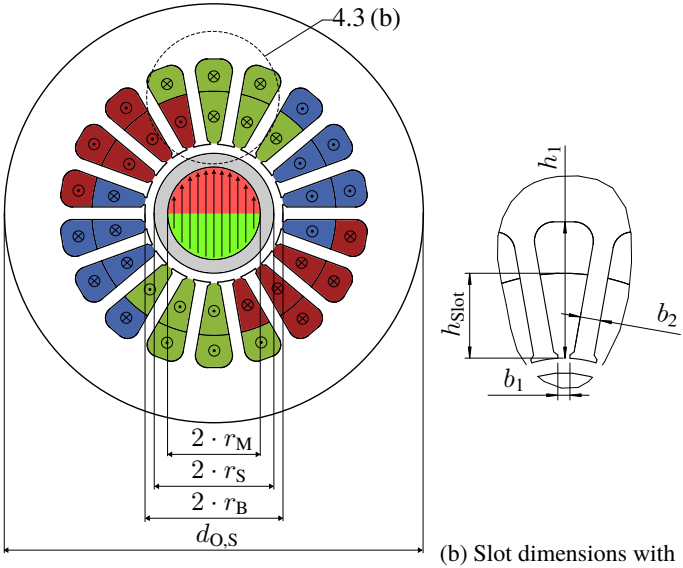

(a) Stator and rotor cross section.

(b) Slot dimensions with parallel stator teeth

Figure 4.3: Machine parameters and dimensions. Color-coded distribution of the two-layer stator winding including the symbolic representation of the magnetomotive force. The rotor is shown with the diametral magnetization of the magnet.

Chapter 5

Validation

The main focus of the validation process is to validate the methodology used and ensure its applicability to similar electric machines, rather than focusing on a specific machine. To achieve this, the reference machine presented in Chapter 4 is used to evaluate the performance of the methodology and to identify potential areas for improvement. Since this machine was designed without the use of the presented methodology, it serves as an independent basis for validation. This approach ensures that the methodology is robust and accurate.

5.1 Validation Process

Different approaches are used to validate each aspect of the methodology. Mainly, numerical simulation is used to validate each aspect. Therefore, all the simulations performed are based on the tools provided by ANSYS.

5.2 Aerodynamic Components

The method of scaling the compressor stage has already been presented and validated in [114, 115]. The turbine wheel sizing is compared with the actual selection for the reference machine. The scaling approach gives the turbine wheel outer diameter $d_3 = 42\,\text{mm}$. The actual selection for the wheel is $47\,\text{mm}$. Since the efficiency measurements of the turbine wheel could not be included in this work, the scaling must be assumed to be an optimistic approach.

5.3 Mechanical Validation

The mechanical design is divided into two parts. First, the analytical design of the sleeve and magnet is compared to the two-dimensional FEA. Then, the natural frequency of the simplified rotor is compared to the results of the rotor design of the reference machine.

5.3.1 Rotor Strength

To validate the accuracy of the analytic calculation, the results obtained for all six load steps are compared. The material properties used in both calculations are identical and are shown in Table 5.1. The stress values are compared only at the critical locations, the center of the magnet and the inner diameter of the sleeve. The results presented in Table 5.2 show the results for the minimum required

Table 5.1: Material Properties of Inconel 718 and Sm5Co17

Material in	ρ $\mathrm{kg\,m^{-3}}$	E GPa	ν -	α $\mathrm{\mu m\,m^{-1}\,K^{-1}}$	σ_{YS} MPa
Inconel 718	8221	203	0.296	13.1	1090
Sm_2Co_{17}	8300	120	0.270	11	40

radial overlap of $47\,\mu m$. These analytic results are compared with the 2D FEA results shown in Table 5.3. It can be observed that the maximum stress in the magnet σ_M and the joint σ_J is calculated with high accuracy, with deviations in the range of $0.1\,MPa$. Although the deviations for the maximum sleeve stresses σ_S are marginally larger, especially when considering the rotation of the shaft, the maximum deviation is only $3.2\,MPa$, which is a relative deviation of $0.4\,\%$. This level of accuracy is sufficient.
To verify that the deviations are not due to an inaccurate approach, the component stresses given by the equations eq. (3.30) and eq. (3.35) for the magnet and sleeve under rotation are compared with the results obtained from the FEA. The stresses across the magnet radius are shown in Figs. 5.1 (a) and 5.1 (b). It can be seen that the maximum stress of the magnet is located in the center of the component, where the tangential stress and radial stress are equal to $104\,MPa$, since a sleeve does not support the magnet. For the sleeve, the tangential stresses have their maximum value of $391\,MPa$ at the inner diameter of the bore, while

Table 5.2: Analytic calculation for minimum overlap required to satisfy all stress limits.

Case	in	1	2	3	4	5	6
T_M	°C	20	200	20	200	20	200
n	min^{-1}	0	0	144 200	144 200	173 040	173 040
σ_S	MPa	680.9	617.5	813.5	750.0	871.8	808.4
σ_M	MPa	-149.4	-135.5	11.6	25.5	82.5	96.4
σ_J	MPa	149.4	135.5	92.5	78.6	67.4	53.5

Table 5.3: FEA calculation for minimum overlap required to satisfy all stress limits.

Case	in	1	2	3	4	5	6
T_M	°C	20	200	20	200	20	200
n	min^{-1}	0	0	144 200	144 200	173 040	173 040
σ_S	MPa	681.2	617.8	810.3	747.1	868.8	805.8
σ_M	MPa	-149.4	-135.5	11.5	25.5	82.4	96.3
σ_J	MPa	149.4	135.5	92.6	78.6	67.5	53.6

the radial stresses have a maximum value of less than 10 MPa. It can be seen that both approaches are in good agreement with the FEA results. Therefore, it is concluded that the deviations shown in Table 5.3 are not due to the calculation of the stress caused by the rotation. Further investigations have shown that a stepwise FEA simulation, where the simulations are divided into the three loading steps, rotation, thermal expansion and interference fit, where the magnet is replaced by an internal pressure, leads to a better agreement. It is suggested that the small deviations are due to the interaction between the inner and outer components. Therefore, it is concluded that the models used are correct, and they can be applied in this case.

5.3.2 Modal Analysis

To validate the eigenfrequency, a simplified geometry is created based on the geometry presented in Section 3.1.4, using the same material selection as the reference machine. A direct comparison of the two rotors is shown in Section 5.3.2,

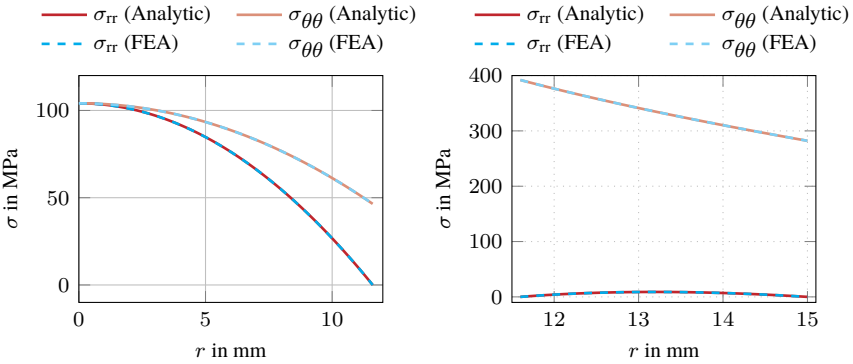

(a) Magnet stress across the magnet radius, from 0 mm to 11.6 mm.

(b) Sleeve stress across the sleeve radius, from 11.6 mm to 15 mm.

Figure 5.1: Comparison of rotational effects on part stresses at the maximum speed $n_{\text{max}} = 144\,200\,\text{min}^{-1}$

representing the first bending mode. The frequency of the first bending mode for the reference machine is 2820 Hz, while the simplified shaft has a first bending frequency of 2855 Hz. This results in an absolute deviation of 35 Hz, which corresponds to a relative deviation of 1.24 %. The absolute scale of the deformation is not shown because the values are not representative of the deformation, only the mode and frequency are of interest. The stationary points for the first bending eigenmode are at the same positions on the rotor.

5.4 Magnetic

The magnetic validation consists of three major parts. Firstly, it includes the validation of the air gap flux density, which consists of the rotor field, permeance functions, and the resulting air gap field. The second part comprises the validation of the flux linkages, which includes the leakage flux. Lastly, the results of the analytic loss calculation are compared to the FEA results.

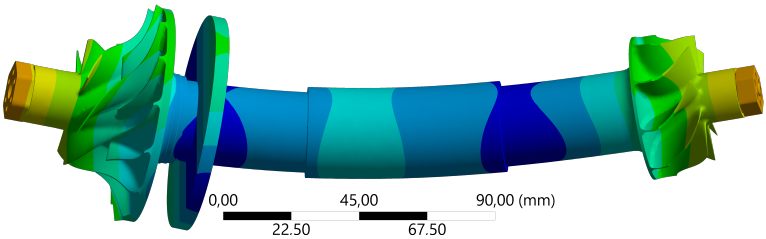

(a) Reference shaft ($f = 2820\,\mathrm{Hz}$)

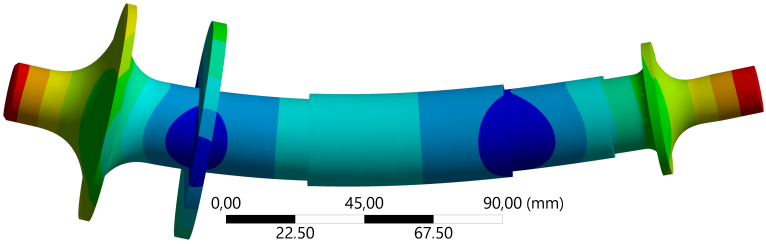

(b) Simplified shaft ($f = 2855\,\mathrm{Hz}$)

Figure 5.2: First bending eigenfrequency of the shaft of the reference machine (a) and of the simplified shaft (b) without scale. Blue region indicates the stationary point for the first bending eigenfrequency.

5.4.1 Air Gap Flux Density

As shown in Section 3.2, the air gap flux density is a result of the superposition of the rotor and stator fields. Since the air gap flux density is affected by the stator slotting, it is included in the modeling and also shown in the validation. The stator field itself is not part of the validation as it is state of the art and is included in the superposition of the air gap field. For the rotor field, the NN predicts the flux amplitude of the magnet. Therefore, Fig. 5.3 (a) shows the predicted air gap flux density at the center of the air gap for variations in magnet height and magnetic air gap length. Furthermore, in Fig. 5.3 (b) the magnetic flux amplitude over the machine radius is plotted for the air gap. It can be seen that the flux density decreases along the radius. Without flux leakage, a linear decrease would be expected since the air gap cross-section increases with r. The slope of the

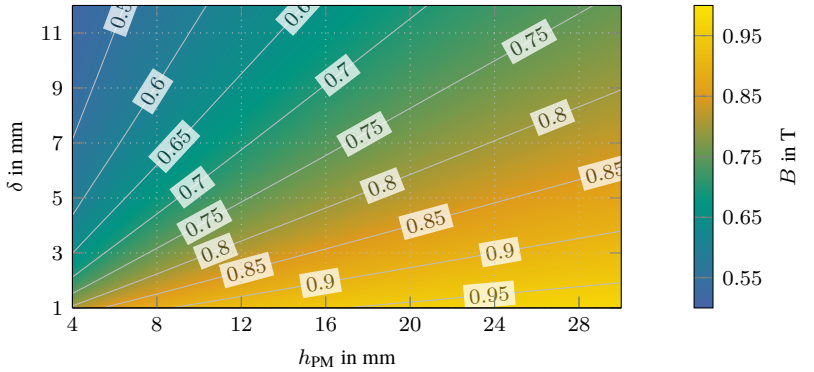

(a) Neuronal net fitted to the results from the static FEA; Shown in the center of the air gap.

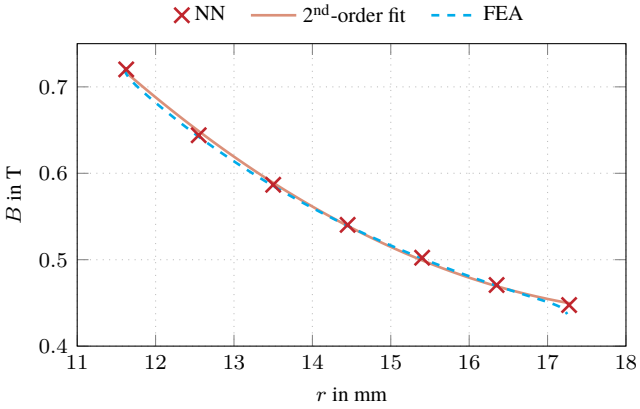

(b) Amplitude of the radial flux density shown over the radius of the air gap.

Figure 5.3: Results of the used NN to predict air gap flux densities over a wide variety of geometries and air gap length combinations.

curve decreases, indicating leakage flux from the magnet. The NN can accurately predict the course of the air gap flux density. A 2$^{\text{nd}}$ order fit is sufficient to provide accurate results at any position of the air gap.
The next step is to show the assumption of an ideal sinusoidal air gap field. Therefore, a Fast Fourier Transformation (FFT) of the air gap field resulting from the 2D-FEA is performed. All harmonics with a normalized amplitude less than 1×10^{-5} are set to 0. This leaves only the 1$^{\text{st}}$ order with an amplitude of $0.54\,\text{T}$. From this it can be concluded that the assumption of an ideal sinusoidal air gap is correct. The rotor field is followed by the slotting influence. Since the NNs predict the permeance functions at seven locations in the air gap, the first step is to validate the permeance functions at these locations. Therefore, in Fig. 5.4 the permeance functions for four of the seven locations are shown. The positions directly at the stator and rotor are of minor importance. It is not shown because of the large increase in the permeance function that can be seen later in Fig. 5.5. Several observations are made in Fig. 5.4. The NNs are able to predict accurately the permeance function at all positions. Especially for the positions with a significant drop in Λ, such as $\frac{5}{6}\delta$ and $\frac{2}{3}\delta$, the NNs fit the remanence function very well. Since the field is not needed only at the specified locations where the NNs work, an interpolation is used to have a continuous solution of the permeance function.
The result of the continuous solution is shown in Fig. 5.5 as a contour plot for a slot segment. This plot shows the contour of the slot opening and the surface of the sleeve. Isolines are also plotted to understand the radial progression of the permeance function. It is observed that the field in the center of the slot, close to the stator, has its minimum at $\Lambda < 0.6$. At the edges of the stator teeth a peak of Λ is observed with values above $\Lambda > 1.5$. It can also be seen that Λ increases rapidly in the negative direction along the y-axis. Towards the surface of the sleeve, Λ reaches 0.98. Therefore, it is observed that the sleeve surface is in an area with minimal influence of the stator slot. On the sides of the segment, Λ remains above one. In these regions, the neighboring slots interfere with each other. The detailed understanding of the local permanence function $\Lambda(r,\varphi)$ is important because the exact amplitude of the flux harmonics at any given position must be known to accurately determine the eddy current losses in the sleeve or magnet. In Fig. 5.6 the interpolated permeance function is compared with the actual FEA result. Compared to the previously presented results, the deviations appear larger. In particular, in the center of the slit opening, the deviation appears to be significant, but the relative deviation is only $0.6\,\%$.
Since all subcomponents of the air gap field are validated, the resulting air gap field can be compared. This is done in two steps. First, the rotor field including

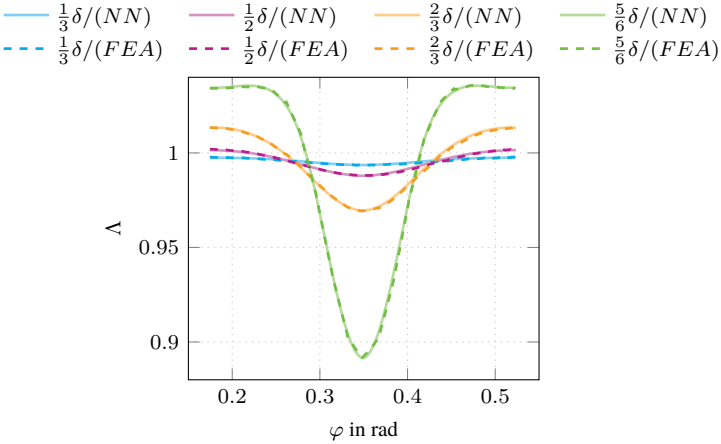

Figure 5.4: Comparison of the presented approach with the FEA permeance function for the designed motor at the defined spots from 1/3 to 5/6 of the gap.

the slotting effect is compared to the original 2D-FEA result. The original core material NO20 with a non-linear BH curve is used for the comparison. In addition, the stator has its original slot geometry. The resulting air gap flux density is shown in Fig. 5.7 (a). From a visual inspection of the lines, no significant deviations can be observed. To show more details of the comparison, the results of the FFT of the two flux densities are shown in Table 5.4(a). Only results with an amplitude greater than 1 mT are integrated. It can be seen that the deviations in the first amplitude are minimal and result in a relative deviation of 2.3 %. The relative deviation for the 19^{th} harmonic is larger with 17 %, while the absolute error is relatively small and could be due to numerical uncertainty.
In Fig. 5.7 (b) the stator field is added with the nominal operating point. The deviations remain small and decrease for the first amplitude. More details are shown in Table 5.4(b). The different harmonics show deviations in all cases. However, all harmonics are in the same order of magnitude. The deviations are expected due to the simplification of a plane stator field, which does not take into account the special requirements of HSPMSM. In addition, the superposition of the stator and rotor field can lead to inaccuracies. The upcoming validation of the machine parameters and losses will prove that the stator field calculation is sufficient for the use case.

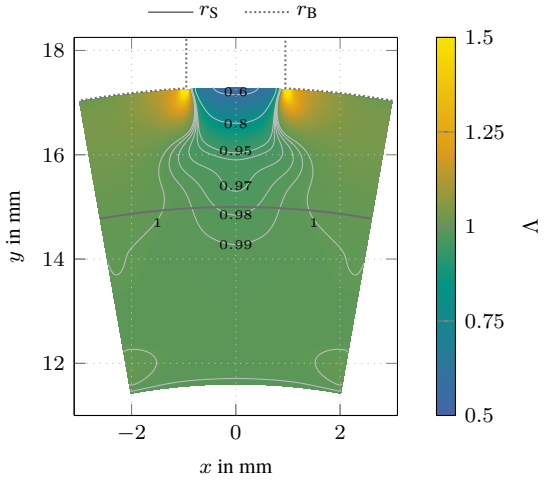

Figure 5.5: Permeance function for the reference machine. For one air gap segment over one stator slot.

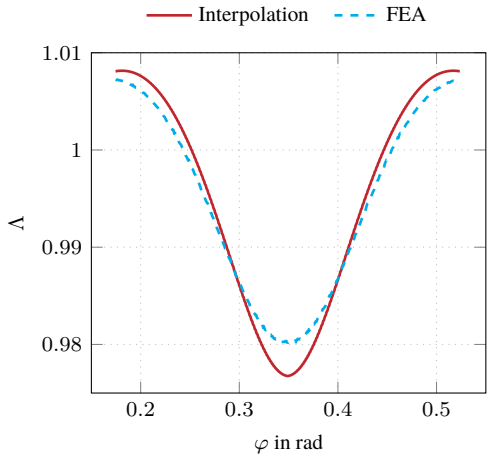

Figure 5.6: Comparison of the interpolated permeance function at the sleeve surface r_S.

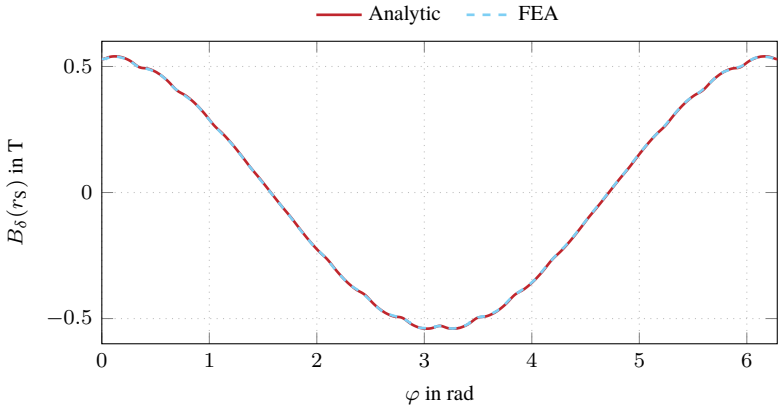

(a) $i = 0\,\mathrm{A}$

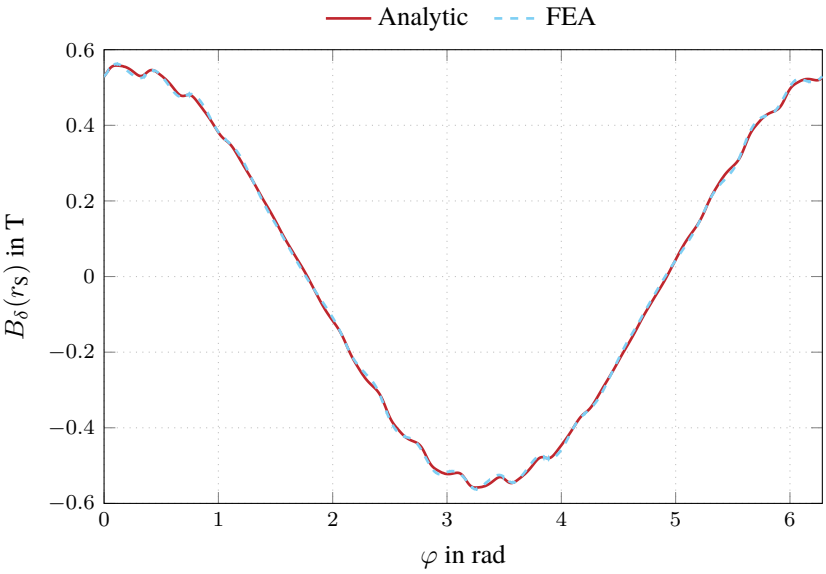

(b) $i = i_{\mathrm{nom}} = 36.4\,\mathrm{A}$

Figure 5.7: Air gap flux density at the sleeve surface r_S for the no load case (a) and nominal operating point (b).

Table 5.4: Air gap field harmonics comparison for no load operating and nominal operating points.

(a) $i = 0\,\mathrm{A}$

Order	in	NN	FEA
1^{st}	T	0.5509	0.5383
5^{th}	T	-	-
7^{th}	T	-	-
11^{th}	T	-	-
13^{th}	T	-	-
17^{th}	T	0.0040	0.0041
19^{th}	T	0.0040	0.0034

(b) $i = 36.4\,\mathrm{A}$

Order	in	NN	FEA
1^{st}	T	0.5509	0.5502
5^{th}	T	0.0033	0.0091
7^{th}	T	0.0010	0.0029
11^{th}	T	0.0006	0.0016
13^{th}	T	0.0011	0.0028
17^{th}	T	0.0063	0.0112
19^{th}	T	0.0070	0.0069

5.4.2 Flux Linkages

From the air gap flux density, the main flux linkages and the main inductances are derived. In the presented model only the main flux linkage and therefore the main inductance $L_{\mathrm{q,main}}$ are calculated in the first step. In addition, the leakage inductance L_σ and the winding head inductance L_{wh} are added. The combination of the results is shown in Table 5.5. The model results are compared with FEA and the results of the LCR measurement of the assembled machine. It is observed that the total inductance L agrees very well with an absolute deviation of $2.2\,\mu\mathrm{H}$ and a relative deviation less than $1\,\%$. It should be noted that this comparison is only valid because of the linear characteristics of the machine as a whole.

Table 5.5: Machine inductances divided into its subcomponents

Parameter	in	Model	FEA	Measurement
$L_{\mathrm{q,main}}$	µH	94.5	-	-
L_σ	µH	103.9	-	-
$L_{\mathrm{q,main}} + L_\sigma$	µH	198.4	196.2	-
L_{wh}	µH	123.9	-	-
$\sum L$	µH	322.3	320.1	315.0

The model gives a permanent flux linkage of $0.0241\,\mathrm{V\,s}$ at room temperature. This can be compared to the measurement made with two machines. Therefore, the rotor was rotated with a hand drill up to $1100\,\mathrm{min}^{-1}$ and the induced voltage was measured with an oscilloscope. The measurement was made three times for each machine and Ψ_{PM} was calculated from the induced voltages in all three phases. This results in a scatter of the measured values of $0.0239\,\mathrm{V\,s}$ to $0.0242\,\mathrm{V\,s}$. The measurement at this low speed is valid because the machine is linear. The results fit well with the mean remanence flux density given in the data sheet for the magnet material.
The remaining parameter to be validated is the phase resistance. The phase resistance of the machine at room temperature is calculated to be $45\,\mathrm{m\Omega}$. The measurement of the phase resistance is in a range of $0.38\,\mathrm{m\Omega}$ to $0.42\,\mathrm{m\Omega}$. Overall, the deviations are over $10\,\%$. Therefore, the model overpredicts the resistance, which is not critical for the design process.

5.4.3 Machine Losses

The losses can be validated only for the core losses and the eddy current losses occurring in the sleeve. With the two proposed models, the results presented in Table 5.6 are obtained. The core losses of the machine P_{Fe} are calculated with $179.6\,\mathrm{W}$ compared to $168.0\,\mathrm{W}$ in the FEA. This corresponds to a relative deviation of $6.9\,\%$. For the rotor losses, the absolute deviation is only $1.2\,\mathrm{W}$, which is a relative deviation of $7.3\,\%$. Both calculations do not take into account any Pulse Width Modulation (PWM) influence and are most likely higher in reality. Therefore, it is concluded that the losses are accurate enough. The deviations for the core losses are mainly due to the simplified approach of a homogeneous flux density in the teeth and the stator yoke. For the rotor losses, the uncertainty is due to the uncertainty in the prediction of the harmonics and the fact that the effects of the eddy currents in the rotor on the field are not considered.

Table 5.6: Comparison of losses determined by the presented model and the FEA.

Loss	in	Model	FEA
P_{Fe}	W	179.6	168.0
P_{Rotor}	W	15.2	16.4

Chapter 6

Design Study for Fuel Cell Electric Air Compressors

In this chapter, the methodology presented and validated in the previous chapters is applied to the specific application of electric air compressors for fuel cell applications. For this purpose, the objectives, and the boundaries are defined. Different parameter studies are performed, and the results are presented to understand the influence of the design variables. A first study is carried out on the design of the sleeve and is presented in Section 6.2. This is followed in Section 6.3 by the system optimization for an electric compressor in the design space specified in Section 6.1.1.

6.1 Objectives and Boundary Conditions

The main purpose of the presented results is to get a good understanding of the electric drive system and how rotor materials affect the performance. It is also shown how the circumferential speed of the rotor impacts the machine design and what design speed should be used for different applications.

6.1.1 Range of Application

In the opening literature review of this work in Table 1.2 it is seen that the pressure of a PEM fuel cell operating range goes from 1.6 bar to 3.5 bar. The electric compressor, reaching the maximum pressure ratio of 3.5 bar, is described in [39]

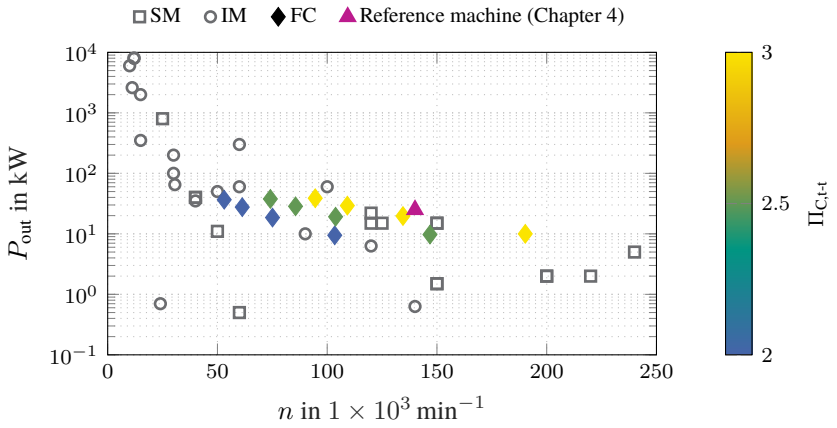

Figure 6.1: Fuel cell compressors operating range based on an aerodynamic scaling in comparison to the published high-speed electric machines.

and is designed as a two-stage compressor. In this study only single-stage compressors are investigated. The fuel cell supplier *EKPO Fuel Cell Technologies GmbH* offers a maximum stack capacity of 205 kW electrical power at an absolute pressure of 2.5 bar [151]. The largest complete systems currently available are in the 120 kW to 150 kW range. [152, 153]. For these sizes of fuel cell systems, an air compressor shaft power of 25 kW is expected. The focus of this work is on existing systems and increasing power requirements for potential larger systems. The combination of compressor power and pressure ratio defines the volume flow delivered to the fuel cell. Starting from the given compressor stage, the scaling of the aerodynamic components determines the speed and power range of the machines. The use of a turbine reduces the power requirement of the machine.

In Fig. 6.1 the results of the aerodynamic component scaling are shown in relation to the published literature for high-speed electric machines. The results show the total compressor power consumption as a function of speed. A turbine will shift the operating points to a lower power level at the same speed. As input parameters, a target compressor power range of 10 kW to 40 kW and a pressure ratio $\Pi_{C,t\text{-}t}$ of 2 to 3 are used. This results in a wide range of compressor stage designs and therefore a wide speed range. The compressor power does not al-

ways match the required power because the required flow is calculated with an estimated compressor stage efficiency $\eta_{C,is}$ of 0.75. Therefore, the power requirement varies and is usually lower for smaller pressure ratios $\Pi_{C,t\text{-}t}$. It can be observed that the speed decreases with increasing compressor power. This is simply explained by the larger cross section required and therefore larger wheel diameters, which reduces the rotational speed at constant circumferential speed. It can also be seen that the application range for pressure ratios $\Pi_{C,t\text{-}t}$ of 2 to 3 is in a range where machine designs have already been published. Reducing the power and increasing the speed leads to a wider spread of the speed range. In particular, high pressure ratios of 3 and higher will be difficult to achieve at lower power ratings. It is important to note that different compressor characteristics lead to different results. To increase the efficiency of the overall system, turbines are added to the system to recover energy from the airflow leaving the fuel cell. The temperature of the air stream is assumed to be $T_{air} = 80\,°C$ and the pressure drop is $\Delta p = 0.5$ bar. In Fig. 6.2 (a) the turbine power P_T is plotted over the speed range of the applications. It can be seen that higher pressure results in higher turbine power. In Fig. 6.2 (b) the power of the turbine is put in relation to the power of the compressor. It is observed that the turbine has the potential to recover up to $40\,\%$ of the energy put into the air supply. A higher pressure therefore leads to a higher recovered power. The step from a pressure ratio of 2 to a pressure ratio of 2.5 gives an improvement in efficiency. Increasing the pressure ratio further decreases the efficiency again. These values agree with those published by [112], who gives efficiencies of up to $40\,\%$.

6.2 Rotor Sleeve Design

The mechanical stability of the rotor assembly is primarily provided by the sleeve, which compresses the magnet to prevent it from breaking. The two most common metal materials used in published research are titanium (TiAl6V4) and Inconel 718. In the following study, these two materials are combined with a magnet made of Sm_2Co_{17}. The two main constraints for this study are that the maximum stresses in the magnet and sleeve must not exceed the yield strength of the material and must have a safety factor of 1.2 at the maximum operating speed. It has to be possible to assemble both parts by cooling the magnet and heating the sleeve up to its material-specific limits. The assembly gap to be achieved is taken from DIN 7190 [118]. For this study, the operating range of fuel cell compressors is considered as shown in Fig. 6.1. The speed range varies from $25\,000\,\text{min}^{-1}$ to $195\,000\,\text{min}^{-1}$. This range is divided into $10\,000\,\text{min}^{-1}$ steps

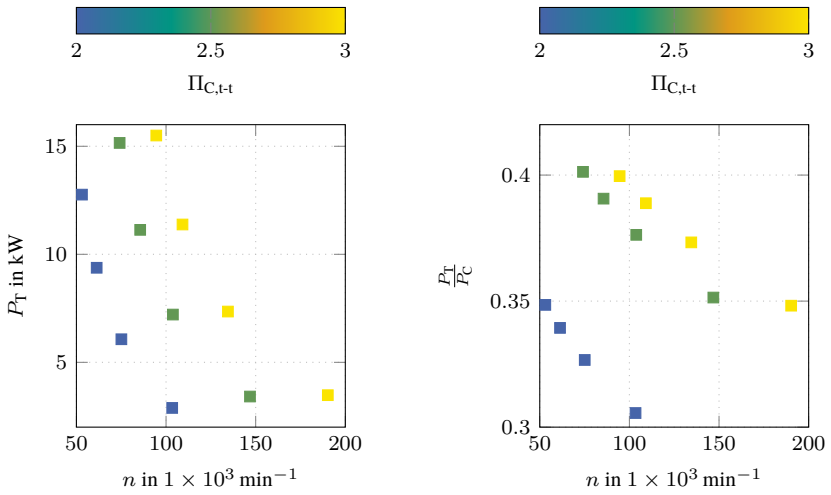

(a) Absolute recovered power

(b) Relative recovered power

Figure 6.2: Recovered energy from the turbine

and combined with a variation of the circumferential speed v_c of $100\,\mathrm{m\,s^{-1}}$ to $260\,\mathrm{m\,s^{-1}}$. The minimum sleeve thickness is set to 1 mm. This limit is given to ensure that the design is feasible for manufacturing. The Fig. 6.3 (a) shows the results for Sm_2Co_{17} and Inconel 718. The sleeve thickness t_S increases with rotational speed and circumferential speed. The absolute sleeve thickness has its maximum at high circumferential speeds and low rotational speeds. In Fig. 6.3 (b) the relative sleeve thickness $\frac{t_S}{r_S}$ is shown. This plot of the data shows that the sleeve thickness is primarily a function of circumferential speed. This behavior is expected because the rotational stresses are proportional to the circumferential speed, as seen in Eqs. (3.28), (3.29), (3.33) and (3.34). This is valid for speeds above $175\,\mathrm{m\,s^{-1}}$. As the speed increases, the relative thickness of the sleeve increases for the same circumferential speed. For speeds below $175\,\mathrm{m\,s^{-1}}$ and speeds above $75\,000\,\mathrm{min^{-1}}$, the minimum sleeve thickness limits the decrease in sleeve thickness. Therefore, at low circumferential speeds and high rotational speeds, the ratio of sleeve thickness to rotor radius is worse than for designs close to the minimum sleeve thickness.

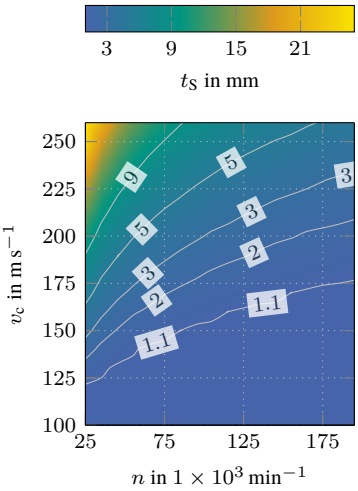

(a) Inconel 718 sleeve thickness t_S in mm

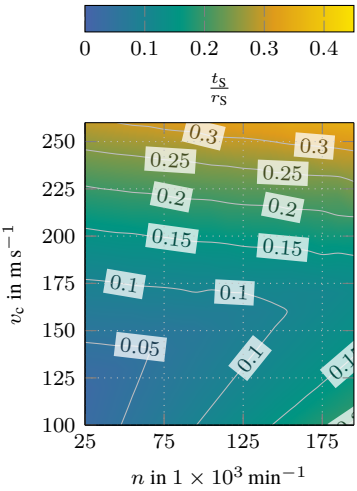

(b) Relative sleeve thickness for Inconel 718

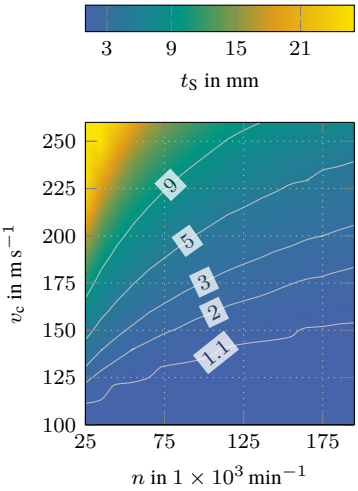

(c) Titanium sleeve thickness t_S in mm

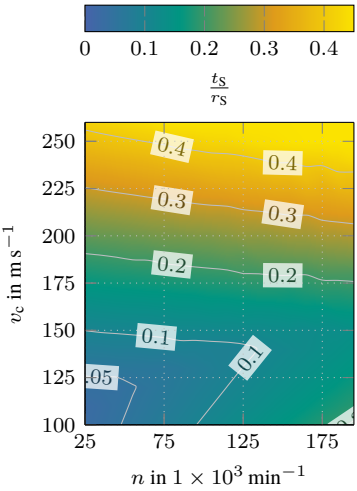

(d) Relative sleeve thickness for titanium

Figure 6.3: Sleeve thickness over circumferential speed and rotational speed for Inconel 718 sleeves in combination with Sm_2Co_{17} magnets

If it is not possible to manufacture such a thin sleeve, this area increases with the sleeve thickness contour line of 2 mm in Fig. 6.3 (a).
Fig. 6.3 (c) shows the sleeve thickness as a function of rotational speed and circumferential speed for a titanium sleeve. The same behavior is observed as for Inconel sleeves, but the design requires a higher sleeve thickness. The reason for the higher sleeve thickness is not the lower yield strength. As shown in Fig. 6.4 (c), the safety factor in the worst case is close to two, even though a safety factor of only 1.2 is required. The reason for the high safety factor and poor material utilization is the required assembly clearance. The assembly gap is shown in Fig. 6.4 (d). In the large blue area, the sleeve thickness is limited by the assembly tolerance, which is at its minimum. In the parts with the larger assembly gap, the design is limited by the minimum sleeve thickness of 1 mm. The yield strength is therefore not a limiting factor for a titanium sleeve. Rather, it is limited by the thermal expansion given by $\alpha = 8.7\,\mu\mathrm{m\,m^{-1}\,K^{-1}}$ to $9.1\,\mu\mathrm{m\,m^{-1}\,K^{-1}}$ and the maximum assembly temperature of $T = 400\,^{\circ}\mathrm{C}$. To ensure that assembly is possible, the sleeve thickness must be increased. The magnet diameter decreases for a constant outer diameter r_{S}. This results in a decreasing elongation under rotation of the sleeve at the inner diameter and a decreasing elongation of the magnet. This results in a smaller required overlap as can be seen from eq. (3.30) and eq. (3.35).
In comparison, the same evaluation is done for the Inconel 718 sleeve in Figs. 6.4 (a) and 6.4 (b). It can be seen that the safety factor of the sleeve is at its lower limit of 1.2 when the circumferential speed reaches $150\,\mathrm{m\,s^{-1}}$. Therefore, the material is much better utilized compared to the titanium sleeve. In Fig. 6.4 (b) it is also seen that the relative assembly gap is much larger compared to the titanium design. There are two reasons for this: First, Inconel 718 has a higher thermal expansion factor, which is in the range of $12.8\,\mu\mathrm{m\,m^{-1}\,K^{-1}}$ to $13.4\,\mu\mathrm{m\,m^{-1}\,K^{-1}}$. Second, the maximum assembly temperature is higher with $600\,^{\circ}\mathrm{C}$. The high assembly temperatures carry the risk of demagnetizing the magnet if it is already magnetized during the assembly process. This should be checked in detail, but is not considered for this study, since the magnets should be magnetized afterwards for easier handling during manufacturing. It is shown that at high-speeds the assembly gap of Inconel 718 sleeves is larger and therefore the risk of failed assemblies is also lower compared to titanium.

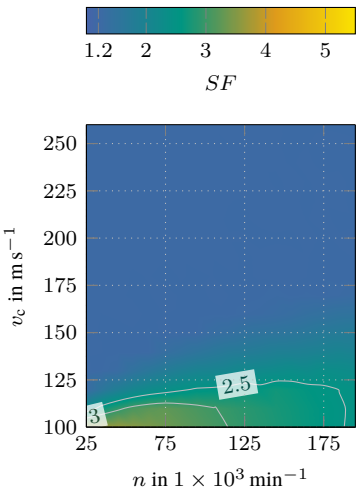

(a) Safety factor for Inconel

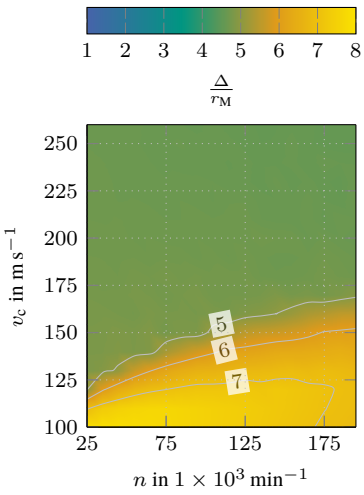

(b) Relative assembly gap Inconel

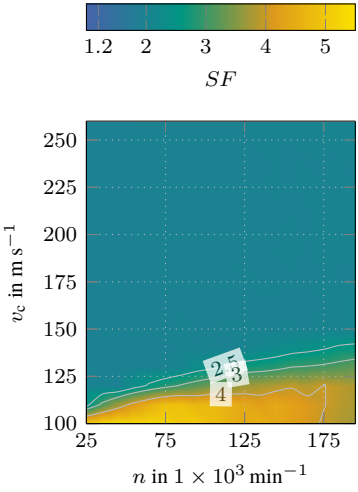

(c) Safety factor for titanium

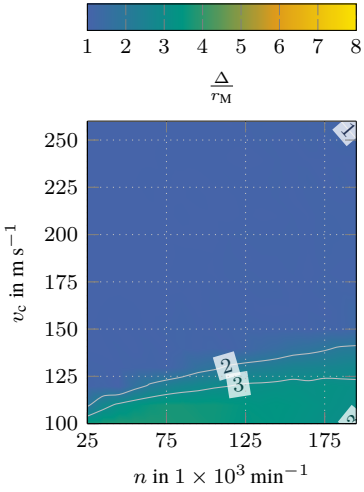

(d) Relative assembly gap for titanium

Figure 6.4: Safety factor and relative assembly gap for an Inconel sleeve (a)-(b) and a titanium sleeve (c)-(d)

6.3 System Optimization

In this section, complete systems are optimized. Therefore, the study is divided into two parts. In the first part a constant circumferential speed of $v_c = 210\,\mathrm{m\,s^{-1}}$ and different loads are considered. In the second part, a specific requirement with a variation of the peripheral speed is examined. This will improve the understanding of the results and their interpretation. Finally, a multiobjective optimization is presented. The efficiency and the volume of the motor are considered.

6.3.1 Constant Circumferential Speed and Variable Loads

In the following section, the focus of the study is the investigation of the load influence on the design. Therefore, the peripheral speed of all machines is constant at $210\,\mathrm{m\,s^{-1}}$. The focus is on finding the limits and understanding the relationships between the load and the limiting parameters.

6.3.1.1 Critical Length

The critical length of the machine is determined by its first bending eigenfrequency, and it is assumed that the drive operates below this frequency. In the proposed design approach, the active length of the machine is the only adjustable parameter affecting the eigenfrequency. Other influencing factors such as material properties, compressor operating speed, and rotor circumferential speed are predefined, while the bearing diameter and length are determined by the maximum allowable circumferential speed and the length-to-diameter ratio and remain unchanged. A shorter active length increases the eigenfrequency and provides a higher safety margin. For the evaluated design space, the ratio of $\frac{l_{\mathrm{Fe}}}{l_{\mathrm{cr}}}$ is studied. As shown in Fig. 6.5, the two previously investigated sleeve materials are compared. In Fig. 6.5 (a) the results are shown for a sleeve made of Inconel 718. The data presented includes designs with only a compressor (C only) and designs with compressor and turbine (C+T). In addition, the data is color coded in terms of the compressor operating pressure ratio $\Pi_{\mathrm{C,t\text{-}t}}$. It can be seen that for the lowest pressure ratio of 2 the length ratio is around 0.2. Moreover, the turbine has no major influence on the length ratio. Increasing the pressure ratio increases the length ratio. For the higher power requirements and lower speeds, which correlate with the lower rotational speeds, the rotor design is still on the safe side with ratios of 0.6 to 0.9. Designs with a pressure ratio of 3 and above reach their critical length. For a pressure ratio of 3.5, this limit is reached for all design

powers at the specified circumferential speed. A design for 10 kW is excluded from this summary because of rotational speeds of 250 000 min^{-1}. Increasing the circumferential speed above 210 $\mathrm{m\,s}^{-1}$ opens up the potential for generating suitable designs, since the bending eigenfrequency increases with higher circumferential speeds. The influence of circumferential speed will be shown in the next section. In Fig. 6.5 (b) the results for a titanium sleeve are shown. The pattern

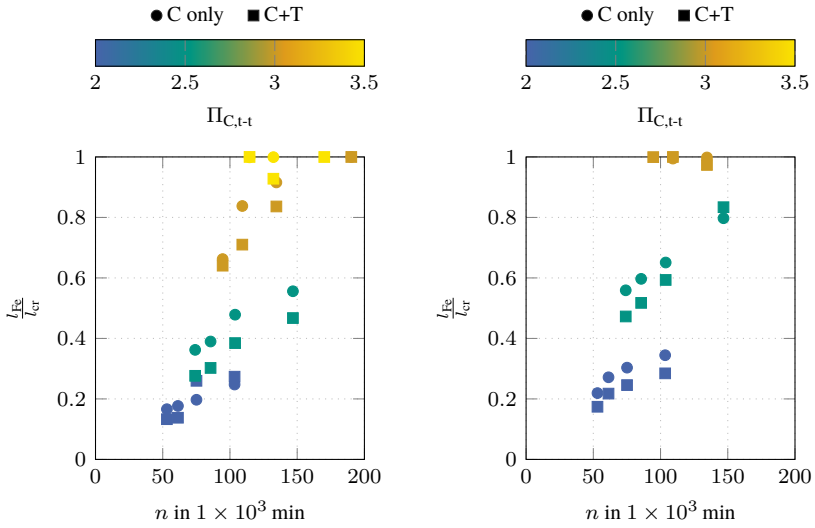

(a) Inconel 718

(b) Titanium

Figure 6.5: Required active length l_{Fe} in relation to the critical length l_{cr}. Comparison of the shaft material (a) Inconel and (b) Titanium at a constant circumferential speed $v_{\mathrm{c}} = 210\,\mathrm{m\,s}^{-1}$. Comparison of compressor only (C only) and compressor and turbine (C+T) designs.

can be compared with the results for the Inconel sleeve. It can be observed that the required length ratio is higher. For the design point at 150 000 min^{-1} and $\Pi_{\mathrm{C,t\text{-}t}} = 2.5$ an increase of 30 % is observed. Especially in the designs for a pressure ratio of $\Pi_{\mathrm{C,t\text{-}t}} = 3$ and higher, the limitation of the titanium material is observed. For the whole range of machine designs the maximum length ratio is used. From these results it can be concluded that Inconel 718 is more suitable for

high speeds and higher power requirements due to the smaller length ratios compared to titanium and therefore the potential for a longer active machine length.

6.3.1.2 Magnetic Rotor Performance

In the next section, the focus shifts from sleeve design to magnetic design. The sleeve design itself has a significant impact on the overall magnetic performance as it increases the air gap length and therefore the utilization of the magnet. The comparison shown in Fig. 6.6 assumes a constant circumferential speed v_c of $210\,\mathrm{m\,s^{-1}}$. The comparison is divided into the two sleeve materials under consideration. In Fig. 6.6 (a) the sleeve thickness of the different designs is shown. The required sleeve thickness for Inconel is smaller compared to Titanium. At high speeds the overall design process did not find a solution for the titanium rotor as there is no data point at $190\,000\,\mathrm{min^{-1}}$. The absolute difference in thickness remains constant, which correlates with the results shown earlier. In Fig. 6.6 (b) the mechanical air gap of the machine is shown. The machine optimization does not decrease with the speed. Instead, the fit to the data points shows an optimum for both sleeve materials. Starting at low speeds, the sleeve thicknesses of both materials are close to each other. For titanium, the mechanical air gap length then decreases at higher speeds. For the Inconel sleeve, the air gap length increases up to a speed of $100\,000\,\mathrm{min^{-1}}$ and then decreases. The fit for the titanium sleeve shows that the expected air gap length would be less than $0\,\mathrm{mm}$. Therefore, it is clear that the machine design is not possible, considering that the results in Fig. 6.5 (b) indicate that the critical length is already at its maximum for the high speeds.
The sum of the two previously described results is the magnetic air gap length, which describes the magnetic performance of the machine. Therefore, the results in Fig. 6.6 (c) show a linear decrease of the magnetic air gap δ as the speed increases. This means that the optimal ratio of magnetic air gap length to magnet radius remains constant. The optimal design therefore still depends on the chosen sleeve material, since the conductivity of the material contributes to the rotor losses. It can be seen that the two materials have an identical air gap length at $130\,000\,\mathrm{min^{-1}}$ to $140\,000\,\mathrm{min^{-1}}$. Looking at eq. (3.56) it can be noted that the optimal air gap flux density is constant in the presented results, considering the ratio of $\frac{\delta}{h_{\mathrm{PM}}}$ to be constant. This can be seen in Fig. 6.7. For titanium this trend is observed over the entire range studied. For Inconel the flux density decreases on the left side for lower speeds. When $100\,000\,\mathrm{min^{-1}}$ is reached, the flux density remains constant up to the maximum speeds studied. It is evident

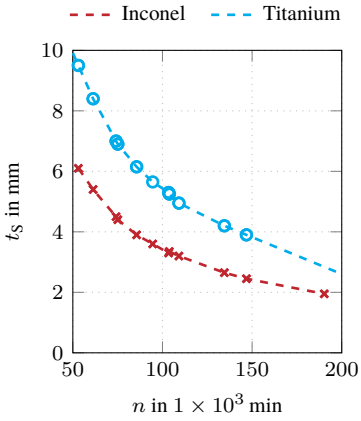

(a) Sleeve thickness

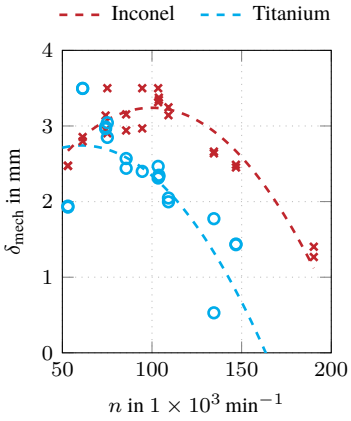

(b) Air gap length δ_{mech}

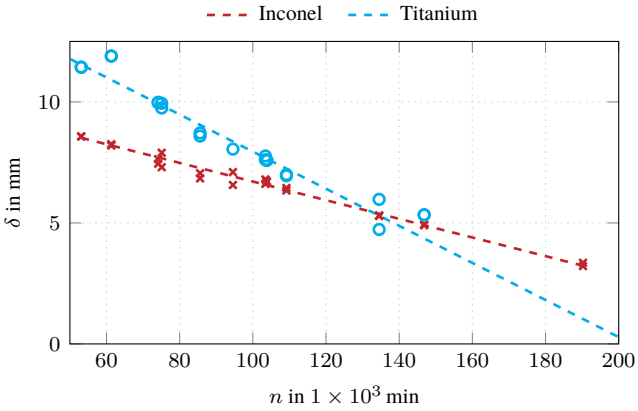

(c) Magnetic air gap length δ

Figure 6.6: Design study results for fuel cell electric compressors with a circumferential speed of $v_c = 210\,\mathrm{m\,s^{-1}}$

that the same outer rotor diameter makes better use of the same volume due to the smaller sleeve thickness required.

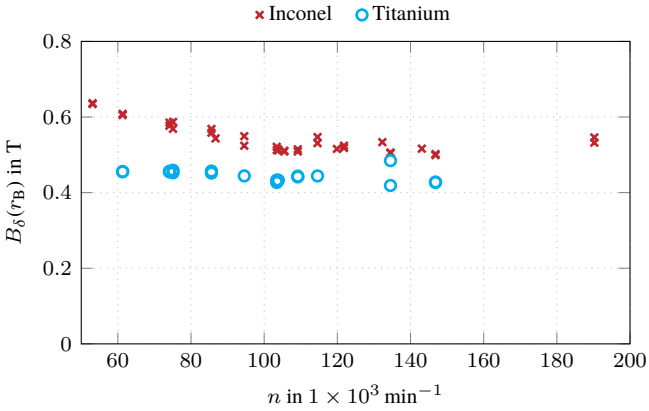

Figure 6.7: Resulting air gap flux density for a constant circumferential speed of $v_c = 210\,\mathrm{m\,s^{-1}}$

6.3.1.3 Stator Design

Next, the stator design and the difference in winding design are described and shown. When optimizing the efficiency of the machines, solutions for q between 1 and 4 are possible. The optimization aims at minimizing the total losses. The rotor losses are mainly influenced by slotting and winding harmonics. In Fig. 6.8 the different designs are compared over speed and frequency. First, the optimization targets designs with $q \geq 2$ and therefore $N \geq 12$. It is also seen that the increasing speed leads to a reduction in the number of slots, due to the lack of space for more slots and a minimum tooth width required to meet manufacturing constraints. Most windings have a coil span reduced by one slot to reduce the harmonic content in the air gap flux density. Only a few machines have a single layer winding. These machines have a high rotational speed compared to machines with the same number of slots. It can be observed that the 18 slot configurations have the widest range of application for the circumferential speed used. Reducing the circumferential speed results in a shift to a smaller number of slots.

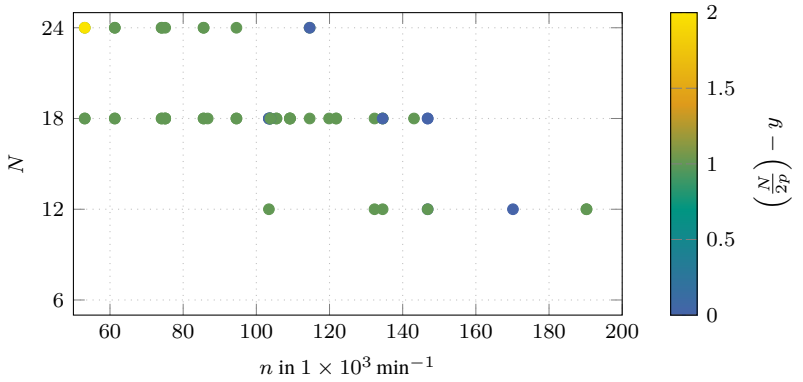

Figure 6.8: Number of slots N over the operating speed of the electric compressor for a circumfirential design speed of $v_c = 210\,\mathrm{m\,s^{-1}}$. Since the machine design features only one pole pair, the number of slots is directly proportional to the number of slots per pole per phase (q). The color bar indicates the reduction in the coil span, measured by the number of slots.

6.3.2 Variation of the Circumferential Speed at Constant Load

In the following section, the effect of circumferential speed is examined. Therefore, a constant operating point is chosen. A compressor power requirement of $15\,\mathrm{kW}$ and a compressor pressure ratio of 2.5 are investigated, along with the addition of a turbine to the system. The compressor optimization results in a speed of $121\,000\,\mathrm{min^{-1}}$. The compressor wheel diameter d_2 is $68.6\,\mathrm{mm}$. The turbine generates $5\,\mathrm{kW}$ and reduces the power requirement for the machine to $10\,\mathrm{kW}$. The study includes machine designs with circumferential speed variation from $150\,\mathrm{m\,s^{-1}}$ to $250\,\mathrm{m\,s^{-1}}$ in steps of $5\,\mathrm{m\,s^{-1}}$. First, note that a suitable design can be found for all speeds. In Fig. 6.9 (a) the critical length l_{cr} and the actual length l_{Fe} are shown. It can be seen that the critical length of the machine increases with the circumferential speed and with the increasing diameter of the shaft. The optimized length of the machine is also shown. In the low speed range of $150\,\mathrm{m\,s^{-1}}$ to $165\,\mathrm{m\,s^{-1}}$ the machine design is limited by the eigenfrequency of the shaft. With further increasing speeds above $170\,\mathrm{m\,s^{-1}}$ the active length decreases and remains almost constant at speeds above $200\,\mathrm{m\,s^{-1}}$. From this it

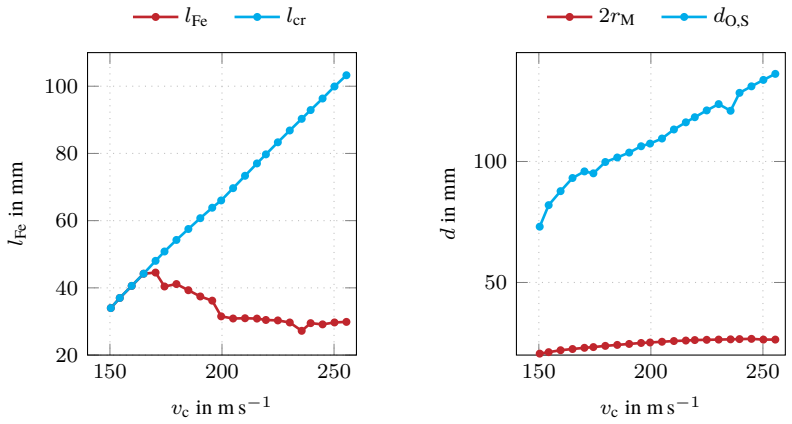

(a) Actual active length l_{Fe} compared to the critical length l_{cr}

(b) Magnet radius over circumferential speed

Figure 6.9: Influence of the circumferential speed on the overall machine dimensions

can be concluded that the increase of the circumferential speed leads to an increased potential in terms of eigenfrequency and critical length. It also indicates that higher loads can be realized with the limit of constant weight of the rotating aerodynamic components and the same speed. It can be observed that the stator diameter grows linearly with the peripheral speed. The magnet, on the other hand, does not grow linearly with speed. For the investigated machine, the magnet diameter actually reaches its maximum at $240\,\mathrm{m\,s^{-1}}$ and then starts to decrease. This also indicates that increasing the speed further under the chosen boundary conditions is not appropriate and will not increase the machine performance.

Having understood that circumferential speed increases the total volume of the machine, the question remains as to how it affects the efficiency of the machine. Therefore, the comparison of losses is shown in Fig. 6.10. The total losses are separated into the individual losses and therefore the speed and design influence can be verified on each of the individual losses. The total losses have their maximum at $150\,\mathrm{m\,s^{-1}}$. This can be explained by the length limitation seen earlier. With increasing speed, the losses first decrease until $165\,\mathrm{m\,s^{-1}}$. After that, the

total losses increase linearly. Looking at the different losses, the core losses P_{Fe} decrease over the whole speed range. The explanation for that is observed in Fig. 6.11. As the air gap flux density decreases, so does the core flux density. This results in lower total core losses in the machine even though the total core volume increases. At the same time, the ohmic losses P_{DC} remain constant

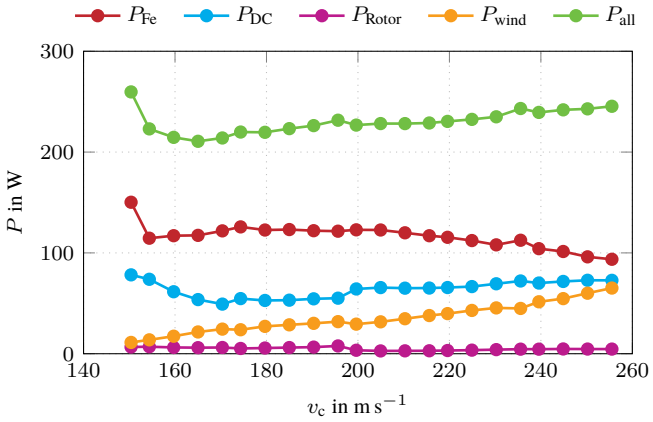

Figure 6.10: Separation of the machine losses over a variation of circumferential speeds v_{c}.

with a small exception in the range of $150\,\mathrm{m\,s^{-1}}$ to $170\,\mathrm{m\,s^{-1}}$, where the copper losses have their minimum. In parallel, the windage losses P_{wind} increase with increasing circumferential speed. This can be expected from the relationship shown in eq. (3.88). The influence of circumferential speed, which is cubic, is greater than the influence of decreasing length, which is linear. The decrease of the core losses is not sufficient to compensate the losses of the increasing windage losses. In the proposed designs, rotor losses do not play a significant role. Therefore, the copper and magnet temperatures are plotted in Fig. 6.12. It can be seen that the design space has two local minima for the magnet temperature at $170\,\mathrm{m\,s^{-1}}$ and at $210\,\mathrm{m\,s^{-1}}$. Compared to the magnet temperature, the winding has only one minimum at $170\,\mathrm{m\,s^{-1}}$. However, all part temperatures are uncritical, and therefore all machine designs are suitable for the application. With efficiency as the main objective, it is advantageous to go for low circumferential speeds to keep winding losses low and also save on material usage. To get a better idea of the proposed machine designs, four machine designs are shown

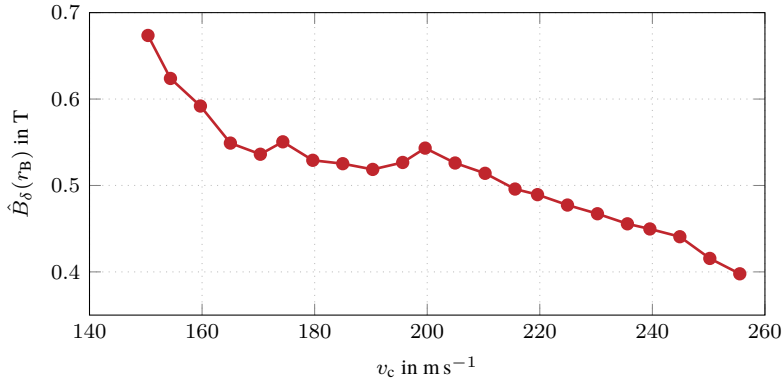

Figure 6.11: Air gap flux density of the electric machines over the circumferential speed v_c.

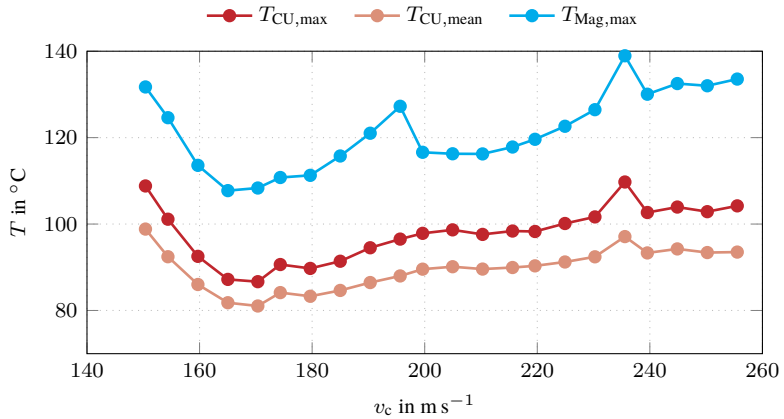

Figure 6.12: Part temperature of the two critical machine components, the magnet and the winding.

in Fig. 6.13. The design optimization proposes a design with twelve slots up to $195\,\mathrm{m\,s^{-1}}$ and a design with 18 slots for higher speeds. This indicates that both designs have their break-even point in terms of losses in this speed range for the application. In addition, the phenomena already described can be seen. The temperature distribution inside the machine is also visible. The hottest area in all cases is the magnet. The magnet temperature is mainly driven by the heat transfer from the rotor to the stator, which is limited by the air gap length. The winding is the second hottest component in the machine. Since the slots have a large height compared to the overall size of the machine, the temperature on the winding near the air gap is significantly hotter than the upper part near the stator yoke.

6.3.3 Optimization of Mass and Volume

In the results presented so far, the focus is on minimizing the losses of the entire electric machine. Therefore, mass and volume are not part of the optimization. This leads to designs that use as much material as the constraints allow. Therefore, the following results include volume minimization as a second optimization objective. Since reducing the volume leads to higher flux densities in the core material and higher current densities in the windings by keeping the air gap flux density and current load constant, it will lead to higher losses. For the following investigations, the same design of an electric hydrogen fuel cell compressor with a compressor power requirement of $15\,\mathrm{kW}$ and a compressor pressure ratio $\Pi_{\mathrm{C,t\text{-}t}}$ of 2.5 is investigated. A turbine is also added to the system. The resulting rotational speed is $121\,000\,\mathrm{min^{-1}}$. The diameter of the compressor wheel d_2 is $68.6\,\mathrm{mm}$. The power regenerated by the turbine is calculated to be $5\,\mathrm{kW}$. Therefore, the power requirement for the electric machine is $10\,\mathrm{kW}$. In Fig. 6.14 (a) the results of the Pareto optimization are shown. The x-axis shows the total losses of the system and the y-axis shows the total volume in $\mathrm{dm^3}$. Each point is a machine design for the described requirements. The color of the points indicates the magnet temperature for the design. It can be noticed that a decrease in volume leads to an increase in losses simply because of a higher power density and a smaller cooling surface. Overall, the behavior is linear over a wide range above $270\,\mathrm{W}$. To reduce the losses even further, the gradient of $\frac{V_{\mathrm{active}}}{P_{\mathrm{all}}}$ decreases further, which means that more active volume is needed to reduce the losses compared to the range above $270\,\mathrm{W}$. It is observed that designs with total machine losses of $245\,\mathrm{W}$ to $255\,\mathrm{W}$ are suitable for the requirement. It is also seen that machine designs with volumes below $0.3\,\mathrm{dm^3}$ have high rotor temperatures close to the accepted temperature limit of $200\,^{\circ}\mathrm{C}$ or above. A further exploration of the results

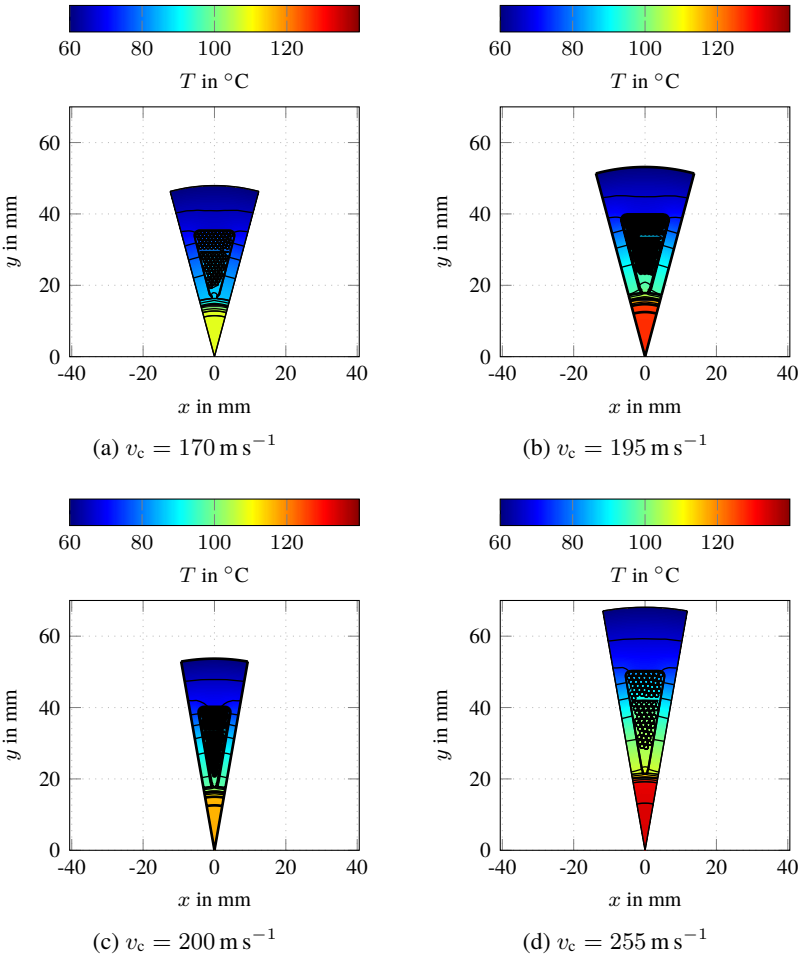

(a) $v_c = 170\,\mathrm{m\,s^{-1}}$ (b) $v_c = 195\,\mathrm{m\,s^{-1}}$

(c) $v_c = 200\,\mathrm{m\,s^{-1}}$ (d) $v_c = 255\,\mathrm{m\,s^{-1}}$

Figure 6.13: Temperature distribution over the circumferential speed of the machines.

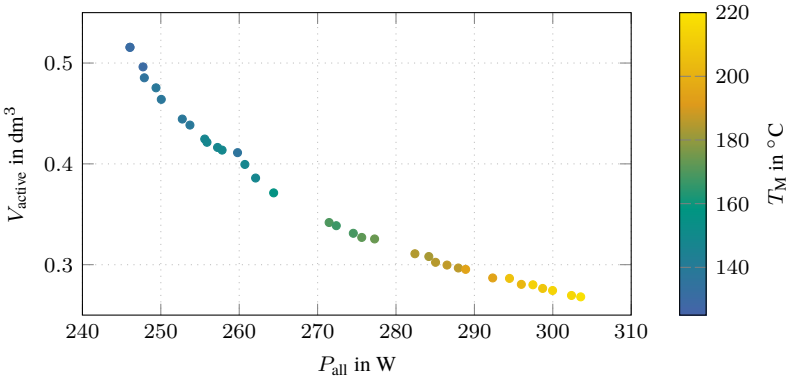

(a) Multi-objective optimization minimizing losses and volume of the electric machine.

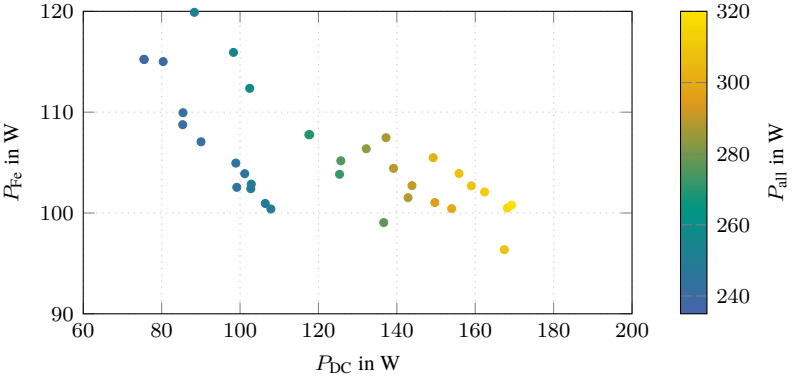

(b) Multi-objective optimization minimizing losses and volume of the electric machine separated into core and copper losses.

Figure 6.14: Results of the multi-objective optimization.

is shown in Fig. 6.14 (b). The copper losses P_{DC} are on the x-axis and the core losses P_{Fe} are on the y-axis. The data points are highlighted in the color corresponding to the total losses. Looking at the results from Fig. 6.14 (b), two things can be observed. The minimal total losses are not minimizing the core losses and the copper losses. Instead, minimizing the copper losses is the main goal for minimum system losses. Reducing the slot area and increasing the current density will reduce the core losses, but they cannot compensate for the increase in copper losses. Considering that AC losses are not studied, the results may be even more in favor of minimizing copper losses.

6.4 Design Conclusions and Limitations

A number of design conclusions are drawn from the studies conducted and the specific application for fuel cell compressors.

Design of High-Speed Electric Machines

The rotor design is constrained by the mechanical properties of the magnets, the rotor sleeve, the bearing system, and the connected loads. Two key factors limit the rotor design: the material strength of the rotor sleeve and the first bending eigenfrequency of the rotor. To achieve maximum efficiency, the circumferential speed should be chosen so that the required active length is as close as possible to the limit allowed by the bending eigenfrequency. This reduces the overall machine volume while maximizing efficiency. Operating at lower circumferential speeds is beneficial because higher speeds increase windage losses, which negatively affect system efficiency. In addition, slower circumferential speeds reduce the amount of material required in the design.

With the selected materials, there is a critical circumferential speed limit where the magnet diameter begins to decrease rather than increase. Beyond this speed, further increases in speed do not provide any benefit because the active volume of the machine stops growing. For Inconel 718, this critical circumferential speed is higher than for Titanium due to its better assembly capability. Based on the given design constraints, a circumferential speed limit of approximately $250\,\mathrm{m\,s^{-1}}$ is identified for Inconel 718.

The stator design prioritizes distributed windings to reduce flux harmonics. To minimize total losses, the number of slots per pole and phase should be as high as possible within the limits of manufacturability, such as available tooth width. Minimizing copper losses also plays a critical role in reducing total losses.

However, the current design approach to temperature calculation does not provide feedback for magnetic optimization. While minimizing losses increases the air gap, this increased gap reduces heat transfer from the rotor to the stator. Since magnet temperature is critical and has a significant impact on machine performance, further investigation of air gap length is recommended. Reducing the air gap could potentially improve material utilization and thermal management, thereby improving overall machine performance.

Application in Fuel Cell Compressors

The tool chain presented for the study includes many aspects of the overall system design. Therefore, a wide range of compressors are designed and compared in the results shown so far. It can be seen that based on the base compressor stage and characteristics, a scaling of the outer compressor wheel diameter defines the speed range of the applications. As seen in eq. (3.3), the compressor optimization is based on the scaling of the outer diameter and all other dimensions in relation to it. Therefore, an optimization for smaller volume flows will result in a smaller outside diameter d_2 because the inlet area must be reduced to fit the volume flow. To keep the pressure demand constant, the circumferential speed of the compressor wheel must be maintained and therefore the speed requirement increases. This approach is valid in principle, but results in very high speeds. Without considering the foil bearing dimensions in this work, the literature and published electric compressors for fuel cells show that designs above $150 \times 10^3\,\mathrm{min}^{-1}$ are not published in 2023. Due to the losses in the bearings, which could be estimated with the same equations as for the air gap friction, the losses will increase exponentially with higher speeds. Therefore, it must be concluded that the designs with speeds above $150 \times 10^3\,\mathrm{min}^{-1}$ are most likely not feasible. Here a different compressor design with a smaller trim ratio of $\frac{d_1}{d_2}$ should be used. This results in a compressor design with small inlet diameters and large outside diameters to meet the requirements of high pressures at low speeds and small volume flows. As a result, the efficiency of small capacity compressors is not as good as larger trim ratios, but the operating points can be reached at lower speeds. With pressure ratios above 2, the turbine designs show their potential to improve overall system efficiency. Therefore, comparing compressor system designs with and without a turbine doesn't significantly affect overall system performance. The turbine reduces the maximum active length of the electric machine, recovers energy, and reduces torque requirements. Both approaches show comparable performance.

Chapter 7

Summary

This thesis presents an efficient, semi-analytical multi-physics design approach for permanent magnet synchronous machines with a focus on high-speed machines. The results of this work are summarized in the following section and an outlook for further improvements is given.

7.1 Summary and Results of this Work

High-speed electric machines are used in many applications. One application is electric compressors in hydrogen fuel cell systems to supply oxygen to the cathode. Pressurizing the air for the PEM fuel cell increases the power density of the fuel cell and thus reduces the overall volume and weight of the system. It is therefore of particular interest for mobile applications. The design of the electric compressor includes the design of the turbomachinery components, which are a radial compressor and a radial turbine, the mechanical design of the rotor assembly, the magnetic design, and the thermal design of the machine. For the turbomachinery, scaling approaches are presented and used. The calculations are based on a reference compressor presented in this thesis. An analytic approach for the sleeve calculation is presented, which explains the details of the different loads the rotor assembly is subjected to during operation. Analytic solutions for the magnetic design are considered and the limitations for small machines with large air gaps are pointed out. The air gaps for machines of this size cannot be considered small, so the surface area of the rotor and stator is not identical. In addition, the large air gap leads to leakage flux that closes in the air gap. As a result, the radial flux density along the machine radius decreases non-linearly.

To solve these challenges, a new design approach was developed using neural networks to determine the permanent magnet flux and the permeance function to include the slotting effect in the air gap field. Finally, for the thermal design of the machine, the eddy current losses caused by the harmonics of the air gap flux are determined and the stator core losses are included. Winding and copper losses are also included. The design process is completed with a thermal 2D-FEA of the machine design. An optimization process for an electric compressor is presented. The focus is on the magnetic design and the goal to minimize the losses. In the work the efficiency is always an important goal. A multi-criteria optimization is presented to understand the influence between efficiency and machine volume. The proposed model is validated on an electric machine designed for a fuel cell application with a design speed of $140\,000\,\mathrm{min}^{-1}$ and a peripheral speed of $230\,\mathrm{m\,s}^{-1}$. The overall validation shows very well the precession of the presented model. Except for the rotor losses and higher harmonics in the air gap field, all deviations are below $10\,\%$. In most cases the deviations from the FEA results are below $5\,\%$. In the optimization process, the influence of the sleeve material was worked out. Inconel 718 gives better performance compared to TiAl6V4, although the resistivity of titanium is higher and therefore the eddy current losses in the sleeve should be lower. The material properties, especially the thermal expansion factor and the limited temperature range for the assembly process, limit the performance of the titanium sleeve. The results show that machines with Inconel 718 sleeves have a higher magnetic air gap flux densities and are able to reach operating points, especially higher pressure ratios and therefore higher speeds compared to titanium. The influence of circumferential speed is also investigated. It is shown that higher circumferential speeds provide the opportunity to achieve higher output powers due to the increased stiffness and therefore higher eigenfrequency of the rotor. When the load is constant, it is seen that the higher speeds cause higher losses, especially windage losses, and require a larger overall volume. Therefore, the machine should be operated at the lowest possible circumferential speeds. It is also shown that the maximum circumferential speed up to which the diameter of the magnet grows is limited to $240\,\mathrm{m\,s}^{-1}$ for Inconel 718. In the Paetro optimization of the system with constant circumference for a defined load, it is seen that the reduction of copper losses has the greatest impact on the overall system efficiency. Overall, it can be seen that the application for fuel cell air compressors is challenging in many aspects. The limitations caused by the bearing system are not considered in this work.

7.2 Outlook

The work presented provides opportunities to further develop the design approach for electric compressors. The following four areas have been identified. Overall, the design approach covers solid magnets in combination with a metallic sleeve, so designs with ring magnets and segmented magnets would be of interest.

Aerodynamic Design

For the compressor and turbine design, simple approaches have been used based on existing data. It can be seen that the overall system is highly dependent on the characteristics of the compressor. Therefore, it would be beneficial to use a library of different compressors as an optimization to check the feasibility for the application and how the compressor design influences the system design.

Mechanical Design

The mechanical design takes into account all relevant loads to which the rotor assembly is subjected during operation and during assembly. The different temperature levels of the components are also considered in the design process. However, the design process could be improved to include temperature dependent material properties. In addition, the design can be extended to include fiber-reinforced sleeves, which have the potential to improve magnetic performance but require a more complex calculation approach due to the anisotropic material behavior. The low thermal expansion factor of fiber-reinforced sleeves would make it interesting to explore the feasibility of NdFeB magnets in combination with these materials. In addition, a more detailed consideration of the foil bearings is important.

Magnetic Design

The magnetic domain provides accurate results for the applied fundamental currents in many regions. The PWM dependent losses in high-speed machines are very sensitive to the machine design. Factors such as DC bus voltage, inductance, inverter topology, and switching frequency play a role. These factors should be investigated for further improvement of the model. For research purposes, the use of the proposed model to predict the air gap flux density could be tested for other rotor designs, such as ring magnets, but also for larger machines such as traction drives and IPM rotors. Therefore, an approach to account for the nonlinearity of the core materials needs to be developed.

Thermal Design

The thermal design can be improved to understand the system. A thermal model based on the thermal equivalent circuit is recommended to explore the influence of bearing losses, compressor bypass flows, and active rotor cooling. In addition, the feedback loop in the design flow can be improved. Therefore, an additional optimization criterion such as the magnet temperature could be implemented to find the optimal air gap length for a minimum part temperature. Due to the complexity and influence of such a model, a thermal equivalent circuit is required.

List of Symbols

Abbreviations

BEV	Battery Electric Vehicle
C	Compressor
CO_2	Carbon Dioxide
DC	direct current
FC	Fuel Cell
FCEV	Fuel Cell Electric Vehicle
FEA	Finite Element Analysis
FFT	Fast Fourier Transformation
HSPMSM	High-Speed Permanent Magnet Synchronous Machine
HU	Humidifier
IC	Intercooler
IM	induction machine
IPM	Internal Permanent Magnet Synchronous Machine
MGT	Micro Gas Turbine
MMF	magnetomotive force
MTPA	Maximum Torque per Ampere
NdFeB	Neodym iron boron magnet
NN	Neuronal Network
PEM	Proton exchange membrane
PM	Permanent Magnet
PMSM	Permanent Magnet Synchronous Machine
PWM	Pulse Width Modulation
SM	synchronous machine

Sm_2Co_{17}	Samarium Cobalt Alloy
SPMSM	Surface Mounted Permanent Magnet Synchronous Machine
SRM	Switched Reluctance Machine
T	Turbine
TMP	Turbomolecular Pump
WLTP	Worldwide Harmonized Light-Duty Vehicles Test Procedure
WS	Water seperator

Formulars

Latin Symbols

A_c	conducter cross-section
B_dc	DC flux density
B_R	remanence flux density
$\boldsymbol{B}_{\delta,\mathrm{h_{PM}}}$	sinusoidal air gap flux density of the cylindrical permanent magnet with the height of h_PM
$B_{\delta,\mathrm{Rotor}}$	air gap flux density proportion of the rotor
$B_{\delta,\mathrm{Stator}}$	air gap flux density proportion of the stator
$\hat{B}_\delta$	air gap flux density amplitude
$\boldsymbol{B}_{\delta,\mathrm{h_{PM}},\mathrm{b_1}}$	air gap flux density of the cylindrical magnet with the height of h_PM and the stator slot opening with of b_1
B_δ	air gap flux density
$\hat{B}$	flux density amplitude
B	flux density
C_f	friction coefficient
E_I	young's module inner part
E_O	young's module outer part
E	young's module
F_g	geometrical factor of the air gap
H_c	coercive field strength
i_RMS	max. RMS phase current
J	current density
$L_\mathrm{d,main}$	main inductance in d-direction
L_d	inductance in d-axis

$L_{\text{q,main}}$	main inductance in q-direction
L_{q}	inductance in q-axis
$L_{\sigma,\text{ sl}}$	leakage flux consisting of slot leakage and tooth tip leakage
L_{σ}	leakage inductance
L_{wh}	winding head leakage flux
L	overall inductance
T_{CW}	compressor wheel torque
N_{PM}	neuronal network predicting permanent magnet air gap flux
Nu	Nusselt number
N	number of slots
P_{C}	compressor power
P_{DC}	copper losses
P_{FC}	fuel cell stack power
P_{Rotor}	eddy current losses in the rotor
P_{T}	turbine power
P_{all}	all losses in the electric machine
P_{Fe}	core losses
P_{c}	eddy current losses
P_{wind}	windage losses caused by the rotor
P_{out}	output power
P	power
Q_{I}	diameter ratio of the inner diameter of the inner part to the joint diameter
Q_{O}	diameter ratio of the joint diameter to the outer diameter of the outer part
R_{1}	phase resistance
Re_{δ}	Couette-Reynolds number of the air flow in the air gap
Re	Reynolds number
SF	safety factor
T_{1}	temperature 1 (e.g. room temperature)
T_{2}	temperature 2 (e.g. operating temperature)
T_{4}	air temperature at turbine inlet
T_{EM}	mechanical torque provided by the electric machine
T_{M}	magnet temperature
$T_{\text{R,max}}$	maximum Rotor temperautre

T_{TW}	turbine wheel torque
T_{el}	inner torque
T_{sh}	shaft torque
$T_{\mathrm{tot,in}}$	total temperature at inlet
$T_{\mathrm{tot,out}}$	total temperature at outlet
Ta	Taylor number
V_{DC}	DC-bus voltage
U_{W}	gemetrical effective overlap
V_{active}	active volume of the machine
a	parallel paths
b_1	slot opening width
b_2	stator teeth width
b_{t}	stator tooth width
c_0	isentropic spouting velocity
c_{p}	heat capacity
d_1	compressor inlet diameter
$d_{2,\mathrm{new}}$	new compressor outlet diameter
$d_{2,\mathrm{old}}$	old compressor outlet diameter
$d_{2,\mathrm{ref}}$	reference compressor outlet diameter
d_2	compressor outlet diameter
d_3	turbine outlet diameter
d_4	turbine inlet diameter
d_{Cu}	effective copper diameter
d_{Ii}	inner diameter of the inner part
d_{Ii}	outer diameter of the inner part
d_{J}	joint diameter
d_{Oi}	inner diameter of the outer part
d_{Oo}	outer diameter of the outer part
$d_{\mathrm{O,S}}$	outer diameter of the stator
d_{h}	hydraulic diameter
f_{cr}	critical eigenfrequency
f	electrical frequency
h_1	stator slot height
h_4	slot height

h_{PM}	magnet height
h_{Slot}	height of layer seperation
h_{y}	stator yoke height
h	convective heat transer coefficient
i_{nom}	nominal current
i_{d}	current in d-axis
i_{q}	current in qs-axis
i	current
k'	running variable of the stator phases (field effect)
k_{DC}	DC offset loss factor
k	running variable of the stator phases (field cause)
k_c	winding head length factor
k_{c}	eddy current loss factor
k_{e}	excess loss factor
k_{h}	hysterisis loss factor
${}^{s}k_{\mathrm{w},k_1}$	winding factor
k_1	roughness coefficient
l_0	reference length
$l_{\mathrm{CW,new}}$	new length of the compressor wheel
$l_{\mathrm{CW,old}}$	old length of the compressor wheel
l_{CW}	compressor wheel length
l_{Fe}	core length
l_{RAFB}	length of radial air foil bearing
l_{TW}	turbine wheel length
l_{cr}	critical active length
l_{c}	conducter length
l_{wh}	winding head length
m_{T}	mass flow to the turbine
$\dot{m}_{\mathrm{FC}}$	mass flow of the fuel cell
m	number of phases
n_{max}	maximum rotational speed
n	rotational speed
$p_{1,\mathrm{tot}}$	total pressure at compressor inlet
$p_{2,\mathrm{tot}}$	total pressure at compressor outlet

$p_{3,\mathrm{tot}}$	total pressure at turbine outlet
$p_{4,\mathrm{st}}$	static pressure at turbine inlet
$p_{4,\mathrm{tot}}$	total pressure at turbine inlet
$p_{\mathrm{J,o}}$	joint pressure at $n = 0\,\mathrm{min}^{-1}$
$p_{\mathrm{J,n}}$	joint pressure at n
p	pole pairs
q	number of slots per pole per phase
r_{B}	stator bore radius
r_{RAFB}	shaft radius of radial air foil bearing
r_{S}	sleeve radius
r_{avg}	mean air gap radius
r_{M}	magnet radius
r_{w}	average radius of the winding
r_{i}	inner radius
r_{o}	outer radius
r	radius
s	harmonic order
t_{S}	Sleeve thickness
t	time
u_2	circumferential speed of the compressor wheel at the diameter d_2
u_4	circumfirentical speed of the turbine wheel at d_4
$u_{\mathrm{c,corr}}$	corrected cirumferential speed
u_{cell}	fuel cell voltage
u_{r}	radial displacement
$\dot{V}_{\mathrm{new}}$	new volume flow
$\dot{V}_{\mathrm{old}}$	old volume flow
$\dot{V}_{\mathrm{corr}}$	corrected volume flow
v_{c}	circumferential speed
w_{S}	width of the unrolled sleeve
w_{c}	turns per coil
w	series winding number
x_1	postition coordinate of the stator
y	coil span

Greek Symbols

Δh_{sg}	equivalent height of the slot
$\Delta h_{\mathrm{T,t\text{-}st,is}}$	total isentropic enthalpy difference of the turbine
Δs_k	edge length of a slot element
Λ_{12}	permeance for the mutual inductance
Λ_1	permeance for the self-inductance of the upper layer
Λ_2	permeance for the self-inductance of the lower layer
Λ	permeance function
Φ_{c}	Coil flux
Ψ	flux linkage
$\underline{\Theta}_1$	magnetic excitation
Θ	magnetic excitation curve
$\alpha_{\mathrm{m,mech}}$	spatially machine symmetry
α	thermal expansion coefficient
δ_{mech}	mechanical air gap
δ	magnetic air gap length
ε_{T}	thermal elongation
$\varepsilon_{\mathrm{rr}}$	radial elongation
$\varepsilon_{r\theta}$	shear strain
$\varepsilon_{\theta\theta}$	tangential elongation
$\eta_{\mathrm{CW,max}}$	maximum compressor efficiency
$\eta_{\mathrm{CW,new}}$	efficiency of the new compressor
$\eta_{\mathrm{CW,old}}$	old compressor efficiency
$\eta_{\mathrm{C,is}}$	compressor efficiency
$\eta_{\mathrm{T,is}}$	turbine efficiency
κ	isentropic exponent
Δh_k	slot element height
λ_{FC}	air stoichiometry
λ_{wh}	relative winding head leakage inductance
λ	thermal conductivity
μ_0	magnetic permeability constant for vacuum
μ_{PM}	magnetic permeability of the magnet
μ_{Fe}	magnetic permebility of the iron core

μ_r	magnetic permebility
ν_I	poisson's ratio inner part
ν_O	poisson's ratio outer part
ν_air	kinematic viscosity of air
ν	poisson's ratio
ω_lift	angular lift off speed in $[\omega_\mathrm{lift}] = \mathrm{rad\,s^{-1}}$
ω_max	maximum angular velocity
ω	angular speed
Π_TW	pressure ratio turbine
Π_new	new pessure ratio
Π_old	old pressure ratio
$\Pi_\mathrm{C,t\text{-}t}$	pressure ratio compressor (total to total)
Ψ_d	flux linkage in d-axis
Ψ_PM	permanent magnet flux linkage
$\Psi_\mathrm{q,main}$	main flux in q-direction
Ψ_q	flux linkage in q-axis
ρ_1	air density at compressor inlet
ρ_I	density inner part
ρ_O	density outer part
ρ_c	specific conductor resistivity
ρ_el	electrical resistivity
ρ	material specific density
σ_YS	yield limit of a material
σ_J	joint stresses
σ_M	magnet stresses
σ_S	sleeve stresses
σ_c	compressive strength
σ_eq	von Mieses stresses
σ_rr	radial stress
$\sigma_{\theta\theta}$	tangential stress
σ_t	tensile strength
σ	electric conductivity
τ_p	pole division factor
ξ_a	ratio of the air gap length to the slot opening

ξ_w	effective oversize

List of Figures

List of Tables

Bibliography

Own Publications

[E1] B. Jux, S. Foitzik, and M. Doppelbauer, "A Standard Mission Profile for Hybrid-Electric Regional Aircraft based on Web Flight Data," in *2018 IEEE International Conference on Power Electronics, Drives and Energy Systems (PEDES)*, 2018.

[E2] M. Halwas *et al.*, "Coherences between production technology and performance of electric traction drives," in *2019 9th international electric drives production conference (EDPC)*, 2019.

[E3] F. Hoffmann, B. Jux, and M. Doppelbauer, "Thermal Modeling of the Stator Slot in Electrical Machines Using an Extended Layer Approach," in *IECON 2019 - 45th Annual Conference of the IEEE Industrial Electronics Society*, vol. 1, 2019.

[E4] W. Wößner *et al.*, "Unwucht hochausgenutzter Synchronmaschinen: Ein modellbasierter Ansatz zur Vermeidung ungewollter Unwuchtänderungen," en, *Zeitschrift für wirtschaftlichen Fabrikbetrieb*, vol. 114, no. 7-8, 2019.

[E5] M. Halwas *et al.*, "Influences of design and manufacturing on the performance of electric traction [drives]," in *2020 international conference on electrical machines (ICEM)*, ISSN: 2381-4802, vol. 1, 2020.

[E6] B. Jux and M. Doppelbauer, "IMPACT OF INTER-TURN FAULT ONTO THE TRANSIENT THERMAL MACHINE BEHAVIOUR AND FAULT DEVELOPMENT," en, *IET Conference Proceedings*, vol. 2020, no. 7, 2021.

[E7] C. Digel, B. Jux, J. Jakubik, P. Breining, and M. Doppelbauer, “Design & operating point dependent surrogate models for PMSM,” in *Elektromechanische antriebssysteme 2023; 9. Fachtagung (VDE OVE)*, 2023.

[E8] B. Jux, R. Dabrowski, D. A. Subramani, and M. Doppelbauer, “Neuronal Networks to Determine Air Gap Flux Densities for High-Speed Electric Motors,” in *2023 IEEE International Electric Machines & Drives Conference (IEMDC)*, 5/18/2023, ISBN: 979-8-3503-9899-1.

Supervised Students Thesis

[S1] M. Améfia, “Fluidkühlung für die Rotoren elektrischer Antriebsmaschinen für die Automobilindustrie,” Master thesis, Karlsruher Institut für Technologie, 2018.

[S2] C. Digel, “Entwicklung einer Wuchtmaschine,” Bachelor thesis, Karlsruher Institut für Technologie, 2018.

[S3] L. John, “Konstruktion eines elektrischen Antriebsmotors für den Rennsporteinsatz in der Formula Student,” Bachelor thesis, Karlsruher Institut für Technologie, 2018.

[S4] B. Molins, “Parametrierung von thermischen Ersatzschaltbildern für elektrische Maschinen,” Bachelor thesis, Karlsruher Institut für Technologie, 2018.

[S5] J. Vollmer, “Mechanische Auslegung und Umsetzung eines leistungsverzweigten Hybrids für einen Demonstrator,” Bachelor thesis, Karlsruher Institut für Technologie, 2018.

[S6] S. Weik, “Bestimmung der elektromagnetischen und thermischen Betriebsparameter von hochausgenutzten Synchronmaschine auf Basis von Lastzyklen,” Master thesis, Karlsruher Institut für Technologie, 2018.

[S7] M. Weiss, “Mechanische Konzeptionierung und Auslegung eines Doppelrotors mit Oberflächenmagneten,” Master thesis, Karlsruher Institut für Technologie, 2018.

[S8] N. Bihr, “Entwicklung eines Prüfstandes zur Vermessung von Motorsegmenten,” Bachelor thesis, Karlsruher Institut für Technologie, 2019.

[S9] M. Grüner, “Thermische Modellierung des Wickelkopfes,” Bachelor thesis, Karlsruher Institut für Technologie, Elektrotechnisches Institut, 2019.

[S10] P. Keck, “Startorträger Kühlkonzepte für E-Maschinen,” Bachelor thesis, Karlsruher Institut für Technologie, 2019.

[S11] J. Meßmer, “Entwicklung von Herstelungsverfahren für Motoretten mit einer reduzierten Lebensdauer,” Bachelor thesis, Karlsruher Institut für Technologie, 2019.

[S12] D. Silys, “Thermische Modellierung eines Kugellagers,” Bachelor thesis, Karlsruher Institut für Technologie, 2019.

[S13] J. Suppanz, “Designverifikation eines hochausgenutzten Elektromotors mit innenliegender Kühlung und duroplastischem Leichtbaugehäuse,” Master thesis, Karlsruher Institut für Technologie, 2019.

[S14] C. Götz, “Elektromagnetische Auslegung eines elektrischen Antriebsmotors f¨ur den Rennsporteinsatz in der Formula Student,” Bachelor thesis, Karlsruher Institut für Technologie, 2020.

[S15] A. Hussein, “Untersuchung einer elektrischen Maschine zur Potentialbewertung einer neuartigen Wickelkopfkühlung,” Bachelor thesis, Karlsruher Institut für Technologie, 2020.

[S16] P. Treuherz, “Elektromagnetischer Entwurf einer Hochdrehzahlmaschine für eine Verdichteranwendung,” Bachelor thesis, Karlsruher Institut für Technologie, 2020.

[S17] C. Digel, “Potentialanalyse von maschinellem Lernen zur Auslegung von elektrischen Maschinen,” Master thesis, Karlsruher Institut für Technologie, 2021.

[S18] H. Hirsch, “Temperaturabhängige Auslegung elektrischer Maschinen auf Basis analytischer thermischer Modelle,” Master thesis, 2021.

[S19] T. Kühnel, “Konstruktion und Auslegung eines Maschinenprüfstands für Hochdrehzahlmaschinen,” Bachelor thesis, Karlsruher Institut für Technologie, 2021.

[S20] C. Xu, “Entwurf und Implemetierung einer FPGA basierten Regelung für Hochdrehzahlmaschinen,” Master thesis, Karlsruher Institut für Technologie, 2021.

References

[1] *COP28 The UAE Consensus Brochure*, United Nations, 2023.

[2] H. Kahl, M. Kahles, J. Kamm, and H. Scheuig, *Wirtschaft und Europa auf dem Weg zur Klimaneutralität - Der Green Deal der EU und seine Bedeutung für Deutschlands Energiewende.* Deutsche Energie-Agentur GmbH, Berlin, Germany, 2021.

[3] *Green Hydrogen Mission*, Government of India, Ministry of New and Renewable Energy, 2023.

[4] A. G. Elkafas, M. Rivarolo, E. Gadducci, L. Magistri, and A. F. Massardo, "Fuel Cell Systems for Maritime: A Review of Research Development, Commercial Products, Applications, and Perspectives," *Processes*, vol. 11, no. 1, 2022.

[5] D. Stolten and B. Emonts, Eds., *Fuel Cell Science and Engineering: Materials, Processes, Systems and Technology*, 1st ed. Wiley, 2012, ISBN: 978-3-527-33012-6.

[6] N. Belmonte, C. Luetto, S. Staulo, P. Rizzi, and M. Baricco, "Case Studies of Energy Storage with Fuel Cells and Batteries for Stationary and Mobile Applications," *Challenges*, vol. 8, no. 1, 2017.

[7] T. Wilberforce, A. Alaswad, A. Palumbo, M. Dassisti, and A. G. Olabi, "Advances in stationary and portable fuel cell applications," *International Journal of Hydrogen Energy*, vol. 41, no. 37, 2016.

[8] A. G. Olabi, T. Wilberforce, and M. A. Abdelkareem, "Fuel Cell Application in the Automotive Industry and Future Perspective," *Energy*, vol. 214, 2021.

[9] H. Lohse-Busch, K. Stutenberg, M. Duoba, and S. Iliev, "Technology assessment of a fuel cell vehicle: 2017 toyota mirai," Argonne National Laboratory (ANL), Argonne, IL (United States), Tech. Rep., 2018.

[10] J. Opletal. "Nio ET7 with 150 kwh semi-solid state battery achieves a 1,044 km range," Accessed: Mar. 16, 2025. https://carnewschina.com/2023/12/17/nio-et7-with-150-kwh-semi-solid-state-battery-achieves-a-1044-km-range/.

[11] M. McDee. "Nio ET7 Real Life Test sees it cover 649 miles with the new 150 kwh battery," Accessed: Mar. 16, 2025. https://www.arenaev.com/nio_et7_breaks_records_with_1044_km_range_with_the_new_150_kwh_battery-news-2892.php.

[12] *Global Hydrogen Review 2023*, International Energy Agency (IEA), Paris, France, 2023.

[13] M. Handwerker, J. Wellnitz, and H. Marzbani, "Comparison of Hydrogen Powertrains with the Battery Powered Electric Vehicle and Investigation of Small-Scale Local Hydrogen Production Using Renewable Energy," *Hydrogen*, vol. 2, no. 1, 2021.

[14] B. C. Maitra *et al.*, *DEMYSTIFYING THE FUTURE OF HYDROGEN MOBILITY IN INDIA: Exploring the potential of hydrogen to fuel India's growth*, Arthur D. Little, Ed., 2023.

[15] Y. Li, P. Pei, Z. Ma, P. Ren, and H. Huang, "Analysis of air compression, progress of compressor and control for optimal energy efficiency in proton exchange membrane fuel cell," *Renewable and Sustainable Energy Reviews*, vol. 133, 2020.

[16] T. Sugawara, T. Kanazawa, N. Imai, and Y. Tachibana, "Development of Motorized Turbo Compressor for Clarity Fuel Cell," in *SAE Technical Paper Series*, 2017.

[17] Y. Wan, J. Guan, and S. Xu, "Improved Empirical Parameters Design Method for Centrifugal Compressor in PEM Fuel Cell Vehicle Application," *International Journal of Hydrogen Energy*, vol. 42, no. 8, 2017.

[18] Wan Yu, Xu Sichuan, and HuaiSheng Ni, "Air Compressors for Fuel Cell Vehicles: An Systematic Review," *SAE International Journal of Alternative Powertrains*, vol. 4, no. 1, 2015.

[19] Y. Wu, H. Bao, J. Fu, X. Wang, and J. Liu, "Review of Recent Developments in Fuel Cell Centrifugal Air Compressor: Comprehensive Performance and Testing Techniques," *International Journal of Hydrogen Energy*, vol. 48, no. 82, 2023.

[20] Q. Yan, H. Toghiani, and H. Causey, "Steady State and Dynamic Prformance of Proton Exchange Membrane Fuel Cells (PEMFCs) under Various Operating Conditions and Load Changes," *Journal of Power Sources*, vol. 161, no. 1, 2006.

[21] B. Blunier and A. Miraoui, "Proton Exchange Membrane Fuel Cell Air Management in Automotive Applications," *Journal of Fuel Cell Science and Technology*, vol. 7, no. 4, 2010.

[22] A. Cruz Rojas, G. Lopez Lopez, J. Gomez-Aguilar, V. Alvarado, and C. Sandoval Torres, "Control of the Air Supply Subsystem in a PEMFC with Balance of Plant Simulation," *Sustainability*, vol. 9, no. 1, 2017.

[23] H. Liu, P. Li, A. Hartz, and K. Wang, "Effects of Geometry/Dimensions of Gas Flow Channels and Operating Conditions on High-Temperature PEM Fuel Cells," *International Journal of Energy and Environmental Engineering*, vol. 6, no. 1, 2015.

[24] M. Grujicic, K. M. Chittajallu, E. H. Law, and J. T. Pukrushpan, "Model-based control strategies in the dynamic interaction of air supply and fuel cell," *Proceedings of the Institution of Mechanical Engineers, Part A: Journal of Power and Energy*, vol. 218, no. 7, 2004.

[25] J. Klütsch, S. Pischinger, A. Schloßhauer, and D. Lückmann, "Simulationsgestützte Auslegung von Brennstoffzellen-Luftverdichtern," *MTZ - Motortechnische Zeitschrift*, vol. 82, no. 7-8, 2021.

[26] A. Kaufmann, "Using Turbocharger maps in gas exchange simulation and engine control units," *Forschung im Ingenieurwesen*, vol. 78, no. 1-2, 2014.

[27] P. Fröhlich, "Development of an oil free turbo compressor for mobile fuel cell applications – challenges and results," *FC^3 Fuel Cell Conference. Chemnitz, 26./27.11.2019*, 2019.

[28] Y. Zhao *et al.*, "Air and hydrogen supply systems and equipment for PEM fuel cells: a review," *International Journal of Green Energy*, vol. 19, no. 4, 2022.

[29] Z. Liu, L. Li, Y. Ding, H. Deng, and W. Chen, "Modeling and control of an air supply system for a heavy duty PEMFC engine," *International Journal of Hydrogen Energy*, vol. 41, no. 36, 2016.

[30] M. Antivachis, F. Dietz, C. Zwyssig, D. Bortis, and J. W. Kolar, "Novel High-Speed Turbo Compressor With Integrated Inverter for Fuel Cell Air Supply," *Frontiers in Mechanical Engineering*, vol. 6, 2021.

[31] D. Thirumalai and R. White, "Steady-state operation of a compressor for a proton exchange membrane fuel cell system," *Journal of Applied Electrochemistry*, vol. 30, no. 5, 2000.

[32] M. K. Gee, J. Garbak, and B. Sutton, "Cost and Performance Enhancements for a PEM Fuel Cell System," 2003.

[33] F. Dubas, C. Espanet, and A. Miraoui, "Design of a High-Speed Permanent Magnet Motor for the Drive of a Fuel Cell Air-Compressor," in *IEEE Vehicle Power and Propulsion Conference (VPPC)*, 2005, ISBN: 0-7803-9280-9.

[34] W. Jiang, J. Khan, and R. A. Dougal, "Dynamic centrifugal compressor model for system simulation," *Journal of Power Sources*, vol. 158, no. 2, 2006.

[35] J. F. Walton, M. J. Tomaszewski, C. A. Heshmat, and H. Heshmat, "On the Development of an Oil-Free Electric Turbocharger for Fuel Cells," in *Volume 5: Marine; Microturbines and Small Turbomachinery; Oil and Gas Applications; Structures and Dynamics, Parts A and B*, 2006, ISBN: 0-7918-4240-1.

[36] X. Zheng, Y. Zhang, H. He, and Z. Qiu, "Design of a Centrifugal Compressor With Low Specific Speed for Automotive Fuel Cell," in *Volume 6: Turbomachinery, Parts A, B, and C*, 2008, ISBN: 978-0-7918-4316-1.

[37] D.-K. Hong, B.-C. Woo, J.-Y. Lee, and D.-H. Koo, "Ultra High Speed Motor Supported by Air Foil Bearings for Air Blower Cooling Fuel Cells," *IEEE Transactions on Magnetics*, vol. 48, no. 2, 2012.

[38] Dongdong Zhao *et al.*, "Design and control of an ultra high speed turbo compressor for the Air Management of fuel cell systems," in *2012 IEEE Transportation Electrification Conference and Expo (ITEC)*, 2012, ISBN: 978-1-4673-1408-4.

[39] V. V. N. K. S. Koyyalamudi and Q. H. Nagpurwala, "Stall Margin Improvement in a Centrifugal Compressor through Inducer Casing Treatment," *International Journal of Rotating Machinery*, vol. 2016, 2016.

[40] L. Qi *et al.*, "Design and Research of a Centrifugal Compressor for Automotive Fuel Cell Systems," in *2018 IEEE International Conference on Mechatronics and Automation (ICMA)*, 2018, ISBN: 978-1-5386-6074-4.

[41] Y. Zhang, S. Xu, and Y. Wan, "Performance improvement of centrifugal compressors for fuel cell vehicles using the aerodynamic optimization and data mining methods," *International Journal of Hydrogen Energy*, vol. 45, no. 19, 2020.

[42] J.-H. Kim, D.-M. Kim, Y.-H. Jung, and M.-S. Lim, "Design of Ultra-High-Speed Motor for FCEV Air Compressor Considering Mechanical Properties of Rotor Materials," *IEEE Transactions on Energy Conversion*, vol. 36, no. 4, 2021.

[43] W. LI and G. FENG, "Design and Experimental Study of Centrifugal Compressor in Fuel Cell Vehicle," *Mechanics*, vol. 27, no. 1, 2021.

[44] D. Hu, J. Liu, F. Yi, Q. Yang, and J. Zhou, "Enhancing heat dissipation to improve efficiency of two-stage electric air compressor for fuel cell vehicle," en, *Energy Conversion and Management*, vol. 251, 2022.

[45] H. Zhang, W. Hua, W. Yu, and L. Yang, "Design and Experimental Validation of a High-Speed Permanent Magnet Machine for Centrifugal Air Compressor in Hydrogen Fuel Cell Power Station," in *2022 IEEE 20th Biennial Conference on Electromagnetic Field Computation (CEFC)*, 2022, ISBN: 978-1-66546-833-6.

[46] H. Zhang, W. Yu, and W. Hua, "Research on Stator Iron Loss of Ultra-high-speed Permanent Magnet Motor for Hydrogen Fuel Cell Air Compressor," in *2022 IEEE Transportation Electrification Conference and Expo, Asia-Pacific (ITEC Asia-Pacific)*, 2022, ISBN: 978-1-66549-206-5.

[47] H. Zhang, W. Yu, and W. Hua, "Design and Key Technology of Oil-Free Centrifugal Air Compressor for Hydrogen Fuel Cell," *CES Transactions on Electrical Machines and Systems*, vol. 6, no. 1, 2022.

[48] Z. Chen, H. Huang, Q. Chen, X. Peng, and J. Feng, "Novel multidisciplinary design and multi-objective optimization of centrifugal compressor used for hydrogen fuel cells," en, *International Journal of Hydrogen Energy*, vol. 48, no. 33, 2023.

[49] "Products | FISCHER Fuel Cell Compressor AG," Accessed: Dec. 16, 2023. https://www.fischer-fuelcell-compressor.com/de/produkte/.

[50] "FC Compressors - Xeca Turbo (Chengdu) Technology Co., Ltd.," Accessed: Dec. 26, 2023. https://www.xecaturbo.cn/en/col.jsp?id=127.

[51] A. Binder and T. Schneider, "High-speed inverter-fed AC drives," in *2007 International Aegean Conference on Electrical Machines and Power Electronics*, 2007.

[52] J. Pyrhonen, T. Jokinen, and V. Hrabovcová, *Design of Rotating Electrical Machines*. Chichester, West Sussex, United Kingdom and Hoboken, NJ: Wiley, 2008, ISBN: 978-0-470-69516-6.

[53] A. Binder, *Elektrische Maschinen und Antriebe: Grundlagen, Betriebsverhalten*, 2., aktualisierte Auflage. Wiesbaden: Springer Vieweg, 2017, ISBN: 978-3-662-53240-9.

[54] R. Abebe *et al.*, "High speed drives review: Machines, converters and applications," in *IECON 2016 - 42nd Annual Conference of the IEEE Industrial Electronics Society*, 2016.

[55] M. A. Rahman, A. Chiba, and T. Fukao, "Super high speed electrical machines - summary," in *IEEE Power Engineering Society General Meeting, 2004*, 2004, ISBN: 0-7803-8465-2.

[56] S. Singhal, H. Walter, and T. Tyer, "Concept, design and testing of a 12MW 9500 RPM induction motor with oil film bearings for pipeline applications in North America," in *Industry Applications Society 60th Annual Petroleum and Chemical Industry Conference*, 2013, ISBN: 978-1-4673-5110-2.

[57] W. Eichhammer and T. Fleiter, *Energy efficiency in electric motor systems: Technology, saving potentials and policy options for developing countries*, 2012.

[58] "Electricity production, consumption and market overview," Accessed: Aug. 15, 2022. https://ec.europa.eu/eurostat/statistics-explained/index.php?title=Electricity_production,_consumption_and_market_overview.

[59] M. Unger and P. Radgen, "Energy Efficiency in Compressed Air Systems – A review of energy efficiency potentials, technological development, energy policy actions and future importance," 2018.

[60] J. Howard and A. Engeda, "Analysis and Design of Centrifugal Blowers for the Pressure Ratio Range 1.2 - 1.8," in *Volume 1: Aircraft Engine; Fans and Blowers; Marine; Wind Energy; Scholar Lecture*, 2021, ISBN: 978-0-7918-8489-8.

[61] A. Boglietti, A. Cavagnino, A. Tenconi, and S. Vaschetto, "Key design aspects of electrical machines for high-speed spindle applications," in *IECON 2010 - 36th Annual Conference on IEEE Industrial Electronics Society*, 2010, ISBN: 978-1-4244-5225-5.

[62] C. Zwyssig, J. W. Kolar, and S. D. Round, "Megaspeed Drive Systems: Pushing Beyond 1 Million r/min," *IEEE/ASME Transactions on Mechatronics*, vol. 14, no. 5, 2009.

[63] "Vakuumerzeugung - Turbopumpen | Pfeiffer Vacuum," Accessed: Jun. 15, 2023. https://www.pfeiffer-vacuum.com/de/produkte/vakuumerzeugung/turbopumpen/.

[64] T. Ishikawa, Y. Hashimoto, and N. Kurita, "Optimum Design of a Switched Reluctance Motor Fed by Asymmetric Bridge Converter Using Experimental Design Method," *IEEE Transactions on Magnetics*, vol. 50, no. 2, 2014.

[65] D. Gerada *et al.*, "High-Speed Electrical Machines: Technologies, Trends, and Developments," *IEEE Transactions on Industrial Electronics*, vol. 61, no. 6, 2014.

[66] "Energy Efficiency: Capstone Green Energy Corporation (CGRNQ)," Accessed: Feb. 7, 2024. https : / / www . capstonegreenenergy . com / solutions/energy-efficiency.

[67] L. Goldstein *et al.*, *Gas-Fired Distributed Energy Resource Technology Characterizations*, 2003.

[68] James R. Bumby, E. S. Spooner, and Mariusz Jagieła, "Equivalent circuit analysis of solid-rotor induction machines with reference to turbocharger accelerator applications," 2006.

[69] J. Pyrhonen, J. Nerg, P. Kurronen, and U. Lauber, "High-Speed High-Output Solid-Rotor Induction-Motor Technology for Gas Compression," *IEEE Transactions on Industrial Electronics*, vol. 57, no. 1, 2010.

[70] Juha Saari and A. Arkkio, "Losses in high-speed asynchronous motors," in *International Conference on Electrical Machines, Paris, France, 5.-8.9.1994*, 1994.

[71] J. F. Gieras and J. Saari, "Performance Calculation for a High-Speed Solid-Rotor Induction Motor," *IEEE Transactions on Industrial Electronics*, vol. 59, no. 6, 2012.

[72] M. T. Caprio, V. Lelos, J. D. Herbst, and J. Upshaw, "Advanced Induction Motor Endring Design Features for High Speed Applications," in *International Electric Machines and Drives Conference*, 5/15/2005 - 5/15/2005, ISBN: 0-7803-8987-5.

[73] J. Lähteenmäki, *Design and voltage supply of high-speed induction mechines* (Acta polytechnica Scandinavica Electrical engineering series). Helsinki: Finnish Academies of Technology, 2002, vol. 108, ISBN: 951-666-607-8.

[74] R. Lateb, J. Enon, and L. Durantay, "High speed, high power electrical induction motor technologies for integrated compressors," in *Electrical Machines and Systems, 2009. ICEMS 2009. International Conference on*, 2009, ISBN: 978-1-4244-5177-7.

[75] B. M. Wood, C. L. Olsen, G. D. Hartzo, J. C. Rama, and F. R. Szenasi, "Development of an 11000-r/min 3500-HP induction motor and adjustable-speed drive for refinery service," *IEEE Transactions on Industry Applications*, vol. 33, no. 3, 1997.

[76] F. Viggiano and G. Schweitzer, *Active magnetic support and design of high speed rotors for powerful electric drives* (Proceedings of the Third International Symposium on Magnetic Bearings). 1992.

[77] Y. Honda, S. Yokote, T. Higaki, and Y. Takeda, "Using the Halbach magnet array to develop an ultrahigh-speed spindle motor for machine tools," in *IAS '97. Conference Record of the 1997 IEEE Industry Applications Conference Thirty-Second IAS Annual Meeting*, vol. 1, 1997.

[78] D. Gerada, A. Mebarki, N. L. Brown, H. Zhang, and C. Gerada, "Design, modelling and testing of a high speed induction machine drive," in *2012 IEEE Energy Conversion Congress and Exposition (ECCE)*, 2012.

[79] S. Mathew *et al.*, "Development of a Hybrid Rotor Structure for high-speed Laminated Rotor Induction Motor," in *2021 IEEE International Electric Machines 2021*.

[80] Roland Y. Siegwart, René Larsonneur, and Alfons Traxler, "Design and Performance of a High Speed Milling Spindle in Digitally Controlled Active Magnetic Bearings," 1990.

[81] A. Smirnov, N. Uzhegov, T. Sillanpaa, J. Pyrhonen, and O. Pyrhonen, "High-Speed Electrical Machine with Active Magnetic Bearing System Optimization," *IEEE Transactions on Industrial Electronics*, vol. 64, no. 12, 2017.

[82] T. Epskamp, B. Butz, and M. Doppelbauer, "Design and Analysis of a High-Speed Induction Machine as Electric Vehicle Traction Drive," in *2016 18th European Conference on Power Electronics and Applications (EPE'16 ECCE Europe)*, 2016.

[83] Y. Hu, J. Chen, and X. Ding, "Analysis and Computation on Magnetic Field of Solid Rotor Induction Motor," *IEEE Transactions on Applied Superconductivity*, vol. 20, no. 3, 2010.

[84] Jussi Huppunen, "High-Speed Solid-Rotor Induction Machine – Electromagnetic Calculation and Design," in *HIGH-SPEED SOLID-ROTOR INDUCTION MACHINE*.

[85] J. K. Laehteenmaeki and V. Soitu, *Comparison of solid steel rotors with a copper coating or with a copper cage for a 60 kW 60.000 rpm compressor*, 2000.

[86] Y. Liu *et al.*, "Application of an Amorphous Core to an Ultra-High-Speed Sleeve-Free Interior Permanent-Magnet Rotor," *IEEE Transactions on Industrial Electronics*, vol. 65, no. 11, 2018.

[87] J. Ou, “Improving high-speed electrical machines by amorphous metals,” Dissertation, Karlsruher Institut für Technologie, Elektrotechnisches Institut, HEV, Karlsruhe, 2019.

[88] T. Noguchi and K. Fujita, “Electrical and Mechanical Compatible Design of 15 kW, 150,000 r/min Ultra-High-Speed PM Motor,” in *2019 22nd International Conference on Electrical Machines and Systems (ICEMS)*, 2019.

[89] K. Wang, M. J. Jin, J. X. Shen, and H. Hao, “Study on rotor structure with different magnet assembly in high-speed sensorless brushless DC motors,” *IET Electric Power Applications*, vol. 4, no. 4, 2010.

[90] T. Noguchi, Y. Takata, Y. Yamashita, Y. Komatsu, and S. Ibaraki, “220000-r/min, 2-kW PM Motor Drive for Turbocharger,” *IEEJ Transactions on Industry Applications*, vol. 125, no. 9, 2005.

[91] C. Zwyssig, J. W. Kolar, W. Thaler, and M. Vohrer, “Design of a 100 W, 500000 rpm permanent-magnet generator for mesoscale gas turbines,” in *Fourtieth IAS Annual Meeting. Conference Record of the 2005 Industry Applications Conference, 2005*, vol. 1, 2005.

[92] J. Oyama, T. Higuchi, T. Abe, K. Shigematsu, and R. Moriguchi, “The Development of Small Size Ultra-High Speed Drive System,” in *2007 Power Conversion Conference - Nagoya*, 2007.

[93] Liping Zheng *et al.*, “Design of a superhigh-speed cryogenic permanent magnet synchronous motor,” *IEEE Transactions on Magnetics*, vol. 41, no. 10, 2005.

[94] I. Takahashi, T. Koganezawa, G. Su, and K. Ohyama, “A super high speed PM motor drive system by a quasi-current source inverter,” *IEEE Transactions on Industry Applications*, vol. 30, no. 3, 1994.

[95] T. Noguchi and M. Kano, “Development of 150000 r/min, 1.5 kW Permanent-Magnet Motor for Automotive Supercharger,” in *2007 7th International Conference on Power Electronics and Drive Systems*, 2007.

[96] A. Binder, T. Schneider, and M. Klohr, “Fixation of buried and surface-mounted magnets in high-speed permanent-magnet synchronous machines,” *IEEE Transactions on Industry Applications*, vol. 42, no. 4, 2006.

[97] P.-D. Pfister and Y. Perriard, "Very-High-Speed Slotless Permanent-Magnet Motors: Analytical Modeling, Optimization, Design, and Torque Measurement Methods," *IEEE Transactions on Industrial Electronics*, vol. 57, no. 1, 2010.

[98] G. Munteanu, A. Binder, T. Schneider, and B. Funieru, "No-load tests of a 40 kW high-speed bearingless permanent magnet synchronous motor," in *SPEEDAM 2010*, 2010.

[99] X. Zhang, Y. Wu, W. Huang, and C. Gao, "Research on rotor sleeve winding techniques for high-speed permanent magnet motors via NOL ring testing," *Applied Sciences*, vol. 13, no. 13, 2023, Number: 7411.

[100] "Armor sleeves made of CFRP – for electric motors under maximum performance conditions," Accessed: Mar. 29, 2025. https://backend.schunk-group.com/Schunk/BU-Mobility/Documents/Whitepaper/Schunk_Mobility_Armor-Sleeves_Whitepaper_EN.pdf.

[101] W. Li, H. Qiu, X. Zhang, J. Cao, and R. Yi, "Analyses on Electromagnetic and Temperature Fields of Superhigh-Speed Permanent-Magnet Generator With Different Sleeve Materials," *IEEE Transactions on Industrial Electronics*, vol. 61, no. 6, 2014.

[102] M. Groninger, F. Horch, A. Kock, M. Jakob, and B. Ponick, "Cast coils for electrical machines and their application in automotive and industrial drive systems," in *2014 4th International Electric Drives Production Conference (EDPC 2014)*, 2014, ISBN: 978-1-4799-5008-9.

[103] I. Petrov, M. Polikarpova, P. Ponomarev, P. Lindh, and J. Pyrhonen, "Investigation of additional AC losses in tooth-coil winding PMSM with high electrical frequency," in *Proceedings, 2016 XXII International Conference on Electrical Machines (ICEM)*, 2016, ISBN: 978-1-5090-2538-1.

[104] S. Balasubramanian and M. Henke, "Performance Evaluation of a High-Speed Permanent Magnet Synchronous Machine with Hairpin Winding Technology," in *Proceedings 2020 International Conference on Electrical Machines (ICEM)*, 2020, ISBN: 978-1-7281-9945-0.

[105] P. B. Reddy and T. M. Jahns, "Scalability investigation of proximity losses in fractional-slot concentrated winding surface PM machines during high-speed operation," in *2011 IEEE Energy Conversion Congress and Exposition (ECCE 2011)*, 2011, ISBN: 978-1-4577-0542-7.

[106] S. Li, Y. Li, W. Choi, and B. Sarlioglu, "High-Speed Electric Machines: Challenges and Design Considerations," *IEEE Transactions on Transportation Electrification*, vol. 2, no. 1, 2016.

[107] C. Rollbühler, *Analyse der Verlustbestimmung permanentmagneterregter Synchronmaschinen für die Elektromobilität*, 2023.

[108] G. Bertotti, *Hysteresis in magnetism: For physicists, materials scientists, and engineers* (Academic Press series in electromagnetism), Digitaler Nachdr. San Diego [i pozostałe]: Academic Press, 2008, ISBN: 0120932709.

[109] J. Ou *et al.*, "Experimental Characterization and Feasibility Study on High Mechanical Strength Electrical Steels for High-Speed Motors Application," *IEEE Transactions on Industry Applications*, vol. 57, no. 1, 2021.

[110] D. Filsinger, G. Kuwata, and N. Ikeya, "Tailored Centrifugal Turbomachinery for Electric Fuel Cell Turbocharger," *International Journal of Rotating Machinery*, vol. 2021, 2021.

[111] B. Blunier and A. Miraoui, "Air management in PEM fuel cells: State-of-the-art and prospectives," in *2007 International Aegean Conference on Electrical Machines and Power Electronics*, 2007, ISBN: 978-1-4244-0890-0.

[112] S. Lück *et al.*, "Impact of Compressor and Turbine Operating Range Extension on the Performance of an Electric Turbocharger for Fuel Cell Applications," in *Volume 7: Industrial and Cogeneration; Manufacturing Materials and Metallurgy; Microturbines, Turbochargers, and Small Turbomachines; Oil & Gas Applications*, American Society of Mechanical Engineers, 2022, ISBN: 978-0-7918-8605-2.

[113] M. Heinrich, "Genetic Optimization of Turbomachinery Components using the Volute of a Transonic Centrifugal Compressor as a Case Study," Ph.D. dissertation, 2016.

[114] R. Dabrowski, *Steigerung der Abgasenergie-Rekuperationsleistung mittels Hybrid-Abgasturbolader durch Anpassung des Turbinendesigns auf hohe Druckverhältnisse*. Universität Rostock, 2019.

[115] T. Roß, *Neue Konzepte zur Abgasturboaufladung eines direkteinspritzenden Vierzylinder-Ottomotors* (Fortschrittberichte VDI : Reihe 12, Verkehrstechnik, Fahrzeugtechnik), Als Ms. gedr. Düsseldorf: VDI-Verl., 2008, vol. Nr. 687, ISBN: 978-3-18-368712-1.

[116] Syed Noman Danish, Ma Chaochen, and Ce Yang, "The Influence of Tip Clearance on Centrifugal Compressor Stage of a Turbocharger," 2006.

[117] B. Lüddecke, D. Filsinger, and J. Ehrhard, "On Mixed Flow Turbines for Automotive Turbocharger Applications," *International Journal of Rotating Machinery*, vol. 2012, 2012.

[118] *DIN 7190-1:2017-02, Pressverbände Teil Berechnungsgrundlagen und Gestaltungsregeln für zylindrische Pressverbände*.

[119] F. G. Kollmann, *Welle-Nabe-Verbindungen: Gestaltung, Auslegung, Auswahl*. Berlin: Springer, 1983, ISBN: 978-3-540-12215-9.

[120] D. Gross and T. Seelig, *Bruchmechanik: Mit einer Einführung in die Mikromechanik*. Heidelberg: Springer Vieweg, Berlin, Heidelberg, 2016, ISBN: 978-3-662-46737-4.

[121] L. Gu, E. Guenat, and J. Schiffmann, "A Review of Grooved Dynamic Gas Bearings," *Applied Mechanics Reviews*, vol. 72, no. 1, 2020.

[122] B. Sternlicht and E. B. Arwas, *State-of-the-art of gas-bearing turbomachinery*, Technical Report, Prepared for Office of Naval Research under Contract Nonr-4535(00), Latham, New York, 1965.

[123] V. Arora, P. J. M. van der Hoogt, R. G. K. M. Aarts, and A. de Boer, "Identification of stiffness and damping characteristics of axial air-foil bearings," *International Journal of Mechanics and Materials in Design*, vol. 7, no. 3, 2011.

[124] A. K. Hartmann, *Analytische Verfahren zum Entwurf und Modellierung umrichtergespeister, fremderregter Synchronmaschinen kleiner Leistung*, Siegen, 2016.

[125] B. Heller and V. Hamata, *Harmonic field effects in induction machines*. Amsterdam a.o: Elsevier, 1977, ISBN: 044499856X.

[126] Z. Q. Zhu and D. Howe, "Instantaneous magnetic field distribution in brushless permanent magnet DC motors. III. Effect of stator slotting," *IEEE Transactions on Magnetics*, vol. 29, no. 1, 1993.

[127] T. Hastie, R. Tibshirani, and J. H. Friedman, *The Elements of Statistical Learning: Data Mining, Inference, and Prediction* (Springer Series in Statistics), Second. New York, NY: Springer New York, 2009, ISBN: 9780387848587.

[128] N. Bianchi, S. Bolognani, and F. Luise, "Potentials and limits of high-speed PM motors," *IEEE Transactions on Industry Applications*, vol. 40, no. 6, 2004.

[129] J. Zhao, W. He, W. Fu, Y. Ding, and Y. Guo, "Comparative Studies on Performances of Slotted and Slotless High-Speed PMBLDC Motors," *IEEE Access*, vol. 12, 2024.

[130] J. Kolbe, "Zur numerischen Berechnung und analytischen Nachbildung des Luftspaltfeldes von Drehstrommaschinen," Thesis, Hochschule der Bundeswehr Hamburg, 1983.

[131] F. Ollendorff, *Potentialfelder der Elektrotechnik*. Julius Springer Verlag, Berlin, 1932.

[132] F. Taegen and J. Kolbe, "Carter-Faktor und Leitwertswellen elektrischer Maschinen mit magnetischem Nutverschlu," *Electrical Engineering (Archiv fur Elektrotechnik)*, vol. 78, no. 5, 1995.

[133] Z. Q. Zhu and D. Howe, "Instantaneous magnetic field distribution in brushless permanent magnet DC motors. II. Armature-reaction field," *IEEE Transactions on Magnetics*, vol. 29, no. 1, 1993.

[134] Z. Q. Zhu and D. Howe, "Instantaneous magnetic field distribution in permanent magnet brushless DC motors. IV. Magnetic field on load," *IEEE Transactions on Magnetics*, vol. 29, no. 1, 1993.

[135] Z. Q. Zhu, D. Howe, E. Bolte, and B. Ackermann, "Instantaneous magnetic field distribution in brushless permanent magnet DC motors. I. Open-circuit field," *IEEE Transactions on Magnetics*, vol. 29, no. 1, 1993.

[136] D. Zarko, D. Ban, and T. A. Lipo, "Analytical calculation of magnetic field distribution in the slotted air gap of a surface permanent-magnet motor using complex relative air-gap permeance," *IEEE Transactions on Magnetics*, vol. 42, no. 7, 2006.

[137] M. Hafner, D. Franck, and K. Hameyer, "Static Electromagnetic Field Computation by Conformal Mapping in Permanent Magnet Synchronous Machines," *IEEE Transactions on Magnetics*, vol. 46, no. 8, 2010.

[138] G. Müller and B. Ponick, *Theorie elektrischer Maschinen* (Elektrische Maschinen), 6., völlig neu bearb. Aufl. Weinheim: Wiley-VCH, 2009, vol. 3, ISBN: 9783527405268.

[139] G. Müller, K. Vogt, and B. Ponick, *Berechnung Elektrischer Maschinen*. Weinheim: Wiley-VCH, 2006-, ISBN: 3-527-40525-9.

[140] A. Cavagnino, "Accuracy-Enhanced Algorithms for the Slot Leakage Inductance Computation of Double-Layer Windings," *IEEE Transactions on Industry Applications*, vol. 53, no. 5, 2017.

[141] F. Magnussen and C. Sadarangani, "Winding Factors and Joule Losses of Permanent Magnet Machines with Concentrated Windings," in *Electric Machines and Drives Conference, 2003. IEMDC'03. IEEE International*, vol. 1, 2003.

[142] M. Markovic and Y. Perriard, "A Simplified Determination of the Permanent Magnet (PM) Eddy Current Losses due to Slotting in a PM Rotating Motor," 2008.

[143] J. Ou and M. Doppelbauer, "Torque analysis and comparison of the switched reluctance machine and the doubly-salient permanent magnet machine," in *2016 18th European Conference on Power Electronics and Applications (EPE'16 ECCE Europe)*, 2016, ISBN: 978-9-0758-1524-5.

[144] J. Saari, *Thermal Analysis of High Speed Induction Machines* (Acta polytechnica Scandinavica El, Electrical engineering series). Espoo: Finnish Acad. of Technology, 1998, ISBN: 978-952-5148-43-5.

[145] Z. Huang, J. Fang, X. Liu, and B. Han, "Loss Calculation and Thermal Analysis of Rotors supported by Active Magnetic Bearings for High-speed Permanent Magnet Electrical Machines," *IEEE Transactions on Industrial Electronics*, 2015.

[146] ZVEI e.V., Verband der Elektro- und Digitalindustrie, Fachverband Electrical Winding & Insulation Systems, Ed., *Leitfaden Strategien zum Wärmemanagement in der Elektro- und Elektronikindustrie*. 2021.

[147] D. A. Howey, P. R. N. Childs, and A. S. Holmes, "Air-Gap Convection in Rotating Electrical Machines," *IEEE Transactions on Industrial Electronics*, vol. 59, no. 3, 2012.

[148] L. A. Dorfman, *Hydrodynamic resistance and the heat loss of rotating solids / L. A. Dorfman*. 1963.

[149] M. Fénot, Y. Bertin, E. Dorignac, and G. Lalizel, "A Review of Heat Transfer between Concentric Rotating Cylinders with or without Axial Flow," *International Journal of Thermal Sciences*, vol. 50, no. 7, 2011.

[150] K. M. Becker and J. Kaye, "Measurements of Diabatic Flow in an Annulus With an Inner Rotating Cylinder," *Journal of Heat Transfer*, vol. 84, no. 2, 1962.

[151] “Brennstoffzellenstacks | EKPO Fuel Cell Technologies,” Accessed: Nov. 2, 2023. https : / / www . ekpo - fuelcell . com / de / produkte - technologien/brennstoffzellenstacks.

[152] “Fuel-cell stack: mass production starting 2022 - Bosch Global,” Accessed: Nov. 2, 2023. https://www.bosch.com/stories/fuel-cell-stack/.

[153] “zepp.X150: ultra high power density - zepp.solutions,” Accessed: Nov. 2, 2023. https://zepp.solutions/en/x150/.

Datasheets

[D1] *N45UH – Datasheet*, Arnold Magnetic Technologies, Rochester, New York, USA, 2017.

[D2] *Recoma® 35E – Datasheet*, Arnold Magnetic Technologies, Rochester, New York, USA, 2017.

[D3] "Samarium Cobalt Magnets (SmCo)," Accessed: Oct. 2, 2023. https://www.miottisrl.com/de/product/magnesy-samarowo-kobaltowe-smco/.

[D4] "NdFeB - Datasheet," Accessed: Oct. 2, 2023. https://www.miottisrl.com/de/product/magnete-neodym-eisen-bor-ndfeb/.

[D5] "Samarium Cobalt Magnets Demagnetization Curves." English, Accessed: Dec. 4, 2024. https://www.armsmag.com/images/Sm2Co17-Grade32.png.

[D6] *Hi-Lite NO20-1200H Data Sheet*, Tata Steel UK Limited, London, UK, 2019.

[D7] *Super Core – Electrical steel sheets for high-frequency application*, JFE Steel Corporation, Tokyo, Japan, 2023.

[D8] *Maxwell Help, Release 2020 R2*, ANSYS, Inc., Canonsburg, Pennsylvania, USA, 2020.